

PETRO VIETNAM JOURNAL



An Official Publication of the Vietnam National Oil and Gas Group Vol 10 - 2018

ISSN-0866-854X

PETROVIETNAM Vol 10 - 2018





EDITOR-IN-CHIEF

Dr. Nguyen Quoc Thap

DEPUTY EDITOR-IN-CHIEF

Dr. Le Manh Hung

Dr. Phan Ngoc Trung

EDITORIAL BOARD MEMBERS

Dr. Trinh Xuan Cuong

Dr. Nguyen Minh Dao

BSc. Vu Khanh Dong

Dr. Nguyen Anh Duc

MSc. Nguyen Ngoc Hoan

MSc. Le Ngoc Son

Dr. Cao Tung Son

Eng. Le Hong Thai

MSc. Ton Anh Thi

MSc. Nguyen Van Tuan

Dr. Phan Tien Vien

Dr. Tran Quoc Viet

Dr. Nguyen Tien Vinh

SECRETARY

MSc. Le Van Khoa

M.A. Nguyen Thi Viet Ha

DESIGNED BY

Le Hong Van

MANAGEMENT

Vietnam Petroleum Institute

CONTACT ADDRESS

Floor M2, VPI Tower, Trung Kinh street, Yen Hoa ward, Cau Giay district, Ha Noi

*Tel: (+84-24) 37727108 * Fax: (+84-24) 37727107 * Email: tcdk@pvn.vn/pvj@pvn.vn*

Mobile: 0982288671

PETROLEUM EXPLORATION & PRODUCTION

PETROVIETNAM JOURNAL
Volume 10/2018, p. 4 - 11
ISSN: 0866-854X

PETROVIETNAM
JOURNAL

Application of machine learning techniques in estimation of fracture porosity using fuzzy inference system for a FGB reservoir in Cuu Long basin, Vietnam

Phan Huy Gao, Nakaret Kam, Khusan Sandomi, Bul Duc Trung
Khoa Institute of Technology (KIT)
Email: hgao@kit.edu.vn

Summary

Determination of porosity of a fractured granite basement (FGB) reservoir in the Cuu Long basin has always been a challenge for petrophysicists. In this study, an analysis of fracture porosity was successfully conducted, using a machine-learning technique, i.e., fuzzy inference system (FIS), the well log data including gamma ray (GR), deep resistivity (ILD), shallow resistivity (ILS), sonic (DT), bulk density (RHOB), neutron porosity (NPHI), photoelectric factor (PEF) and calcar (CAL) from two wells BR001 and BR002, were used as the input for FIS analyses. Fracture porosity calculated by conventional method was found between 0.01 and 2.24% for BR001 and between 0.15 and 6.63% for BR002, respectively. These values match very well with those predicted by various FIS techniques, i.e. Sugeno, Mamdani and Subtractive FIS models. It is expected that the approach of using FIS in petrophysical analysis as presented in this paper can be further applied for other fractured granite basement reservoirs in the Cuu Long and Nam Con Son basins, offshore southern Vietnam.

Key words: Machine learning, fuzzy inference system (FIS), well log analysis, fracture porosity, Cuu Long basin.

1. Introduction

As shown in Figure 1 the study site is located in the northern Cuu Long basin, which was formed by the fragmentation, rifting, and subsidence of Pale-Tertiary basement and later filled with the end-of-Eocene to Pliocene-Quaternary continental, shallow marine and coastal plain deposits.

Common methods used to estimate primary porosity of a clastic reservoir are not always suitable to estimate the fracture porosity. As a result, petrophysicists keep trying to find new approaches to estimate fracture porosity. In this study, porosity of a fractured granite basement reservoir will be estimated by using a soft computing technique known as fuzzy inference system (FIS), whose results will be compared with those calculated based on a conventional method [1].

Concept of soft computing was first put forward by Zadeh [2], which is known to include the major methods such as fuzzy logic, evolutionary computation, neural computing, and probabilistic reasoning.

Date of receipt: 4/10/2018; Date of review/accepting: 4/1 - 15/5/2018; Date of approval: 4/10/2018.

4 **PETROLEUM JOURNAL** VOL.10/2018



PETROVIETNAM JOURNAL
Volume 10/2018, p. 42 - 48
ISSN: 0866-854X

PETROVIETNAM
JOURNAL

Maximising production in shale reservoirs

Hen Cheng Liu
National University of Singapore
Email: ceoh@nus.edu.sg

Summary

This paper describes the interaction between hydraulic fractures and the multi-porosity system of shale reservoirs. During the process of hydraulic fracturing, a complex fracture network consisting of primary and secondary fractures is created. It is postulated that only shale porositites that are in contact with these hydraulic fractures will contribute to hydrocarbon production. Furthermore, we propose a way to maximise well productivity by injecting micro-sized proppants into the secondary hydraulic fractures and reactivated natural fractures to prevent them from closing during production and thereby extending the fracture network. Both laboratory experiments and field tests have shown encouraging results of using micro-sized proppants to enhance the productivity of Barnett shale. More research is warranted to study the applicability and optimisation of micro-sized proppants in production enhancement in other shale formations.

Key words: Shale reservoir, micro-sized proppant, maximizing production, natural fracture, hydraulic fracture.

1. Introduction

The shale revolution in North America in the last decade has captured the attention of both researchers and practitioners in the oil and gas industry. The current research & development effort focuses on the optimisation of multi-stage hydraulic fracturing in long horizontal wells in shale reservoirs. However, a fundamental understanding of the interaction between hydraulic fractures, natural fractures and the pore system of the shale reservoir is lacking. The objective of this paper is to fill this knowledge gap. Based on this understanding, we propose a way to maximise productivity of shale reservoirs by increasing the connectivity between the hydraulic fractures and the pore system of the reservoir.

2. Pore system in shale reservoirs

The pore structure of a shale reservoir is more complicated than that of a conventional reservoir because shale contains both organic matter and inorganic matter. The former consists of kerogen and the latter carbonate, quartz, feldspar and clays. The various types of natural porositites of shale formation can be classified as Figure 1.

- Organic pores
- Inorganic pores
- Pore channel
- Natural fracture

Organic matter such as kerogen tends to develop intraparticle pores during the evolution and expulsion of hydrocarbons from the kerogen [1]. These intraparticle pores have been observed in all mudstones, and believed to contribute dominantly to the total porosity. Their shapes can be spheroidal, bubble-like, or pendular. Organic porosity can also be enhanced by cracks or fractures within the organic matter.

Inorganic pores

Inorganic pores are those that exist in inorganic minerals such as clays, quartz and feldspar. Microscopic observations show that they exist as partially open floccules, triangular pores at clay platelet junctions or lenticular, slit-like pores between clay flakes. These inorganic pores may reduce in size during hydrocarbon production due to compression of the slit-like pore structures because of the increase in effective vertical stress [1].

Artificial porosity

- Organic pores
- Primary hydraulic fracture
- Secondary hydraulic fracture

Date of receipt: 10/10/2018; Date of review/accepting: 10/11 - 15/12/2018; Date of approval: 4/10/2018.

4 **PETROLEUM JOURNAL** VOL.10/2018

SCIENTIFIC RESEARCH



PETROLEUM EXPLORATION & PRODUCTION

- 4.** Application of machine learning techniques in estimation of fracture porosity using fuzzy inference system for a FGB reservoir in Cuu Long basin, Vietnam
- 12.** Application of seismic attribute analysis to study fractured basement
- 23.** Predicting hydrocarbon migration and accumulation in Block 09-3/12, Cuu Long basin by 3D petroleum system modelling

- 34.** Sources, mechanism and prediction method of scale formation in oil production in Vietnam
- 43.** Maximising production in shale reservoirs
- 49.** Combining low frequency spectral decomposition and post stack seismic inversion to identify Middle Miocene gas bearing sands at Hai Thach field



PETROLEUM PROCESSING

- 57.** KRES-ES™ revamp produces more ammonia from less natural gas by energy substitution
- 63.** Approaches to enhance the value of Ca Voi Xanh gas via its transformation into nanocarbon materials

PETROVIETNAM JOURNAL
 Volume 10(2018), p. 57- 62
 ISSN-0866-854X



KRES-ES™ revamp produces more ammonia from less natural gas by energy substitution

Vikram Singh, Shashi Singh
 KBR
 Email: vikram.singh@kbr.com

Summary

The 5th KRES™ technology based Ammonia Plant is now in operation in a grass-root project at PT. Panca Amara Utama (PAU), Indonesia. This follows earlier successful operations in revamp projects - one since 2009 and another since 2015. KBR has therefore studied various schemes in which KRES technology could benefit ammonia plant operators. As a result, KBR is now offering low cost KRES-ES™ technology (patent pending) for revamping ammonia plants by energy substitution.

Ammonia plants having either expensive or curtailed/uncertain supply of natural gas may find this technology a solution to their problem if an alternative source of energy, e.g. coal, is available. It offers an ideal solution for locations facing natural gas shortage or where natural gas is likely to become too expensive to allow viable operations, after building the plant. This enjoys reliability of reforming process (over coal gasification). It also allows the plant to switch totally to natural gas in the future if natural gas becomes available. The revamped ammonia plant requires oxygen and steam imports. Steam import can be met by either using existing capacity or an alternative source of energy. Alternative source of energy may be fossil fuel like coal or other sources. Total natural gas consumption is reduced to less than 6.55 Gcal/MT of ammonia by adding a new reforming exchanger to the existing primary and secondary reformers.

Three examples of KRES-ES based revamps are presented including technical and economic analysis to illustrate the application of this technology.

Key words: KRES™ - KBR reforming exchanger system, ammonia plant, coal, natural gas, ammonia, energy saving.

1. Introduction

Vietnam has a large range of domestic primary energy sources. These resources however are fast depleting. The power sector has grown in Vietnam as also the consumption of natural gas in the generation of power, thus leading to a competing use of natural gas for power generation versus downstream industry. This, along with the government's continued thrust on implementation of energy efficiency measures in operating plants, gives an opportunity to the ammonia industry to consider technology options to address both these needs (a) use of alternate source of energy for ammonia production, e.g. coal and (b) implementing energy reduction measures in their plants.

KRES™ - KBR reforming exchanger system that replaces conventional primary and secondary reformers in an ammonia plant has been in successful commercial

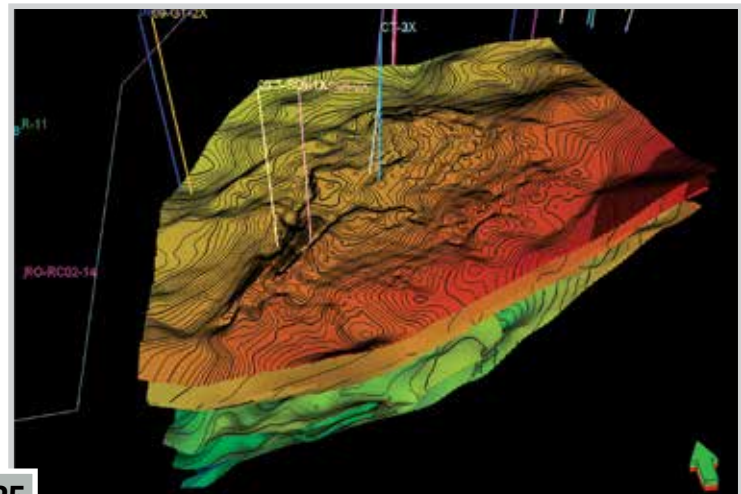
operation [1, 2] in the ammonia plants in Methanex, Canada, since 1994 and in Luohu, China, since 2003. A reforming exchanger is the heart of the KRES technology. It uses high temperature process heat exiting the secondary reformer (or exiting an auto-thermal reformer) to produce syngas by reforming an additional flow of natural gas and steam. As described in a previous paper [3], KRES has been offered as two process schemes. One of these two schemes is used at Methanex and Luohu. The other scheme is used in the third KRES unit in the Chambal Fertilizers & Chemicals Ltd Plant, Chambal Fertilizers & Chemicals Ltd. (CFCL) in India commissioned their KRES based revamp project in their ammonia plant-1 that is in successful operation since April 2009. Since then, two more plants have implemented KRES, one in PCS Lima Plant in Ohio (US) in 2015 (Foster Wheeler Technology) and another in the 1,900 million ton per day grassroot KBR technology ammonia plant in PT. Panca Amara Utama (PAU), Banggai, Indonesia in 2018.

KBR is now offering KRES-Energy Substitution (KRES-ES™) technology (patent pending) as another application

PETROVIETNAM JOURNAL, VOL. 10(2)2018 57



17



25



PETROLEUM TECHNOLOGIES & STRUCTURES

69. Stray current interference and mitigation for underground pipeline

57

Application of machine learning techniques in estimation of fracture porosity using fuzzy inference system for a FGB reservoir in Cuu Long basin, Vietnam

Pham Huy Giao, Nakaret Kano, Kushan Sandunil, Bui Duc Trung

Asian Institute of Technology (AIT)

Email: hgiao@ait.asia

Summary

Determination of porosity of a fractured granite basement (FGB) reservoir in the Cuu Long basin has always been a challenge for petrophysicists. In this study, an analysis of fracture porosity was successfully conducted, using a machine-learning technique, i.e., fuzzy inference system (FIS), the well log data including gamma ray (GR), deep resistivity (LLD), shallow resistivity (LLS), sonic (DT), bulk density (RHOB), neutron porosity (NPHI), photoelectric factor (PEF) and caliper (CAL) from two wells BHX01 and BHX02, were used as the input for FIS analyses. Fracture porosity calculated by conventional method was found between 0.01 and 2.24% for BHX01 and between 0.15 and 6.63% for BHX02, respectively. These values match very well with those predicted by various FIS techniques, i.e. Sugeno, Mamdani and Subtractive FIS models. It is expected that the approach of using FIS in petrophysical analysis as presented in this paper can be further applied for other fractured granite basement reservoirs in the Cuu Long and Nam Con Son basins, offshore southern Vietnam.

Key words: Machine learning, fuzzy interference system (FIS), well log analysis, fracture porosity, Cuu long basin.

1. Introduction

As shown in Figure 1 the study site is located in the northern Cuu Long basin, which was formed by the fragmentation, rifting, and subsidence of Pre-Tertiary basement and later filled with the end-of-Eocene to Pliocene-Quaternary continental, shallow marine and coastal plain deposits.

Common methods used to estimate primary porosity of a clastic reservoir are not always suitable to estimate the fracture porosity. As a result, petrophysicists keep trying to find new approaches to estimate fracture porosity. In this study, porosity of a fractured granite basement reservoir will be estimated by using a soft computing technique known as fuzzy inference system (FIS), whose results will be compared with those calculated based on a conventional method [1].

Concept of soft computing was first put forward by Zadeh [2], which is known to include the major methods such as fuzzy logic, evolutionary computation, neural computing, and probabilistic reasoning.

Fuzzy inference systems (FIS) are designed using fuzzy set, which is a kind of mathematical set, where each element of the set has a degree of membership. A fuzzy set does not require a crisp and a clearly defined boundary. It can contain elements with a partial degree of membership. A crisp set of reservoir porosity may include {fair, very good} where the degree of membership of an element (denoted as μ) is either 0 or 1; thus, there can only be one kind of reservoir porosity. For example, in Figure 2a, if porosity (ϕ_p) is greater than 0.5, reservoir porosity is very good ($\mu = 1.0$), but if porosity is lower than 0.5, it is poor ($\mu = 0$). A Fuzzy set, on the other hand, allows each

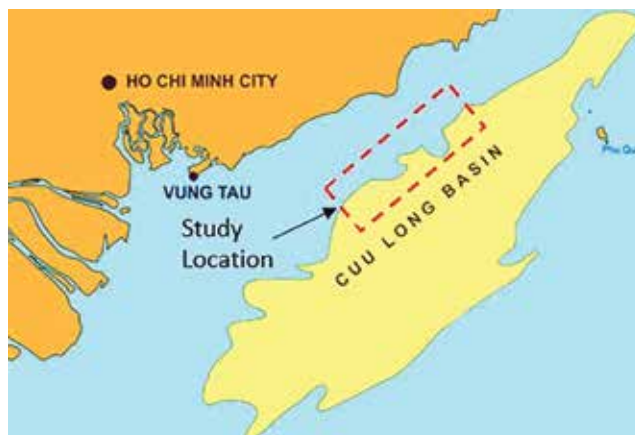


Figure 1. Study location.

Date of receipt: 4/4/2018. Date of review and editing: 4/4 - 11/5/2018.

Date of approval: 4/10/2018.

element to have partial membership; thus, one can write a fuzzy set as {poor, fair, good, very good}. As an example, in Figure 2b, if porosity is 0.4, it is classified as fair.

Fuzzy inference (reasoning) is the actual process of mapping from a given input to an output using fuzzy logic. Figure 3 shows the architecture of a fuzzy inference system.

As seen in Figure 3 the fuzzifier converts the raw input data into a linguistic variable using the membership function stored in the fuzzy knowledge base. The inference engine further converts the fuzzy input to the fuzzy output using if-then type fuzzy rules. The defuzzifier converts the fuzzy output of the inference engine to crisp using membership functions analogous to the ones used by the fuzzifier.

There are two main types of fuzzy interference methods based on clustering of numerical data, i.e. C-means and Subtractive. The former is a supervised algorithm that can only be used when there is a set of inputs and corresponding outputs to those inputs (training set). The final output of fuzzy C-means is not a FIS but rather a list of cluster centres and several membership grades for each data point. One can use the information returned by the fuzzy C-means routine to build a FIS. Two types of FIS can be modelled using C-means clustering,

i.e. Mamdani and Sugeno that are similar in many aspects, and namely, the first two parts of the fuzzy inference process, fuzzifying the inputs and applying the fuzzy operator in the inference engine (Figure 3) are exactly the same. The most fundamental difference between Mamdani type FIS and Sugeno type FIS is the way the crisp output is generated from the fuzzy inputs. While Mamdani FIS uses the technique of defuzzification of a fuzzy output, Sugeno FIS uses weighted average to compute the crisp [3]. So basically, Sugeno model bi-passes the defuzzification. As a result, in Mamdani model there is an output membership function whereas in Sugeno model there is no output membership function. Subtractive is an unsupervised algorithm. It can be utilised when there are no corresponding outputs for a set of input data. This method is focusing on finding regions in the feature space with high densities of data points. The data points within a prespecified, fuzzy radius are then subtracted (removed), and the algorithm proceeds its search for a new point with the highest number of neighbours. The iteration continues until all points have been tested. The quality of the solution depends strongly on the choice of initial values [4].

Application of fuzzy interference systems in petrophysics has been used over the past two decades. Fang and Chen [5] predicted porosity and permeability from the compositional and textural characteristics of sandstones, using fuzzy modelling which is not only assumption-free but also tolerant of outliers. Fuzzy modelling is capable of making both linguistic and numeric predictions based on qualitative knowledge and/or quantitative data. Martinez et al. [6] presented a technique for the identification and characterisation of naturally fractured reservoirs. A fuzzy inference system was implemented in their study to obtain a fracture index using only data from conventional well logs. Additionally, model from O'Connell and Budiansky [7] for the prediction of elastic properties of fractured porous rocks is inverted using genetic algorithms to obtain crack density and crack aspect ratio. The results obtained are compared with core information available. Hambalek and Gonzalez [8] applied fuzzy logic theory in order to establish a narrow relation between well logs and the seven rock types (lithofacies) of the sedimentological model that describes a very complex reservoir in eastern Venezuela. Core analysis of five wells and the established fuzzy relations are used to get the lithofacies description and possible values of permeability in eighteen wells of the same area having only electrical logs. The efficiency

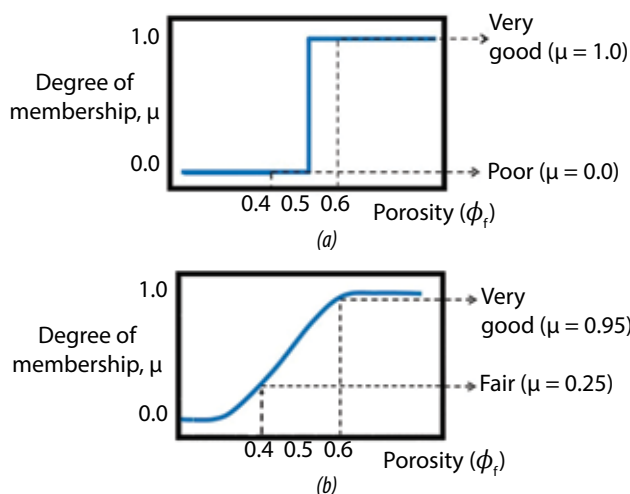


Figure 2. Membership function: (a) crisp set; (b) fuzzy set.

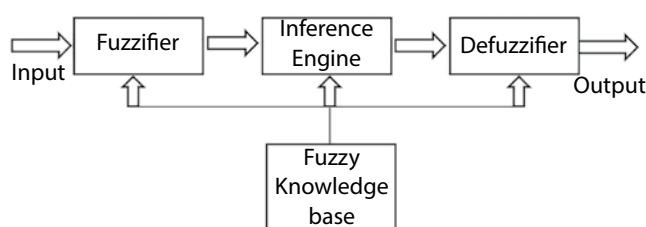


Figure 3. Architecture of a fuzzy inference system.

of the algorithm developed was verified against a control well with both log and core data. The results are very satisfactory and open the possibilities for future research and application. Abdulraheem [9] presented the use of fuzzy logic modelling to estimate permeability from wireline logs data for a carbonate reservoir in the Middle East. In this study, correlation coefficients are used as criteria for checking whether a given wireline log is suitable as an input for fuzzy modelling.

2. Methodology

Well log data gamma ray (GR), deep resistivity (LLD), shallow resistivity (LLS), sonic (DT), bulk density (RHOB), neutron porosity (NPHI), photoelectric factor (PEF), and caliper (CAL) were collected from 2 wells BHX01 and BHX02 at a study site in Cuu Long basin, Vietnam.

In this research, the depth interval from 2,515m to 3,015m of well BHX01 and that from 3,050m to 3,870m of well BHX02 were selected. Four reservoir zones of well BHX01 and five reservoir zones of well BHX02 [10] were used in the analyses as shown in Table 1.

The flowchart of the study is shown in Figure 4. First of all, fracture porosities were calculated using a conventional

method suggested by Elkewidy & Tiab [1] that is also described in detail in Giao and Sandunil [11] by Equations 1 - 3. Matrix density will be assumed to be 2.71g/cc, which is for limestone, and fluid density is 1.00g/cc, which is for water. This is because parameters of wireline logging tools used to acquire formation density and neutron porosity of formation are calibra

$$\phi_D = \frac{\rho_{ma} - \rho_b}{\rho_{ma} - \rho_f} \tag{1}$$

$$\phi_t = \frac{\phi_D + \phi_N}{2} \tag{2}$$

$$\phi_f = \frac{\phi_t^{m+1} - \phi_t^m}{\phi_t^m - 1} \tag{3}$$

Where:

- ϕ_t : Total porosity, fraction;
- ϕ_D : Porosity calculated from bulk density, fraction;
- ϕ_N : Neutron porosity, fraction;
- ϕ_f : Fracture porosity, fraction;
- ρ_b : Bulk density, g/cc;
- ρ_{ma} : Matrix density, g/cc;
- ρ_f : Fluid density, g/cc;
- m: Cementation factor, dimensionless.

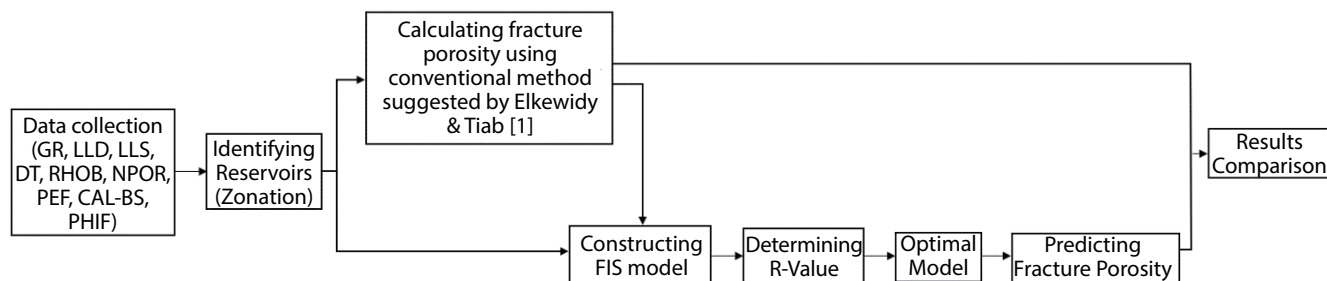


Figure 4. Flow chart of the methodology.

Table 1. Measured depth and true vertical depth of the analysed reservoir zones

Zone	BHX01		BHX02	
	MD (m)	TVD (m)	MD (m)	TVD (m)
Zone 1	2,515 - 2,540	2,514 - 2,540	3,050 - 3,190	2,655 - 2,790
Zone 2	2,540 - 2,655	2,540 - 2,655	3,190 - 3,415	2,790 - 3,015
Zone 3	2,655 - 2,790	2,655 - 2,790	3,415 - 3,525	3,015 - 3,114
Zone 4	2,790 - 3,015	2,790 - 3,015	3,525 - 3,700	3,114 - 3,314
Zone 5	N/A	N/A	3,700 - 3,868	3,314 - 3,466

Table 2. Fracture porosity calculated by conventional approach [1]

BHX01					BHX02				
Zone	MD (m)	TVD (m)	Average ϕ_f (%)	m	Zone	MD (m)	TVD (m)	Average ϕ_f (%)	m
1	2,515 - 2,540	2,514 - 2,540	2.24	1.75	1	3,050 - 3,190	2,655 - 2,790	0.69	2.38
2	2,540 - 2,655	2,540 - 2,655	0.13	2.32	2	3,190 - 3,415	2,790 - 3,015	0.18	2.38
3	2,655 - 2,790	2,655 - 2,790	0.03	2.60	3	3,415 - 3,525	3,015 - 3,114	2.25	1.52
4	2,790 - 3,015	2,790 - 3,015	0.14	2.60	4	3,525 - 3,700	3,114 - 3,314	5.43	1.21
					5	3,700 - 3,868	3,314 - 3,466	3.59	1.28

In the next step, two analyses were conducted to predict porosity using three different FIS models, i.e., Sugeno, Mamdani and Subtractive. In the first analysis

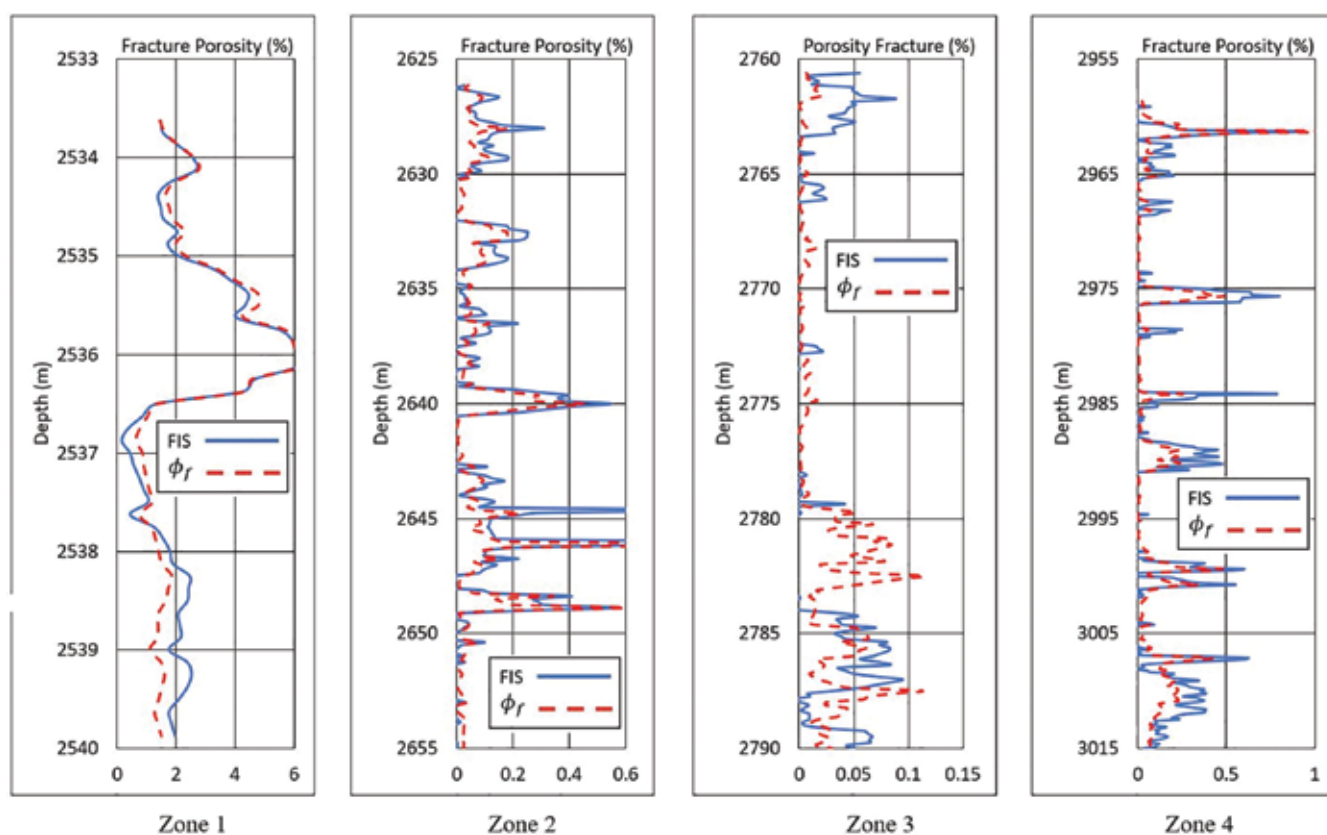
(Analysis I), FIS-based prediction was done for every reservoir zone of wells BHX01 and BHX02, separately, i.e., for each zone 75% of well log data are used for training

Table 3. Results of fracture porosity predicted by FIS in Analyses I and II

Analysis I										Analysis II (data from zones 3 & 4 of BHX01 were trained to predict porosity of zones 1 & 2 of BHX02)						
BHX01					BHX02					Zone	Conventional	FIS Model				
Zone	Conventional	C-mean		Subtractive	Zone	Conventional	C-mean		Subtractive			Zone	Conventional	C-mean		Subtractive
		Sugeno	Mamdani				Sugeno	Mamdani						Sugeno	Mamdani	
1	2.24	2.31	3.02	2.27	1	0.47	0.51	0.63	0.44	1	0.69	0.33	0.26	0.39		
2	0.06	0.06	0.09	0.06	2	0.15	0.10	0.18	0.16	2	0.17	0.24	0.21	0.15		
3	0.01	0.00	0.02	0.01	3	1.37	1.21	1.70	1.34	3	N/A	N/A	N/A	N/A		
4	0.07	0.03	0.08	0.07	4	6.63	6.52	5.92	6.58	4	N/A	N/A	N/A	N/A		
N/A	N/A	N/A	N/A	N/A	5	3.03	3.02	3.41	3.02	5	N/A	N/A	N/A	N/A		

Table 4. Correlation coefficients in two Analyses I & II, using Sugeno, Mamdani and Subtractive models

Analysis I								Analysis II (data from zones 3 & 4 of BHX01 were trained to predict porosity of zones 1 & 2 of BHX02)				
BHX01				BHX02				Zone	C-mean		Subtractive	
Zone	C-mean		Subtractive	Zone	C-mean		Subtractive		Zone	C-mean		Subtractive
	Sugeno	Mamdani			Sugeno	Mamdani						
1	0.962	0.802	1.000	1	0.952	0.838	0.994	1	0.954	0.374	0.591	
2	0.809	0.720	0.834	2	0.910	0.848	0.977	2	0.833	0.630	0.901	
3	0.924	0.905	0.985	3	0.992	0.552	0.993	3	N/A	N/A	N/A	
4	0.831	0.820	0.954	4	0.999	0.804	1.000	4	N/A	N/A	N/A	
N/A	N/A	N/A	N/A	5	0.997	0.882	1.000	5	N/A	N/A	N/A	



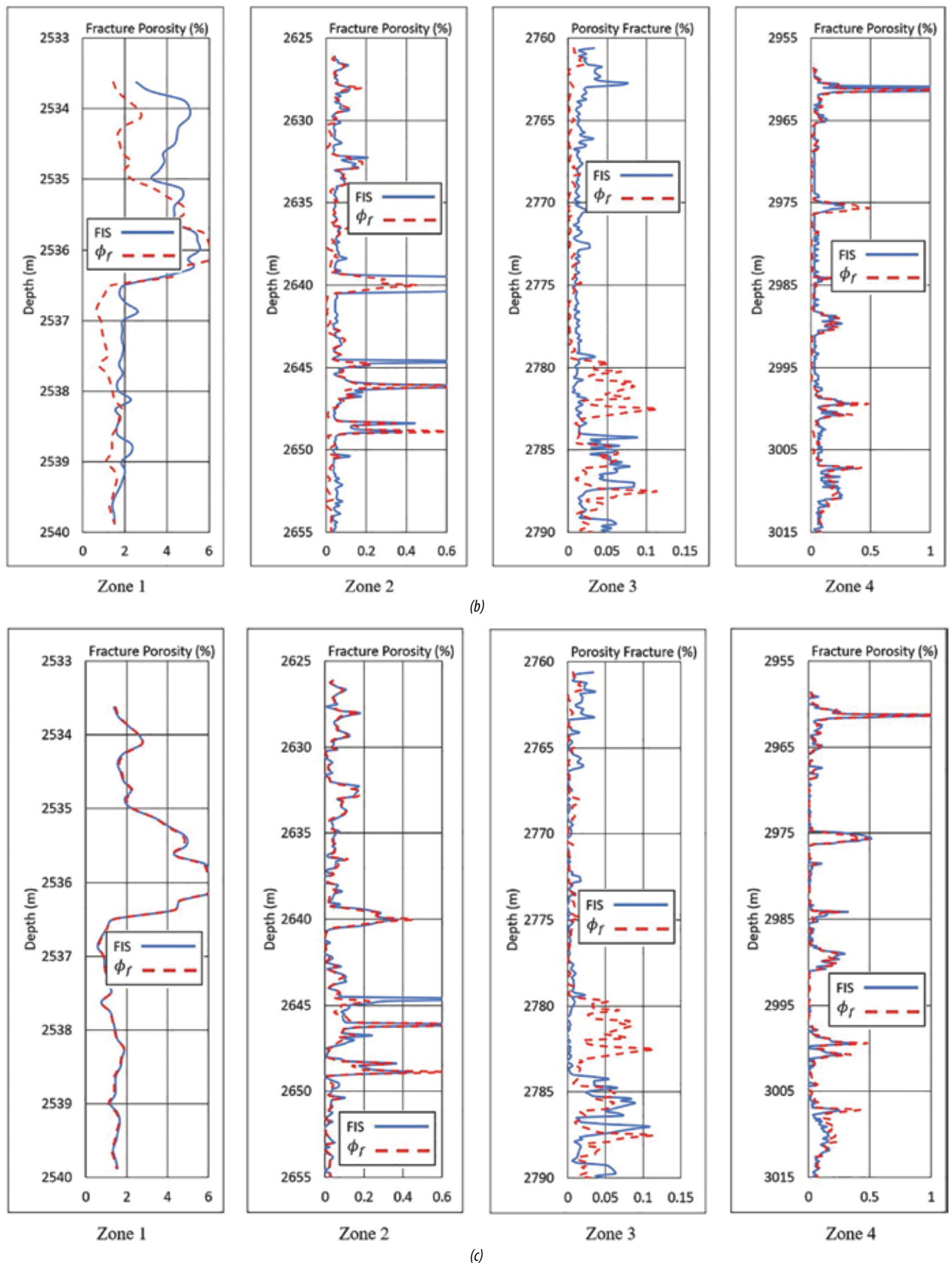
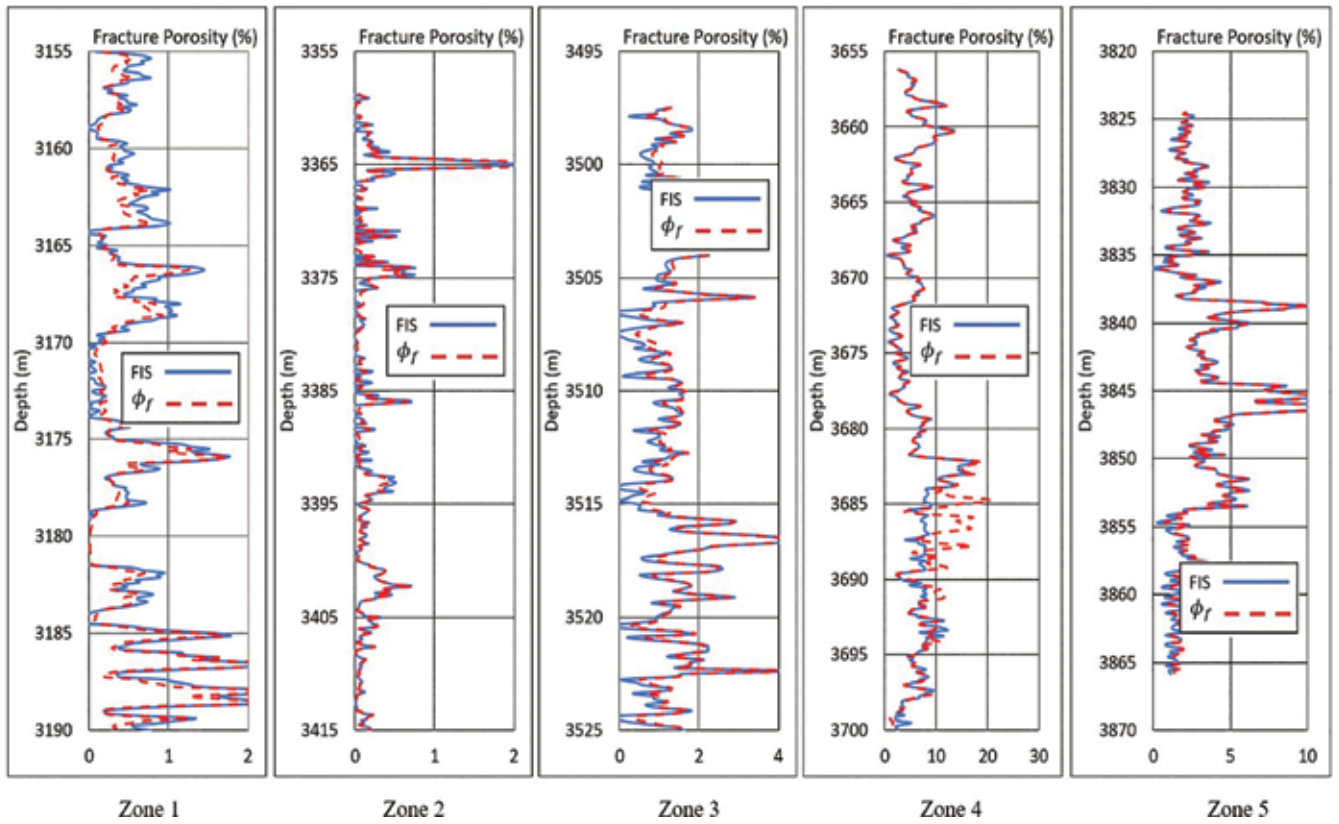
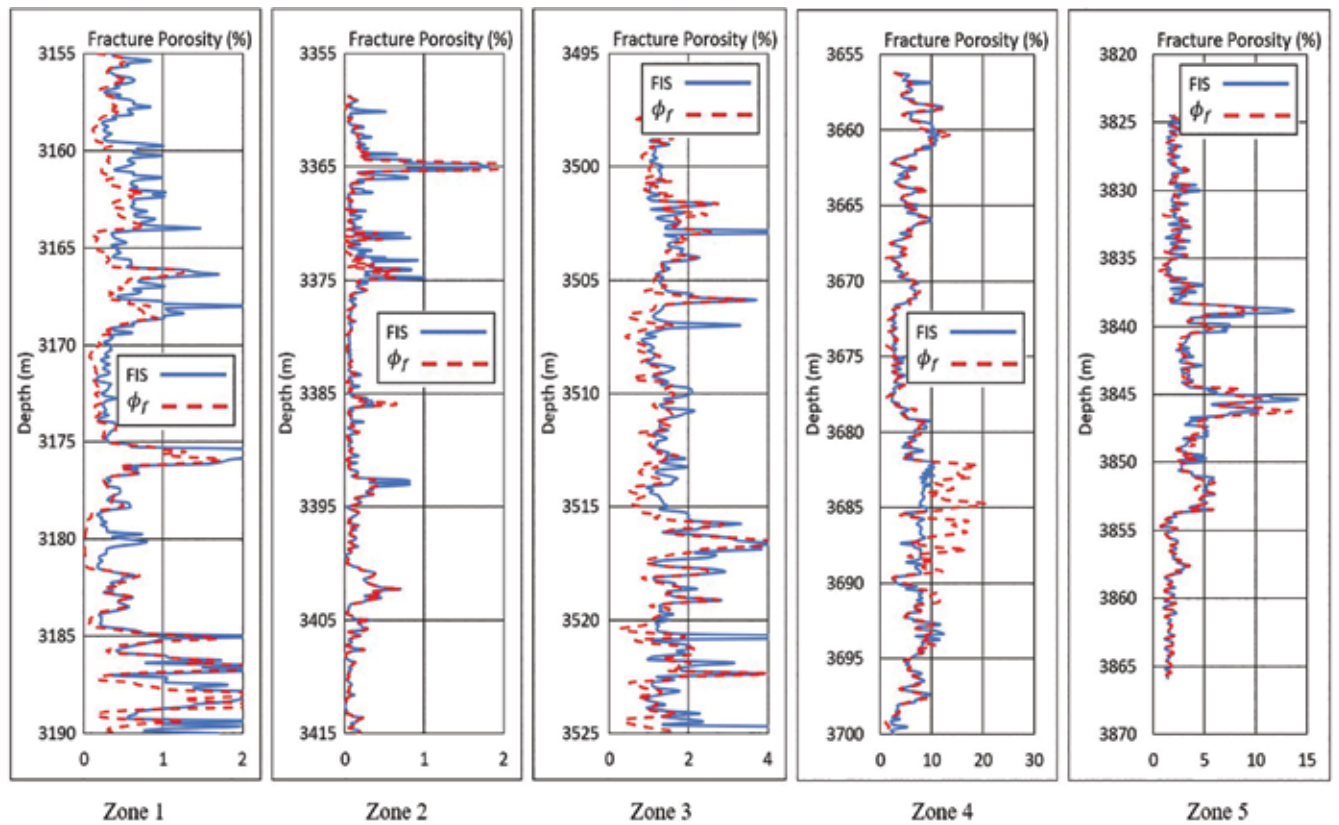


Figure 5. Fracture porosity calculated for zones 1 - 4, well BHX01, Analysis I by (a) Sugeno model, (b) Mamdani model, (c) Subtractive model.



(a)



(b)

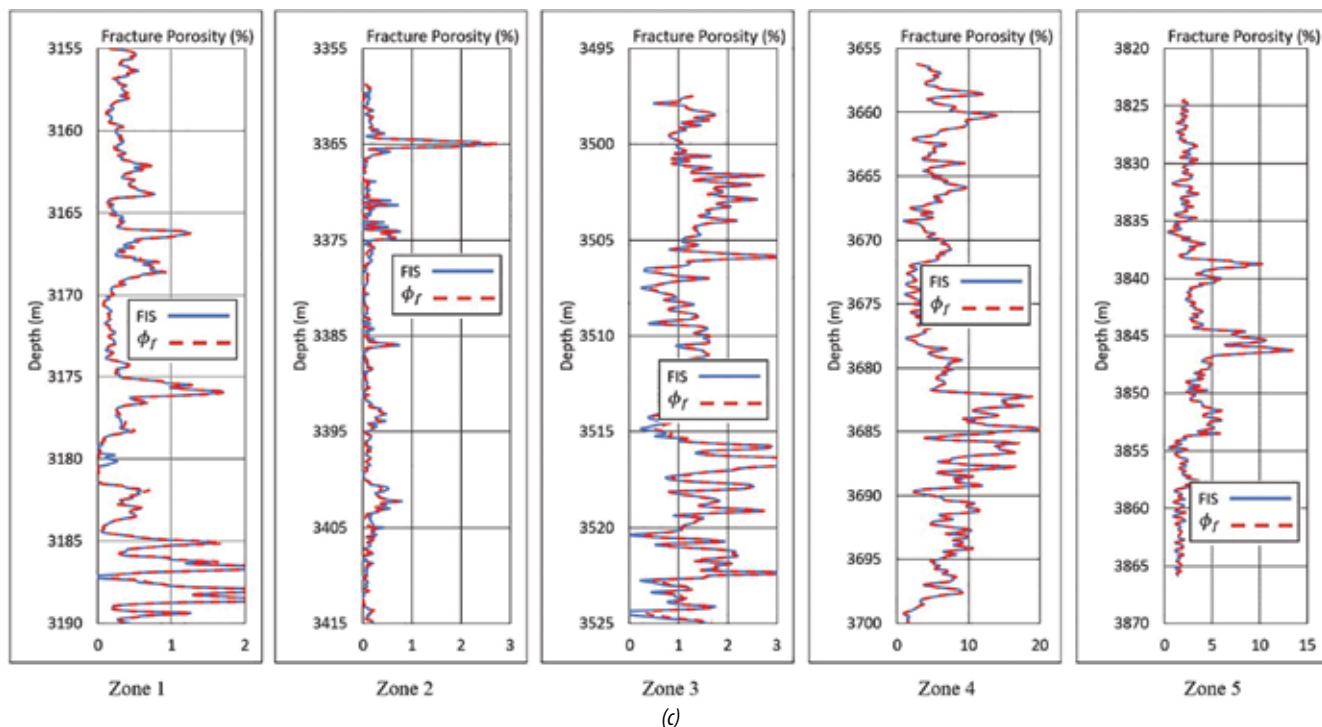


Figure 6. Fracture porosity calculated for zones 1 - 5, well BHX02, Analysis I by (a) Sugeno model, (b) Mamdani model, (c) Subtractive model.

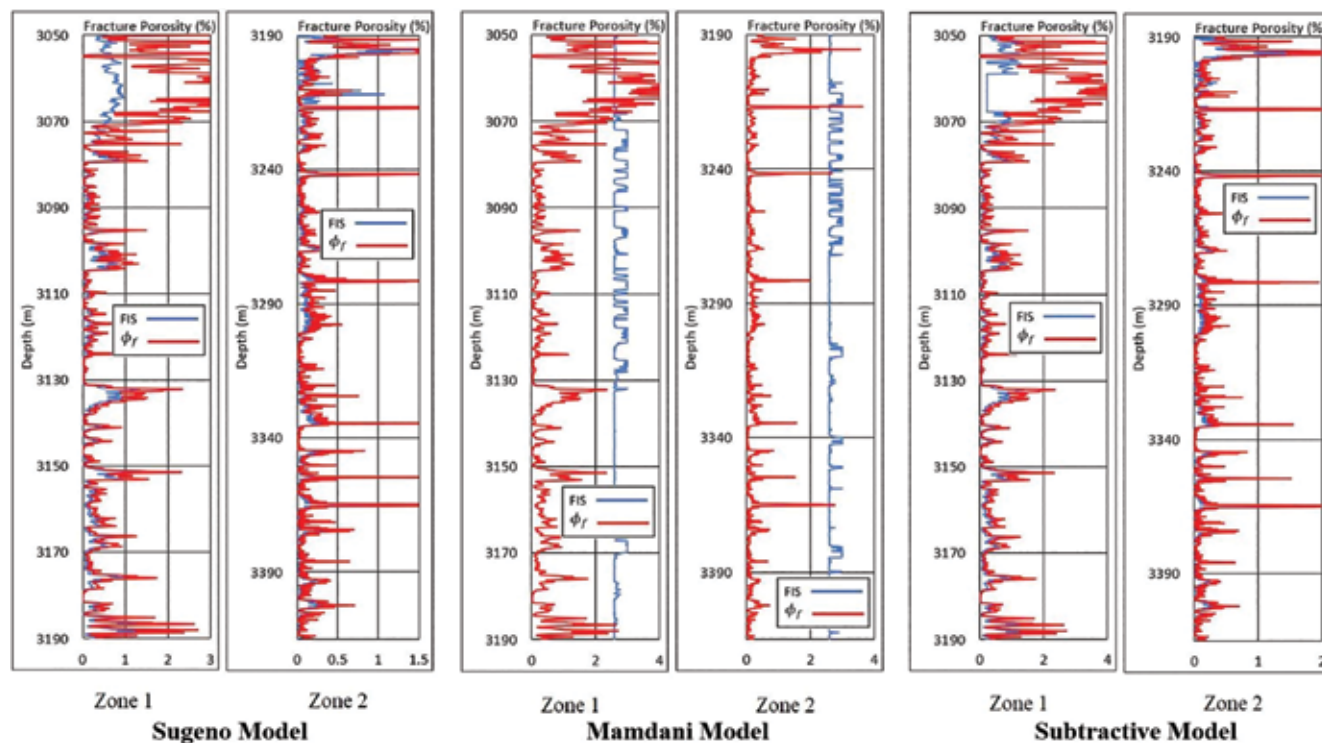


Figure 7. Fracture porosity calculated by Sugeno, Mamdani and Subtractive models for zones 1 and 2, well BHX02, Analysis II.

and the remaining 25% of the well log data are used for prediction. In the second analysis (Analysis II), the well log data of zones 3 and 4 of BHX01 were used to train the FIS models to predict the fracture porosity of zones 1 and 2 of BHX02 as indicated in Table 1.

3. Results and discussion

The average fracture porosities for each reservoir zone as calculated using Elkewidy & Tiab's method [1] shown in Table 2 are found to be between 0.03 and 2.24 for BHX01, and 0.18 and 5.43 for BHX02, respectively. These

conventionally-calculated values were further used to train the FIS models. Table 3 shows the results of Analysis I, indicating the average fracture porosities predicted by Sugeno, Mamdani and Subtractive in comparison with those calculated by the conventional method.

The results of fracture porosity predicted by FIS models are plotted in Figure 5 and Figure 6 as well as shown in Table 3, which are quite close to those calculated by the conventional method shown in Table 2. Among three FIS models, the values predicted by two models of Sugeno and Subtractive are better than those obtained by Mamdani model. This remark is further supported by the calculated correlation coefficient of each FIS analysis as shown in Table 4, which are lower in case of Mamdani model. Out of the three models, Subtractive model gave the best results.

As seen in Figures 5 - 7, the fracture porosity curves predicted by Sugeno and Subtractive models follow well the shape of the conventionally-calculated curve of ϕ_r .

4. Conclusions

The FIS Sugeno and Subtractive models proved to be good methods to predict fracture porosity, which is between 0.00 - 2.31 and 0.01 - 2.27 for well BHX01, 0.10 - 6.52 and 0.16 - 6.58 for well BHX02, respectively.

Fracture porosity predicted by FIS Mamdani are more deviated from the values calculated by Elkewidy & Tiab's method [1] comparing to those predicted by Sugeno and Subtractive models, the fact which is additionally supported by lower values of correlation coefficient.

Out of the three models employed, FIS Subtractive was the best to predict fracture porosity with the highest correlation coefficients.

Although Analysis I that used the well log data in one well to predict fracture porosity prediction for the same well gave better results than Analysis II that used the well data from one well to predict fracture porosity in another well, the results obtained by the latter are also very satisfactory and encouraging for a wider application in practice to predict the porosity of a fractured granite basement reservoirs in the Cuu Long and Nam Con Son basins.

References

1. Tarek Ibrahim Elkewidy, Djebbar Tiab. *An application of conventional well logs to characterize*

naturally fractured reservoirs with their hydraulic (flow) units; A novel approach. SPE 40038. SPE Gas Technology Symposium, Calgary, Canada. 15 - 18 March, 1998.

2. Lotfi A. Zadeh. *Fuzzy logic, neural network and soft computing.* Communication of the ACM. 1994; 37(3): p. 77 - 84.

3. Abdelwahab Hamam, Nicolas D.Georganas. *A comparison of Mamdani and Sugeno fuzzy inference systems for evaluating the quality of experience of Hapto-Audio-Visual applications.* 2008 IEEE International Workshop on Haptic Audio Visual Environments and Games. 18 - 19 October, 2008: p. 87 - 92.

4. Muriel Bowie. *Fuzzy clustering, feature selection, and membership function optimization.* Seminar Paper, Department of Informatics, University of Fribourg, Switzerland. 2004.

5. J.H.Fang, H.C.Chen. *Fuzzy modeling and the prediction of porosity and permeability from the compositional and textural attributes of sandstone.* Journal of Petroleum Geology. 1997; 20(2): p. 185 - 204.

6. L.P.Martinez, R.G.Hughes, M.L.Wiggins. *Identification and characterization of naturally fractured reservoir using conventional well logs.* University of Oklahoma. 2002.

7. Richard J.O'Connell, Bernard Budiansky. *Seismic velocities in dry and saturated cracked solids.* Journal of Geophysical Research. 1974; 79(35): p. 5412 - 5426.

8. Nancy Hambalek, Reinaldo Gonzalez. *Fuzzy logic applied to lithofacies and permeability forecasting.* SPE 81078. SPE Latin America and Caribbean Petroleum Conference, Trinidad. 27 - 30 April, 2003.

9. Abdulazeez Abdulraheem, Emad Sabakhy, Mujahed Ahmed, Aurifullah Vantala, Putu D. Raharja, Gabor Korvin. *Estimation of permeability from wireline logs in a Middle East carbonate reservoir using fuzzy logic.* SPE 105350. SPE Middle East Oil and Gas Show and Conference, Manama, Bahrain. 11 - 14 March, 2007.

10. Bui Duc Trung. *Petrophysical analysis of a fractured granite reservoir, offshore southern Vietnam.* Master Thesis, GE-10-12. Asian Institute of Technology (AIT). 2011.

11. Pham Huy Giao, Kushan Sandunil. *Application of deep learning in predicting fracture porosity.* Petrovietnam Journal. 2017; 10: p. 14 - 22.

Application of seismic attribute analysis to study fractured basement

Nguyen Thanh Tung¹, Pham Dinh Tan¹, Phan Thien Huong²

¹Vietnam Petroleum Institute, ²Hanoi University of Mining and Geology

Email: tungnt@vpi.pvn.vn

Summary

Seismic attribute analysis is supposed to have a great potential to reveal latent geological features and has been implemented extensively in Cuu Long basin to predict the fractured reservoirs of the basement, however, the results so far have not been up to expectations. In this paper, previous seismic attribute studies are reviewed to show that the low signal to noise ratio (SNR) and the presence of artefacts are the main causes of inaccuracies or even misleading interpretations. To improve the effectiveness of seismic attributes in prediction of fractured reservoirs, three approaches to reduce the influence of noise and artefacts are proposed. The simplest way is to focus on the top basement surface instead of the section below it. A selective combination of independent attributes is used to delineate fault traces and anomalous zones related to rough boundaries on the top basement. To utilise the information inside the basement, principal component analysis (PCA) can be employed to separate noise and artefacts from the useful data. Ultimately, it is possible to increase the SNR in the processing stage with diffraction imaging technique. The processed data then can be analysed by seismic attributes or overlaid on conventional data to aid the interpretation of subtle faults and fractures..

Key words: Seismic attributes, principle component analysis, diffraction imaging, fractured basement, Cuu Long basin.

1. Introduction

Fractured basement is the most important reservoir rock type in Cuu Long basin, offshore Vietnam with over 200 million tons of crude oil produced to date from this target alone. Nevertheless, after over 30 years of production, the prediction of fracture systems in the basement remains a great challenge for exploration and production activities. Since there are no clear reflection signals inside the basement, seismic attribute analysis is often applied to aid interpretation with an attempt to extract useful information for fault and fracture characterisation. In the last two decades many seismic attribute techniques have been implemented for basement targets in the basin, however after drilling results it often turned out that many of the predictions by seismic attributes have been inaccurate or even incorrect [1 - 3]. In this paper the applications of seismic attributes for basement reservoir characterisation in Cuu Long basin are reviewed by collecting information from major oil fields including Bach Ho, Rong, Ca Ngu Vang, Ruby, Diamond, Topaz, Hai Su Den, Su Tu Den, and Su Tu Vang. With lessons learned from the review, suitable approaches of seismic attribute

analysis are proposed to target outstanding issues, thus making seismic attributes more effective for prediction of faults and fractures.

2. Review of previous results

In the early time of seismic attribute applications for basement reservoirs of Cuu Long basin, many "successful cases" have been demonstrated and published. The most well-known example of those probably is the case of Su Tu Den field in Block 15-1, where ant-tracking seismic attributes [4, 5] were used in combination with control beam migration (CBM) processed data [6, 7] to predict faults and fractures inside the basement. Figure 1 shows how ant-tracking attribute was applied to delineate lineaments on a time slice cut through the basement. On cross sections, these distinctive lineaments are steep-dip events that were enhanced by CBM technique and clearly delineated by ant-tracking attribute (Figure 2). With these "successful cases", CBM and seismic attributes such as ant-tracking, coherence, curvature [8 - 10] quickly became popular tools for predicting faults and fractures inside the basement and have been widely applied in all blocks with basement targets such as 09/1, 01-02, 15-1/05, 16/1, etc. The applications of CBM and

Date of receipt: 9/7/2018. Date of review and editing: 9/7 - 8/8/2018.

Date of approval: 4/10/2018.

seismic attributes were extensively implemented in the basement of Hai Su Den field of Block 16-1/05 where faults, domains, fracture zones and well designs were all defined with the help of CBM processed data and their seismic attributes [1]. Figure 3 demonstrates that with CBM technique, faults and fracture zones can be straightforwardly delineated on AI time slices and anomalies of variance attribute at 550ms below the top basement.

In other blocks, seismic attributes were also employed as a handy tool for basement assessment, and the most common attributes were RMS amplitude, AI, coherence, variance and ant-tracking. For example, in Block 01-02 [3], various seismic attributes were used to predict the fractured zones as demonstrated in Figure 4 where coherence and AI horizon slices at 400ms below the top basement indicating anomalous areas interpreted as faults and high fractured zones.

Apparently, the fault and fracture predictions shown above seem convincing, however, it was gradually realised by drilling results that the attribute anomalies inside the basement are not always coincident with faults or fractures. The more well information we have the more difficult it is to match attribute anomalies with fracture zones. A good example is the case of well-known Bach Ho and Rong fields of Block 09-1 [12, 13] which are by far the biggest fracture basement reservoirs in Cuu Long basin. The basement in these fields has been penetrated by hundreds of wells and it shows that many areas with attribute anomalies appear to have no fractures and vice versa. The ant-tracking cross section in Figure 5 across Rong field shows

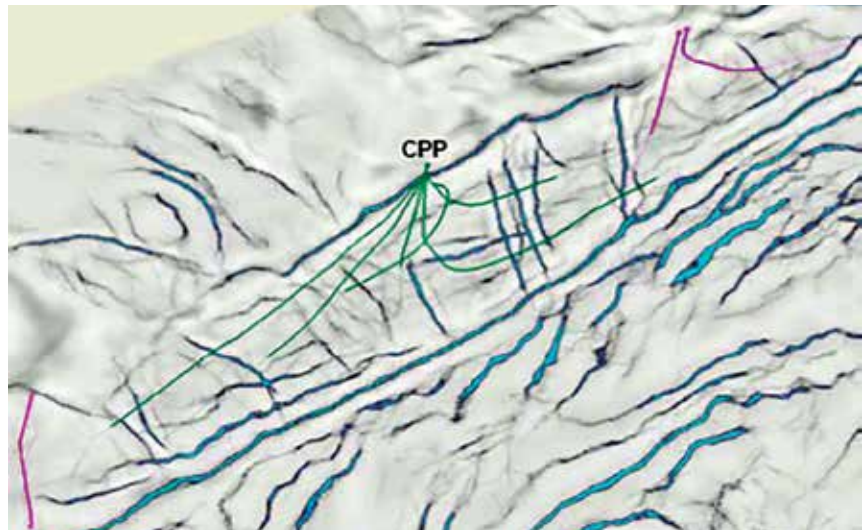


Figure 1. Faults can be nicely identified and tracked on a depth slice using ant-tracking attribute in Su Tu Den structure.

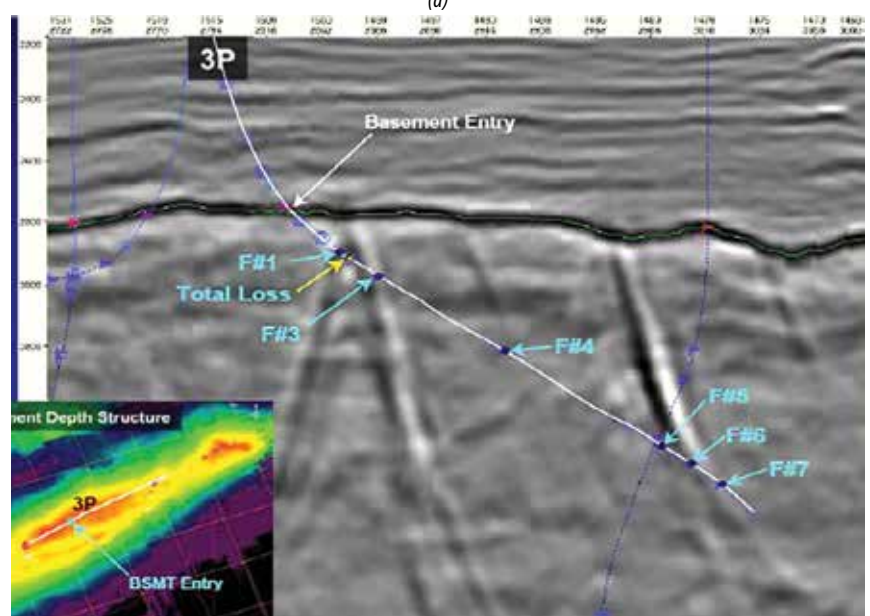
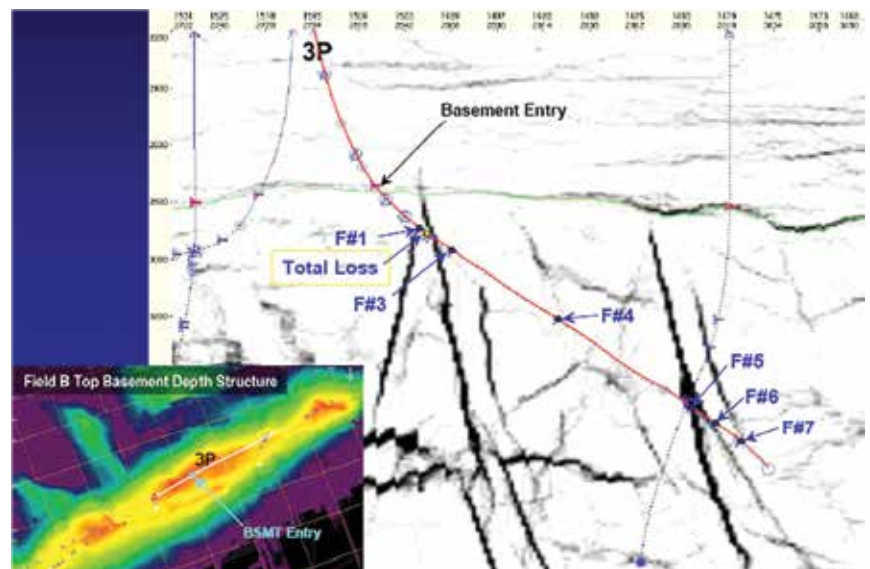
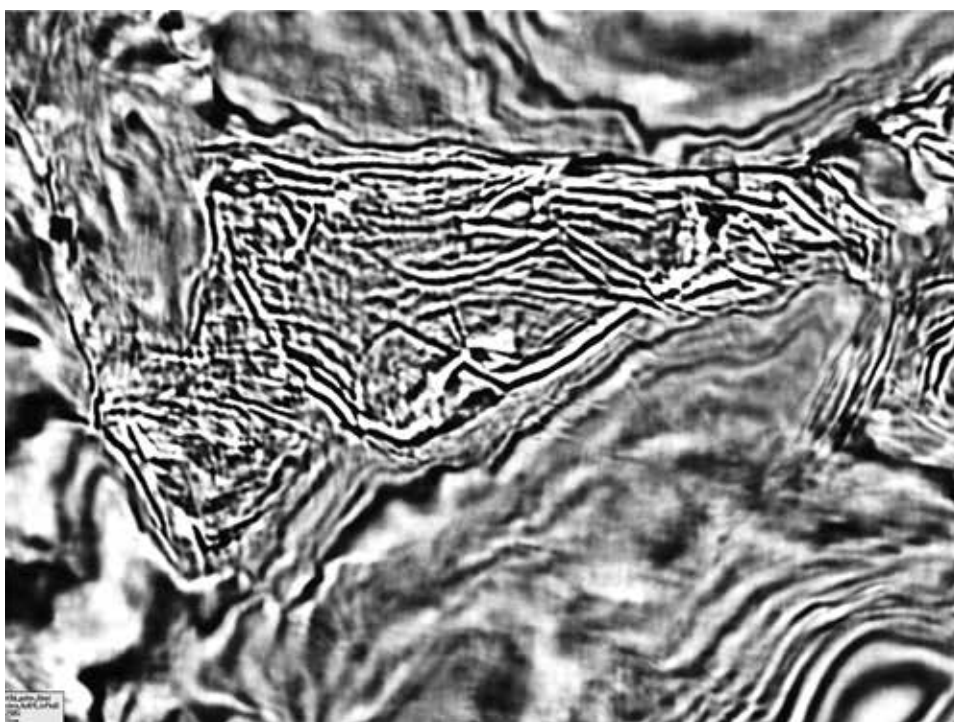


Figure 2. The faults (if real) on ant-tracking attribute (a) can also be observed on conventional seismic data (b).

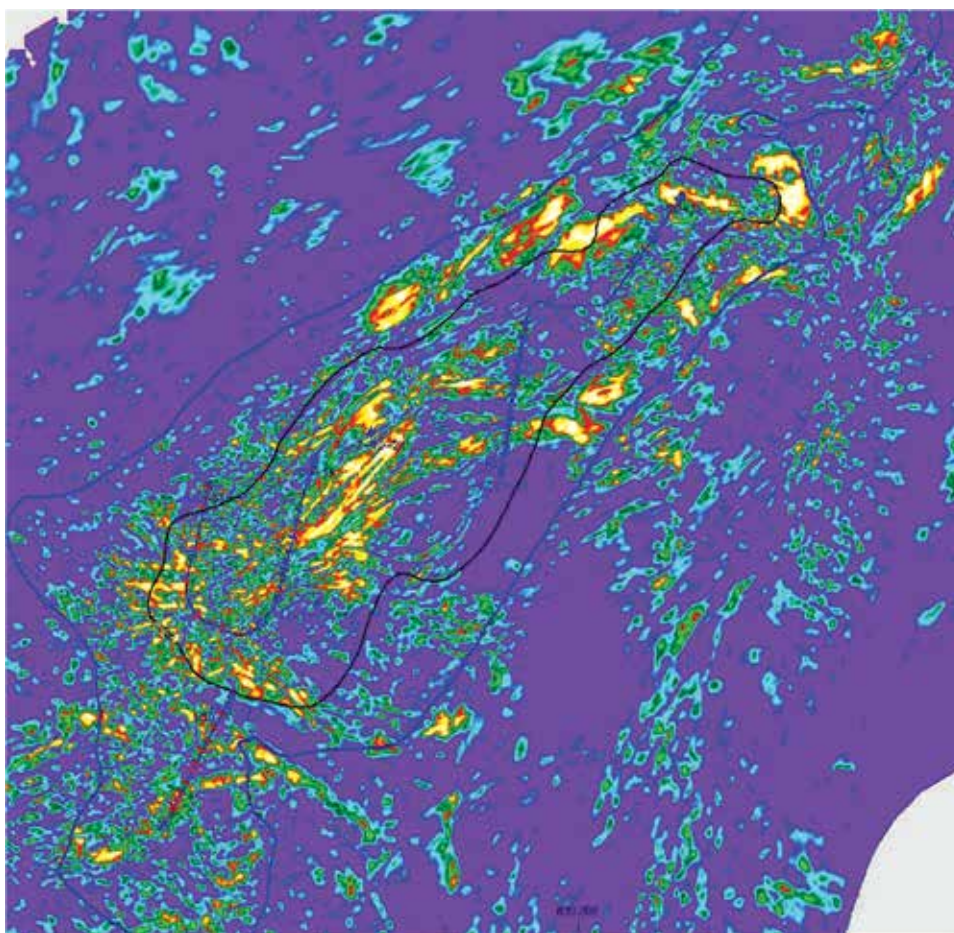
the inconsistency between the ant-tracking attribute and fractures measured by well data.

The explanation for these inconsistencies was the low signal to noise ratio (SNR), since there are no reflection boundaries inside the basement. The information only comes from diffractions at fault planes or fracture zones that are usually weak and much more difficult to image. ANN in combination with seismic attributes was also employed in Bach Ho field [13] in order to try to extract more consistent information but the results were still mixed, as it matches in some areas and does not match in others.

Beside the problem with noise, it was realised that artefacts also potentially cause pitfalls. Some of the previous “successful cases” turned out to be inaccurate or even misleading due to the false lineaments inside the basement generated by CBM technique. For example, some wells drilled into the “fractured zones” and crossing the “faults” predicted by seismic attributes of CBM data in Hai Su Den field were not actually penetrating fractures or faults as expected (Figure 3). The operating company now mainly relies on well information and surface signatures to design the



(a)



(b)

Figure 3. All time slice (a) and variance attributes at 550m below the top basement (b) of CBM cube used to predict faults and fracture zones inside the basement.

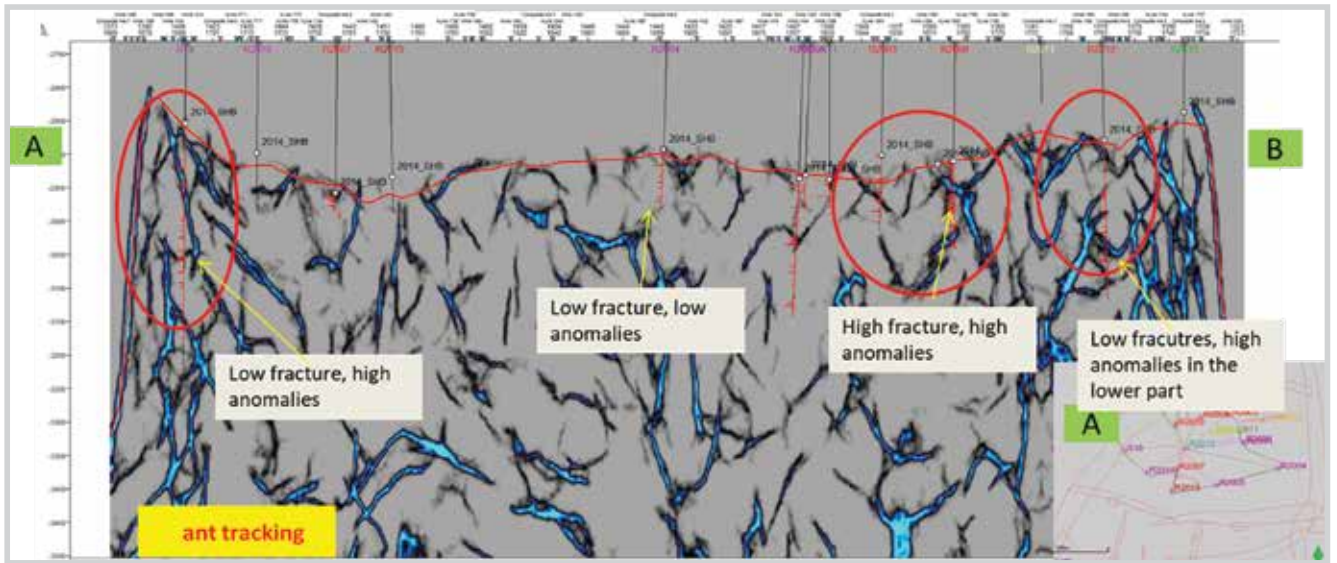


Figure 5. Ant-tracking attribute anomalies are inconsistent with well data in Rong field.

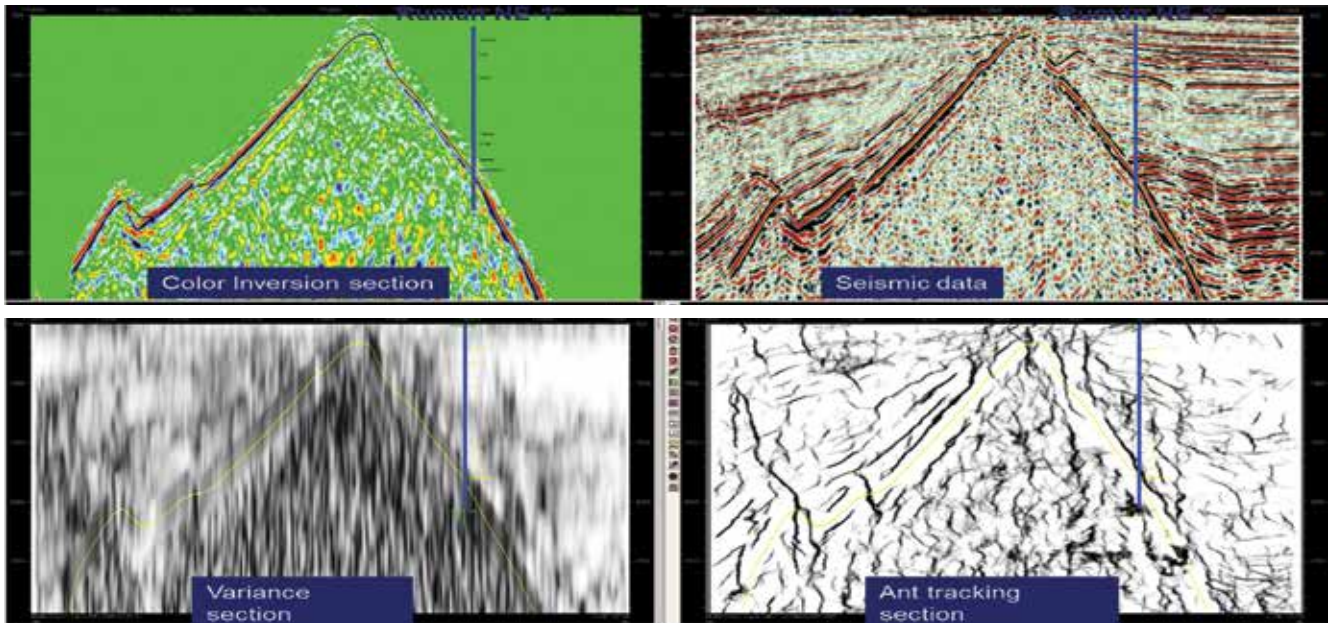
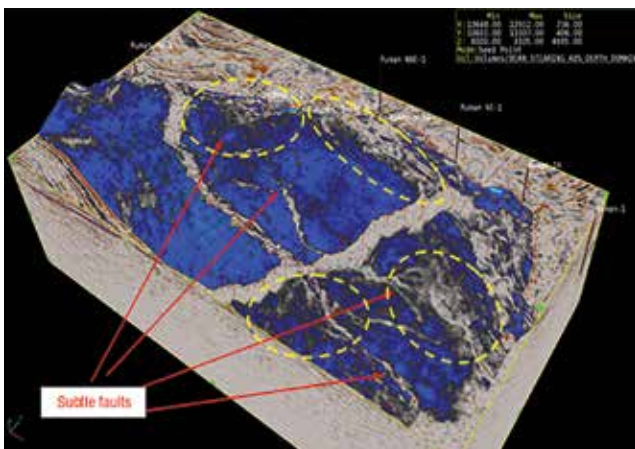
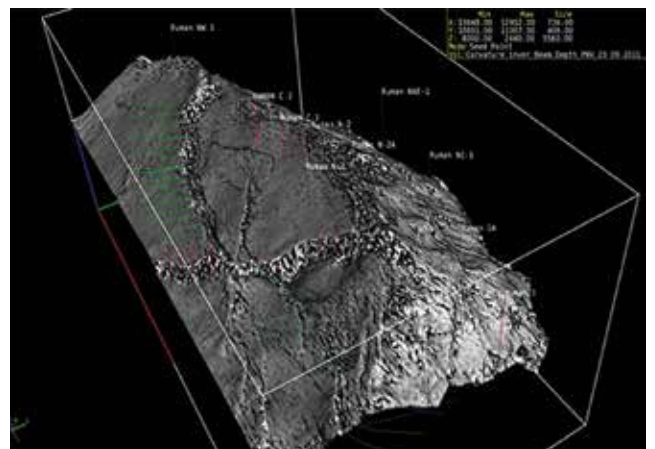


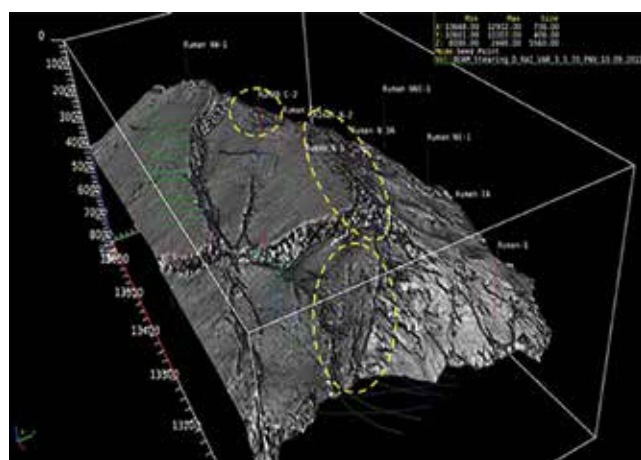
Figure 6. Different attributes show no signature of faults inside the basement due to low SNR.



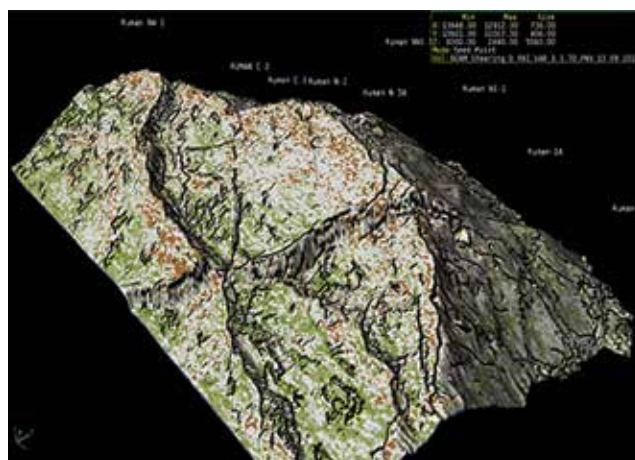
(a) RMS amplitudes and dip & azimuth properties along the top basement. Strong reflections are in blue, low reflectivity areas are in gray (marked as yellow dash ellipse).



(b) Dip & azimuth and curvature properties along the top basement. Dark areas indicate rough surface.

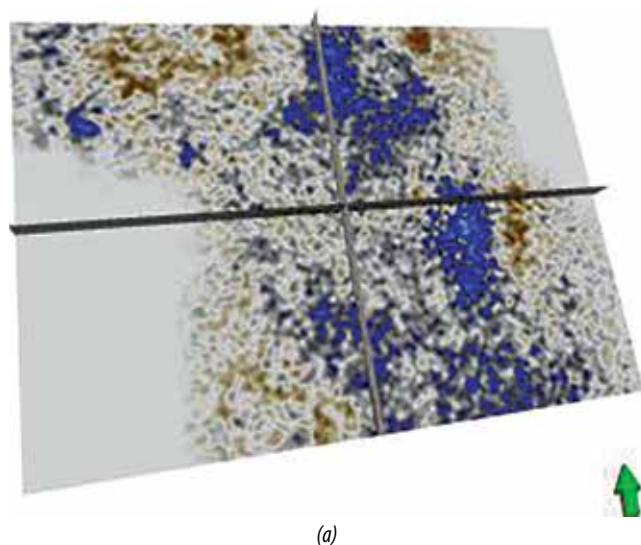


(c) The same as (b) but overlaid by ant-tracking attribute that shows consistent features and enhances the subtle fault prediction.

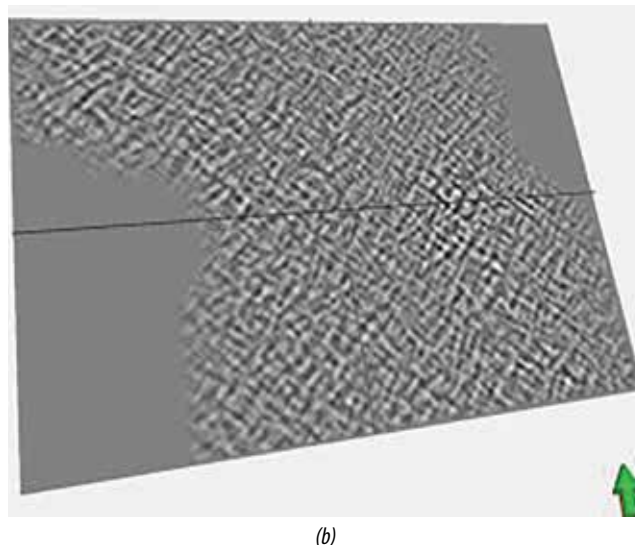


(d) Coherency and ant-tracking attributes at the top basement. Low coherency areas (displayed in green) well collocate with ant-tracking and RMS anomalies in (a) that indicate possible fracture zones.

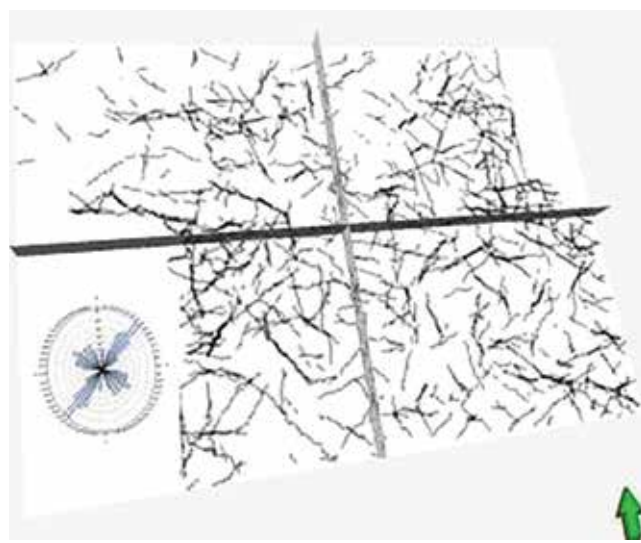
Figure 7. Combination of different attributes extracted along the top basement horizon to aid the interpretation of subtle faults and fracture zones inside the basement.



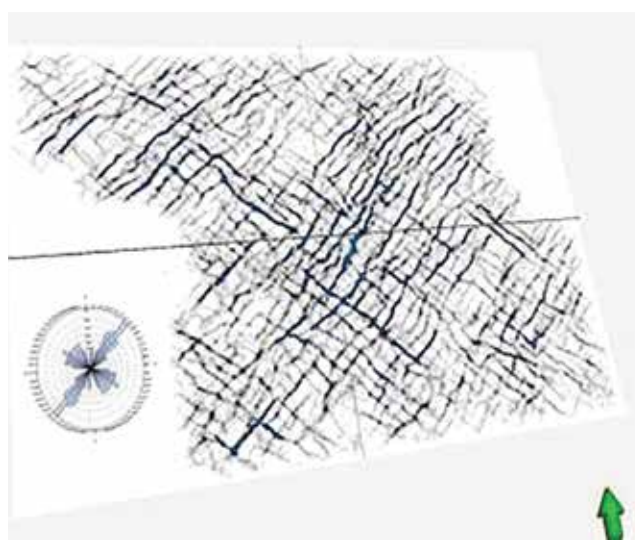
(a)



(b)



(c)



(d)

Figure 8. Seismic cube (a); Fourth orthogonal component (b); Conventional ant-tracking shows random pattern while ant-tracking calculated using the fourth component (c); Emphasises the fracture network consistent with the fracture direction measured from wells (d).

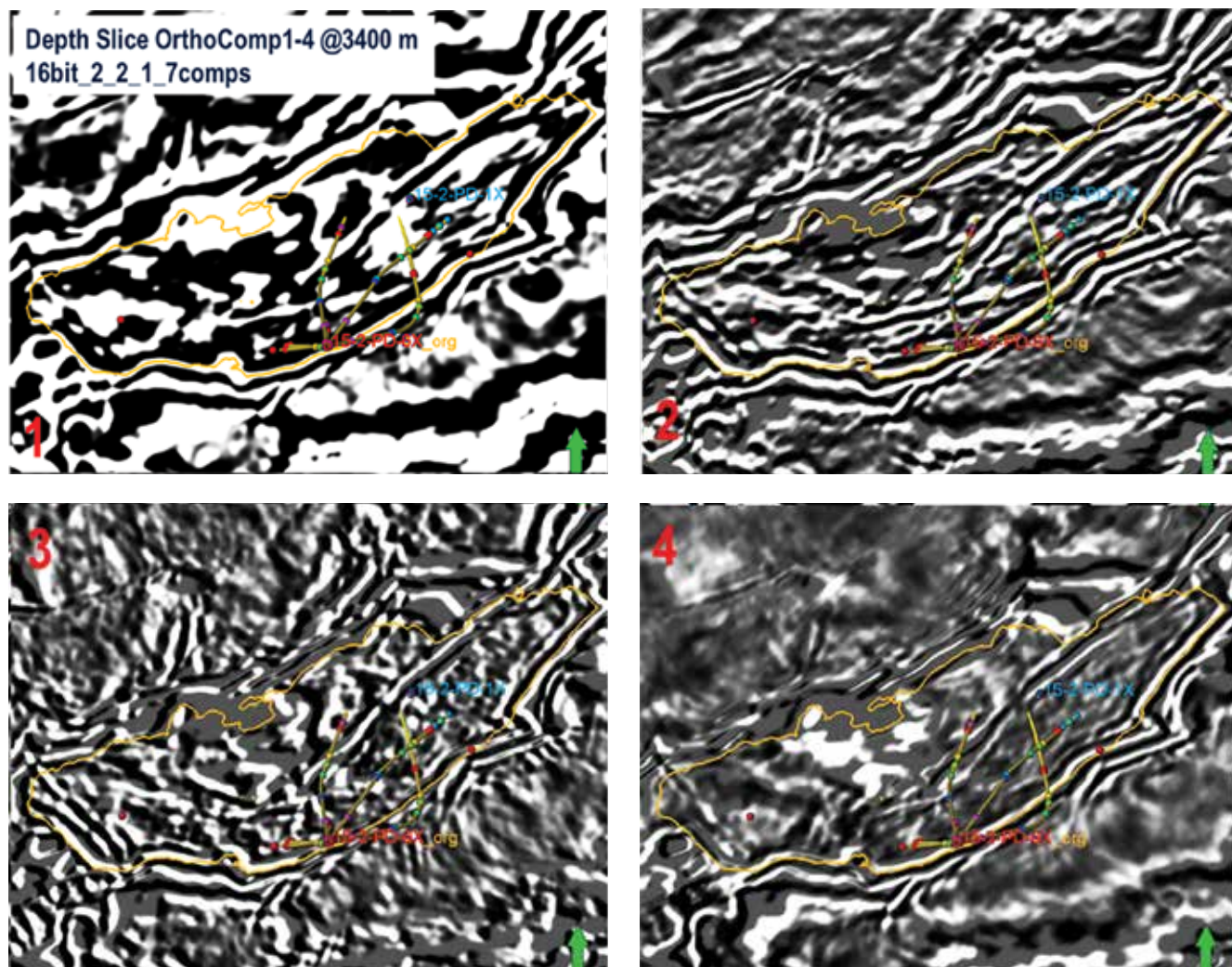


Figure 9. Time slices at 3,400ms of four PCA components of a basement structure in Cuu Long basin show different characteristics that can be analysed with seismic attributes to predict the faults and fractures.

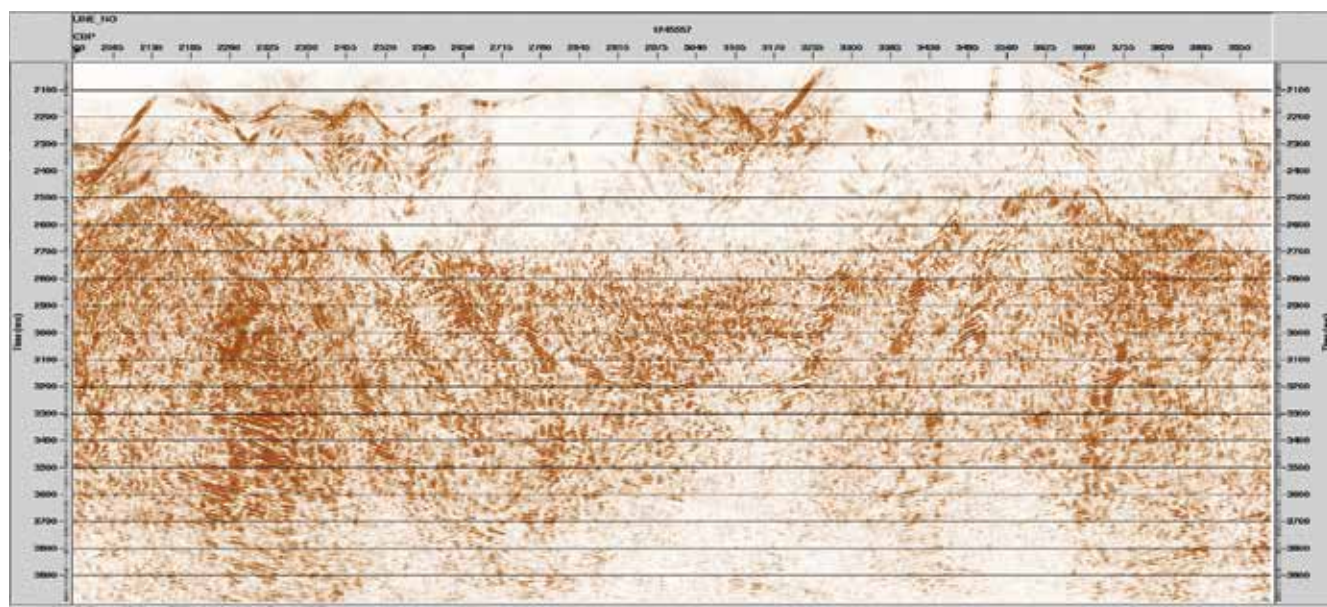


Figure 10. Seismic diffractions remain when reflections have been removed from the data (intermediate results at Vietnam Petroleum Institute).

The color scheme has been chosen to best demonstrate the geological features. Interestingly, subtle fault traces on the top basement that were unable to detect on conventional data (Figure 7) become apparent and consistent on surface attribute data (Figure 8).

Common independent attributes that are recommended to combine for interpretation of subtle faults are RMS amplitudes, dip & azimuth, curvature, coherency and ant-tracking. The interpretation is considered reliable if they give consistent signatures of fault traces and anomalous zones on the top basement surface. The RMS amplitude, dip & azimuth and curvature attributes are sensitive to surface rugosity while coherency, curvature and ant-tracking well respond to subtle faults [10, 11]. Other attributes such as variance, chaos, similarity, etc. can also be useful to combine to enhance the predictability providing that they are independent. Yet it should be noted that the surface attributes avoid the zones affected by noise and artefacts (i.e. below the top

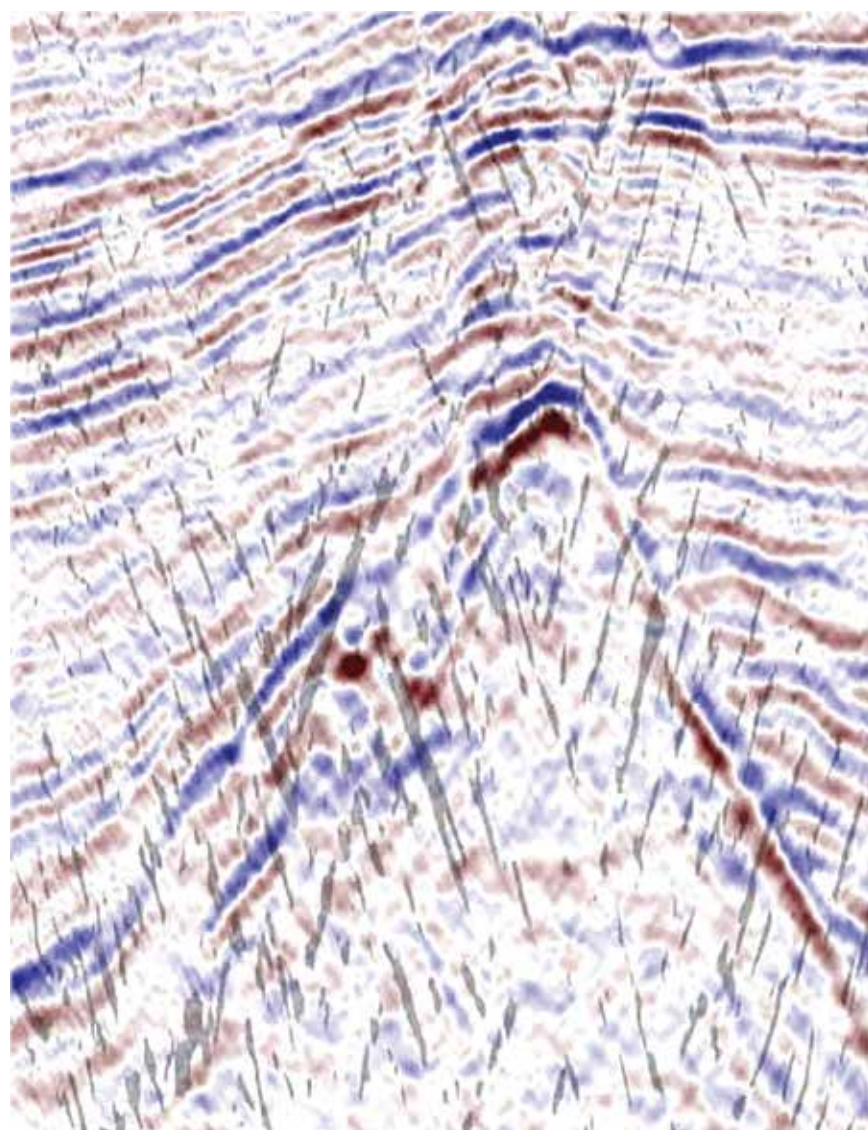


Figure 11. Diffraction data (grey) overlaid with conventional seismic volume showing diffraction events imaging faults that are visible as terminations on the seismic horizons and inside the basements (intermediate results at Vietnam Petroleum Institute).

basement) thus on the other hand they also overlook the invaluable information contained within these zones.

4. Principal component analysis

Principal component analysis (PCA) was introduced decades ago to aid the detection of subtle features on seismic data [14, 15]. Recently it becomes more popular on publications as a tool to separate artefact and noise from the latent features such as subtle faults and fractures [16, 17]. Generally, PCA decomposes the original seismic data into orthogonal components with uncorrelated properties, therefore noise, artefacts and latent responses from geological features can be separated into different component datasets. Well information is usually required to select an orthogonal component useful for fracture detection.

Priezzhev and Scollard [16] used 3D orthogonal decomposition of a seismic cube flattened along the target layer to detect fractures and subtle faults under strong noise conditions. The applied technique computes eigenvalues and eigenvectors of the 3D autocorrelation function of the original data to generate orthogonal 3D components that sum up very closely to the original cube. Figure 8 reproduced from [16] shows that the ant-tracking attribute of conventional seismic data (Figure 8a) has rather random pattern (Figure 8c) due to high noise level while the ant-tracking attribute of the PCA fourth component (Figure 8b) emphasises the fracture network consistent with the well information (Figure 8d).

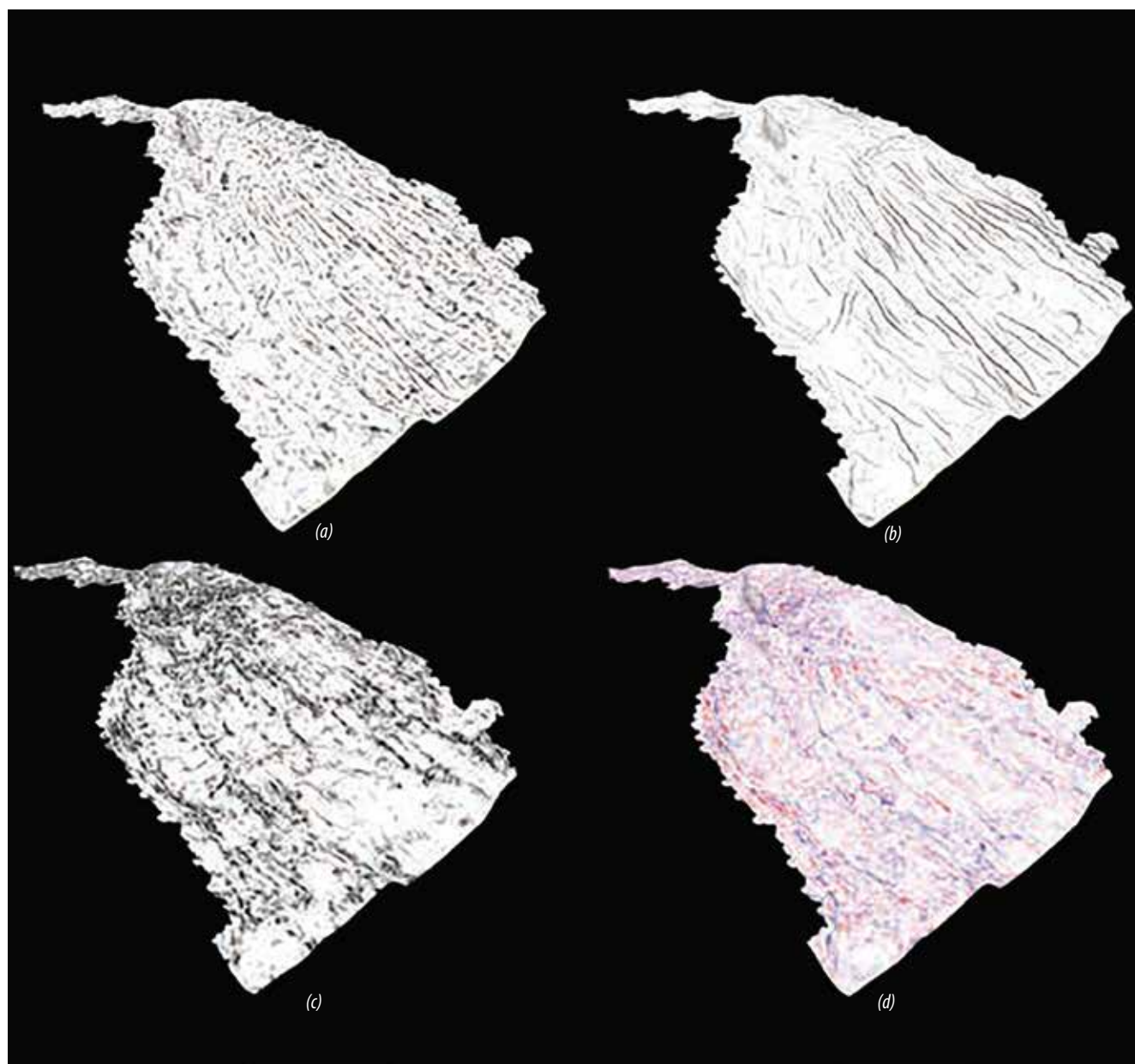


Figure 12. Extractions along a target horizon, clockwise from top left: Raw diffraction volume (a); enhanced diffraction volume (b); positive and negative curvature volume (c); similarity volume (d).

The PCA technique has also been preliminarily tested by the authors for a basement structure in Cuu Long basin as illustrated in Figure 9 where PCA components show different characteristics that can be analysed with seismic attributes to predict the faults and fractures. As mentioned before, information from well data in the studied area must be used to calibrate with these components to enhance the credibility.

5. Diffraction imaging

The analysis techniques described in previous sections are to deal with seismic data that already contaminated by noise and artefacts. Diffraction imaging is a method that

increases the SNR at the processing stage by focusing on diffracted responses from faults and fractures [18].

According to Benfield, et. al. [18], conventional seismic data are biased to the higher amplitude from clear continuous reflection events for structural interpretation when faults are interpreted as breaks in the reflection events. Diffraction imaging workflows aim to achieve the opposite, which is to attenuate the reflectors, leaving behind any focused diffraction events that may be owing to real geological phenomena such as faults, unconformities and depositional discontinuities. Figure 10 shows a seismic diffraction section with reflection signals

removed, the data then can be processed in different ways to generate the diffraction volumes.

A seismic line through a basement structure in Cuu Long basin was initially processed at Vietnam Petroleum Institute using diffraction imaging technique provided by Emerson Paradigm as shown in Figure 11. The diffractions (grey lineaments) are overlaid on conventional reflection volume to show that faults indicated by the diffraction pattern well aligning with the seismic amplitude discontinuities. Additionally, there are diffraction lineaments that are parallel to the clearly imaged faults and go through the top basement. These can be interpreted as faults or fractures inside the basement revealed by the diffraction imaging technique.

Figure 12 reproduced from Benfield et al. [18] compares the diffraction data (Figures 12a and b) along a horizon with conventional post-stack attributes curvature (Figure 12c) and similarity (Figure 12d). Apparently, more lineation features are visible on the diffraction data but all three attributes consistently indicate a complex network of lineaments that can be interpreted as subtle faults and fractures. This diffraction imaging technique is therefore a promising tool to target the noise problems of the data portion beneath the top basement horizon.

6. Conclusions

In the last 20 years seismic attribute analysis has been widely applied to predict fault and fracture reservoir inside the basement in Cuu Long basin. A review of previous studies shows that although seismic attributes have great potential to reveal latent geological features of the basement, the very low signal to noise ratio (SNR) and the presence of artefacts can cause inaccurate or even misleading interpretations. This could be the main reason why in recent years seismic attribute analysis is much less applied for fractured basements than a decade ago.

To improve the effectiveness of seismic attributes in prediction of fracture reservoirs in the basement, three approaches to reduce the influence of noise and artefacts were proposed. The simplest way is to focus on the top basement surface instead of the section below it. A selective combination of independent attributes can be used to delineate fault traces and anomalous zones related to rough reflecting boundaries on the top basement. To utilise the information under the top basement, principal component analysis (PCA) can be

employed to separate noise and artefacts from the data, in this case, well information is essential to verify the PCA component of use. Ultimately, the SNR in the basement can be increased directly during the data processing with diffraction imaging technique. The processed data can then be analysed by seismic attributes to predict fractures and faults or overlaid on conventional data to aid the interpretation.

References

1. PVN. *Reserve assessment report of Hai Su Den - Hai Su Trang fields*, Block 15-02/1. 2015.
2. PVN. *Reserve assessment report of Ruby - Diamond - Topaz fields*, Block 01&02. 2013.
3. PVN. *Reserve assessment report of Su Tu Den - Su Tu Vang fields*, Block 15-1. 2015.
4. Stein Inge Pedersen, Trygve Randen, Lars Sonneland, Øyvind Steen. *Automatic fault extraction using artificial ants*. SEG Technical Program Expanded Abstracts. 2002: p. 512 - 515.
5. Tom Cox, Krista Seitz. *Ant tracking seismic volumes for automated fault interpretation*. 2007 CSPG/CSPE GeoConvention, Calgary, Alberta, Canada. 14 - 17 May, 2007.
6. G.Bone, N.T.Giang, D.N.Quy, V.N.An, D.Pham, J.Sun, Q.Tang. *Improvements in seismic imaging in fractured basement, Block 15-1, offshore Vietnam*. Fractured Basement Reservoir, Petrovietnam. 2008; 4: p. 63 - 69.
7. Don Pham, Jason Sun, James Sun, Qingbing Tang, Graeme Bone, Nguyen Truong Giang. *Imaging of fractures and faults inside granite basement using controlled beam migration*. ASEG Extended Abstracts. 2007; 1: p. 1 - 5.
8. Saleh Al-Dossary, Kurt J.Marfurt. *3D volumetric multispectral estimates of reflector curvature and rotation*. Geophysics. 2006; 71(5): p. 41 - 51.
9. P.Scholtz. *Coherence calculation of different seismic attribute traces for fault interpretation*. European Association Of Geophysical Exploration. 1996; 61: p. 65.
10. Satinder Chopra, Kurt J.Marfurt. *Seismic attributes for fault/fracture characterization*. SEG Technical Program Expanded Abstracts. 2007: p. 1520 - 1524.
11. E.J.H.Rijks, J.C.E.M.Jauffred. *Attribute extraction: An important application in any detailed 3-D interpretation study*. The Leading Edge. 1991; 10(9): p. 11 - 19.

12. PVN. *Reserve assessment report of Rong field, Block 09-1*. 2014.
13. PVN. *Reserve assessment report of Bach Ho field, Block 09-1*. 2017.
14. David C.Hagen. *The application of principal components analysis to seismic data sets*. *Geoexploration*. 1982; 20(1-2): p. 93 - 111.
15. J.R.Scheevel, K.Payrazyan. *Principal component analysis applied to 3D seismic data for reservoir property estimation*. *SPE Reservoir Evaluation & Engineering*. 1999; 4(1): p. 64 - 72.
16. Ivan Priezzhev, Aaron Scollard. *Fracture detection through seismic cube orthogonal decomposition*. *Society of Exploration Geophysicists (SEG) Technical Program Expanded Abstracts*. 2013: p. 1308 - 1313.
17. Poorandokht Soltani, Mehrdad Soleimani, Hamid Aghajani. *Faults and fractures detection in 2D seismic data based on principal component analysis*. *International Journal of Mining and Geo-engineering*. 2017; 51(2): p. 199 - 207.
18. N.R.Benfield, A.Guise, D.Chase. *Diffraction imaging - a tool to reduce exploration and development risk*. *First Break*. 2016; 34(3): p. 57 - 63.

Predicting hydrocarbon migration and accumulation in Block 09-3/12, Cuu Long basin by 3D petroleum system modelling

Nguyen Huy Giang¹, Bui Huy Hoang¹, Nguyen Van Kieu¹, Pham Viet Au²

¹Vietnam Petroleum Institute, ²Vietsovpetro

Email: giangnh@vpi.pvn.vn

Summary

Block 09-3/12 is located to the southeastern margin of the Cuu Long basin. Up until now five wells have been drilled in the block, resulting in discoveries at two fields, Soi Main and Central A. In this study, 3D petroleum system modelling has been used for determining the kitchen areas as well as evaluating hydrocarbon migration and accumulation for the remaining prospects in Block 09-3/12. The petroleum system modelling indicates that the Oligocene source rock is the major source for the prospects in Block 09-3/12. The kitchen area for the Central and Western A structures is the East Bach Ho trough, while the kitchen in the Southeast Soi area is the main source for the Southeast A structure. The simulation results predict the presence of oil accumulations in Lower Miocene and Oligocene reservoirs for the A structure.

Key words: Petroleum system modelling, A prospect, drainage area, hydrocarbon migration and accumulation, Block 09-3/12.

1. Introduction

Block 09-3/12 covers an area of 5,559km² and lies in the southeast portion of the Cuu Long basin (Figure 1). The water depth is about 10 - 50m. The study area has several oil discoveries in Lower Miocene and Oligocene sandstones. The success of Soi-1X in the Soi Main prospect and especially the A-2X, 3X and 4X wells in the Central A prospect proves that there is an active petroleum system in the area.

Detailed 3D basin modelling of Block 09-3/12 focuses on the A structure and covers all of the potential fetch area of the source kitchen. The aim of 3D basin modelling is to investigate the migration and charge history of the recent discoveries and help predict where other accumulations in Lower Miocene and Oligocene plays lie on the remaining prospects in the Western A and Southeast A area (Figure 1).

2. Geological setting

The tectono-structural characteristics of Block 09-3/12 and adjacent areas are influenced by the tectonics of the Cuu Long basin. The Cuu

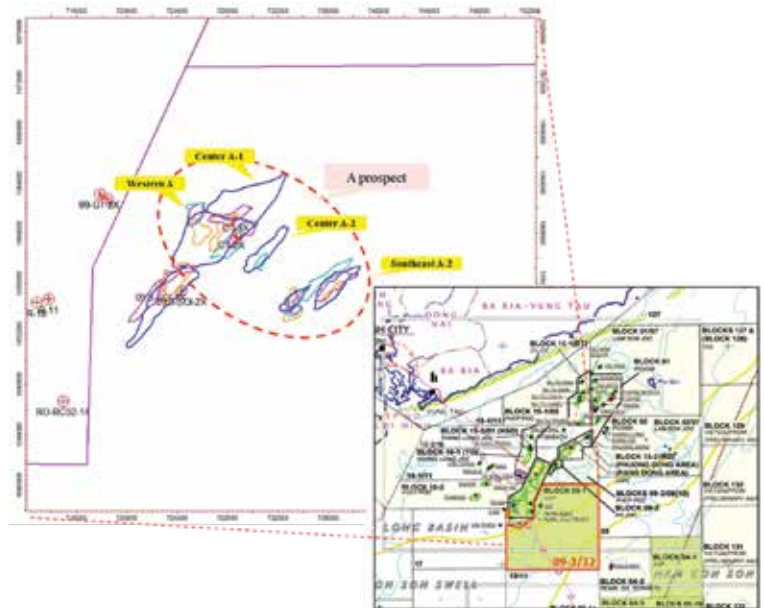


Figure 1. Location of Block 09-3/12.

Long basin is an oval-shaped, early Tertiary rift basin, located on the southern continental shelf of Vietnam. It is separated from the Gulf of Thailand basins to the west by the Khorat High and from the Nam Con Son basin to the southeast by the Con Son swell. Block 09-3/12 encompasses the East Bach Ho trough and the Southeast slope (Figure 2).

The geological evolution of the Cuu Long basin can be divided into 3 episodes: pre-rift (Pre-Tertiary), syn-rift (Eocene to Oligocene), and post-rift (Miocene - Present) (Figure 3). The pre-rift period saw

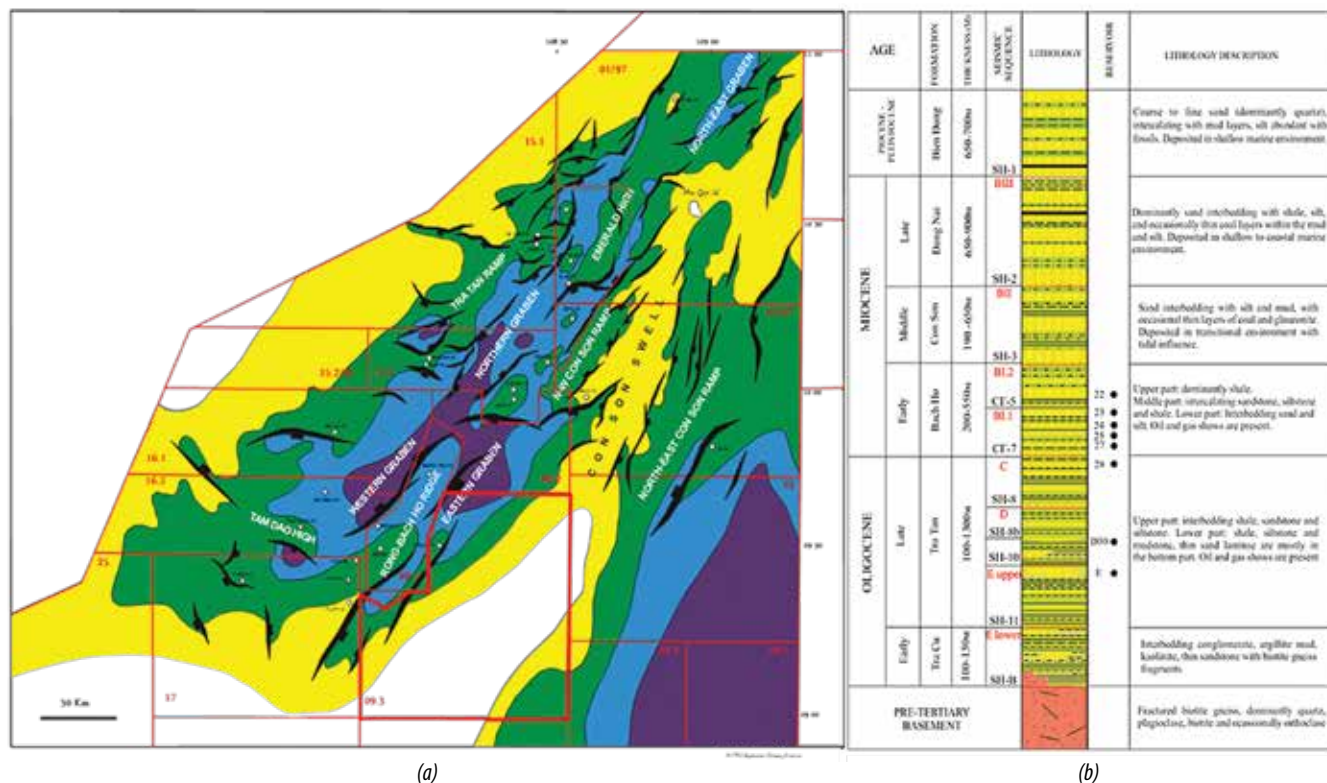


Figure 2. The structural map with major structural components (a) and the general stratigraphic column (b) of Block 09-3/12 [1]. The study area is highlighted.

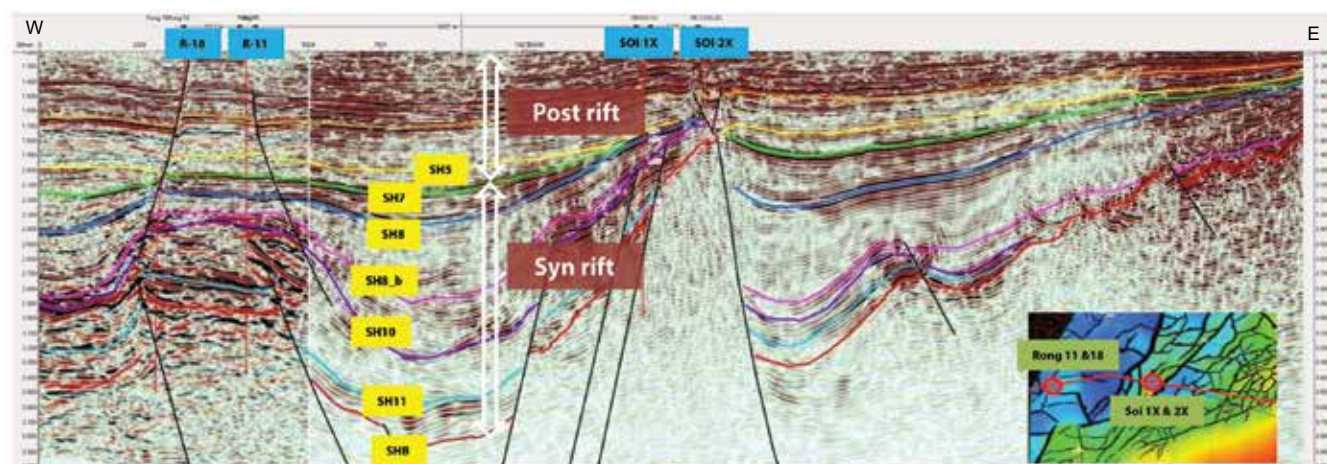


Figure 3. A seismic cross-section through the study area [1].

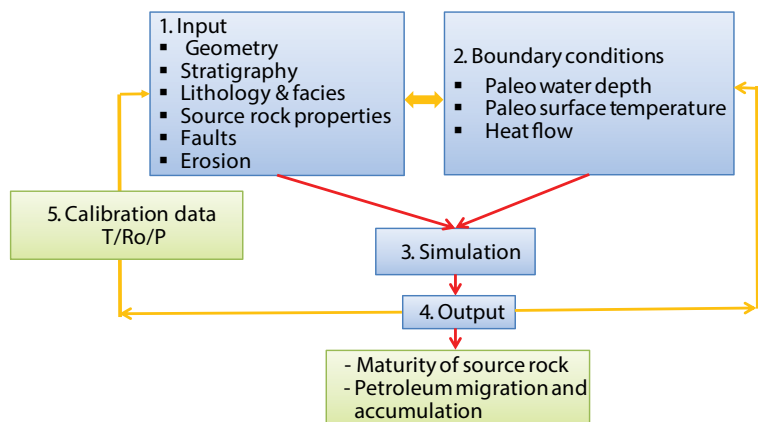


Figure 4. Workflow for 3D basin modelling.

widespread magmatic activities in both the present day onshore and offshore, which formed the crystalline basement for the basin. During the Oligocene, syn-rift basins were initially filled with coarse-grained alluvial to fluvial sand-dominant sediments, represented by the F and lower E sequences. During the Late Oligocene, lacustrine environment dominated, resulting in forming the E and D shale sequences, which are the main source rocks in the basin, as well as in Block 09-3/12. A compressional phase in the Late Oligocene

took place which fractured the basement and created folding and reverse faulting, which is observed in much of the basin. The post rift starts from the Early Miocene, from which point the whole basin enters the thermal sag phase, dominated by fluvio-marine to shallow marine environments [1].

3. Methodology and model input

- Methodology

The method of modelling used combines geological, geophysical, geochemical and petroleum system data [2]. The modelling process using the PetroMod software aims to determine the maturity of source rocks, and model migration and accumulation processes of hydrocarbon through geological time based on the 3D petroleum systems modelling workflow (Figure 4).

- Construction of 3D structural model

The 3D structural model includes the main horizons and fault surfaces. There are 08 horizons interpreted from seismic data: Top Basement (SH-B), Top Lower Oligocene (SH-11), Top Intra Upper

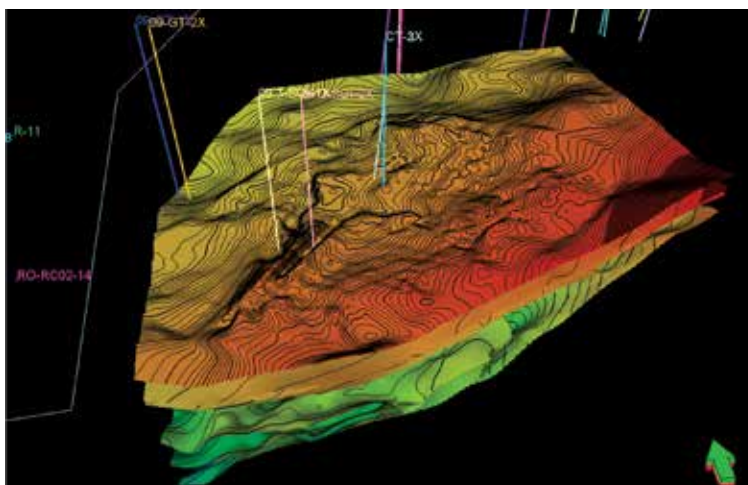


Figure 5. The 3D view of grids of 8 main horizons derived from seismic interpretations.

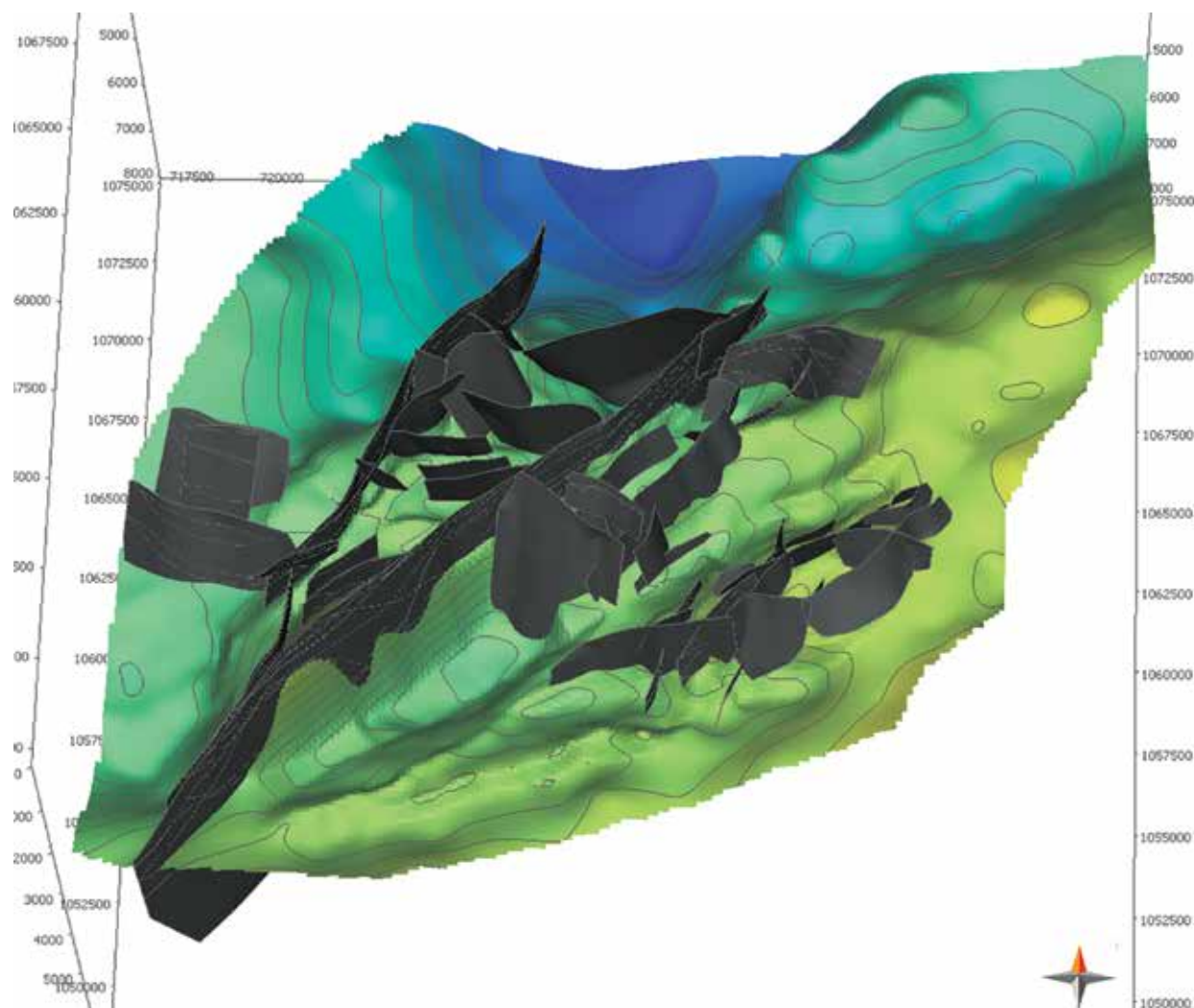


Figure 6. The 3D view of fault plane used for modelling.

Oligocene (SH-10), SH-8b, SH-8, Top Upper Oligocene (SH-7), Top Intra Lower Miocene (SH-5), and Top Lower Miocene (SH-3) (Figure 5). The fault systems in the study area are mostly normal faults trending NE-SW, and a number of small faults trending NW-SE or E-W. In total, there are about 50 main faults chosen to be included in the 3D petroleum system model to simulate the entrapment and migration of hydrocarbon along fault surfaces (Figure 6). The structural model is constructed by PetroMod 3D in the depth domain.

- Source rock properties

The geochemistry analysis results of samples from wells in Block 09-3/12 and the surrounding area show that mature Oligocene sediment is the main source rock with good to very good generation potential [3]. The average TOC values of Oligocene source rock vary from 3 - 5%wt, and HI values higher than 400mgHC/gTOC. Oligocene source rock, which is shale deposited in fluvial-deltatic and lacustrine environments, contains mainly kerogen type I and mixture of type I and III. In contrast, Lower Miocene sediment is not good enough to become source rock because it is immature and has low organic matter richness (Figures 7 and 8) [4].

- 1D well modelling and Heat Flow

The 1D petroleum system model and heat flow are the controlling factor of the maturation modelling in the 3D petroleum system model. The 1D petroleum system model is built for wells A-2X and A-3X, in which the vitrinite reflectance (%Ro) and well temperature (°C) are used to calibrate the heat flow as well as model output.

In this study, the heat flow profile depends on the onset of rifting phase and subsidence phase. Because Cuu Long basin is a Cenozoic rift basin, the heat flow profile is based on the McKenzie model. Heat flow was low during the Pre-rift phase (about 40Ma) and then increased in rifting phase and peaked at 28Ma. In Lower Miocene (subsidence phase), heat flow has decreased until the present time at 40 - 50mW/m² (Figure 9).

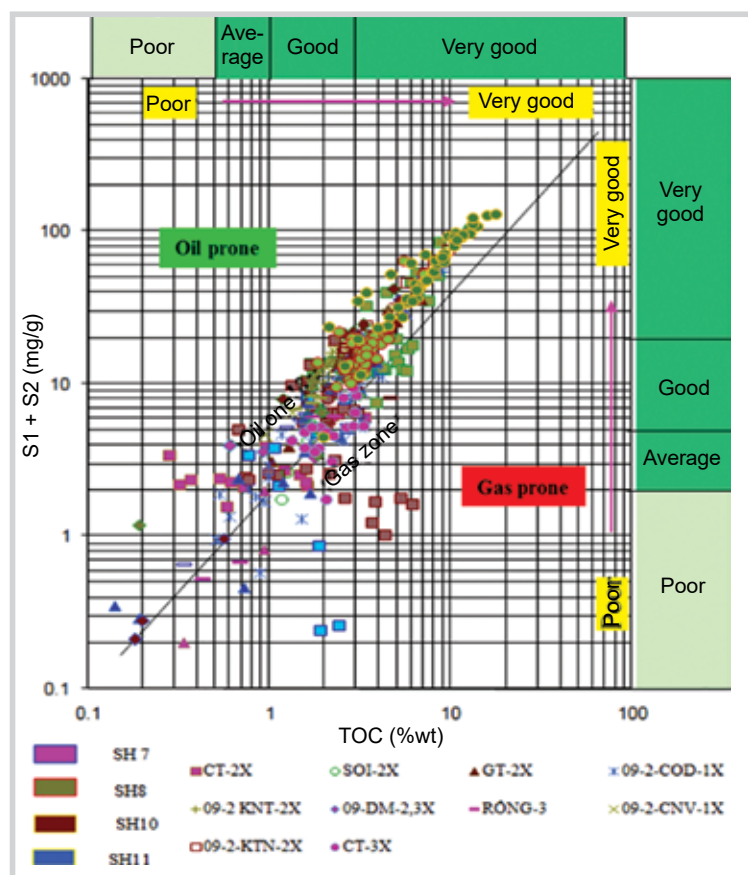


Figure 7. TOC vs (S1+S2) diagram of T20 in Block 09-3/12 and adjacent area, Cuu Long basin.

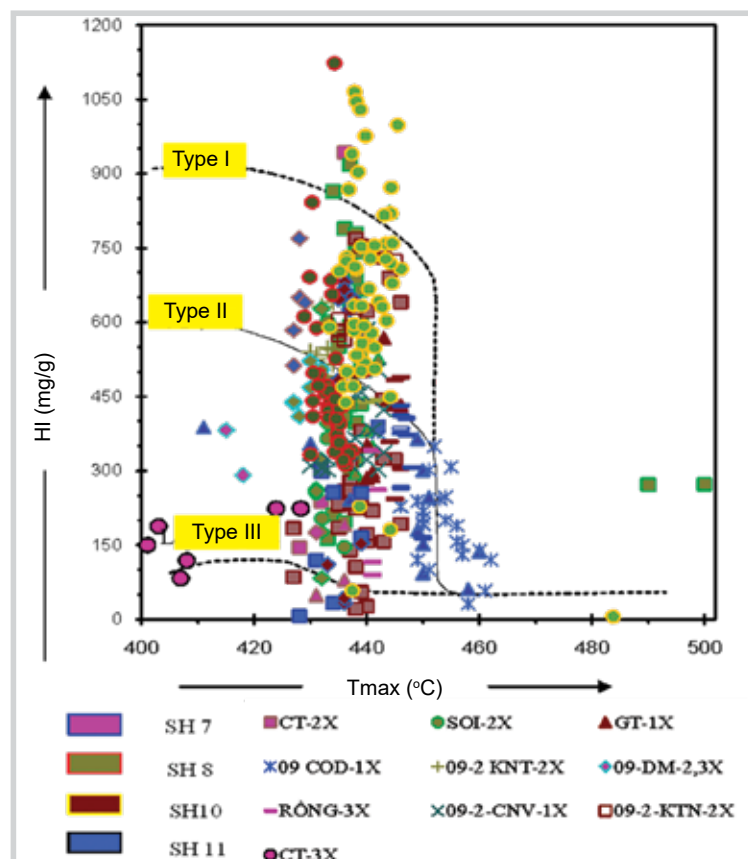


Figure 8. HI vs Tmax diagram of T20 in Block 09-3/12 and adjacent area, Cuu Long basin.

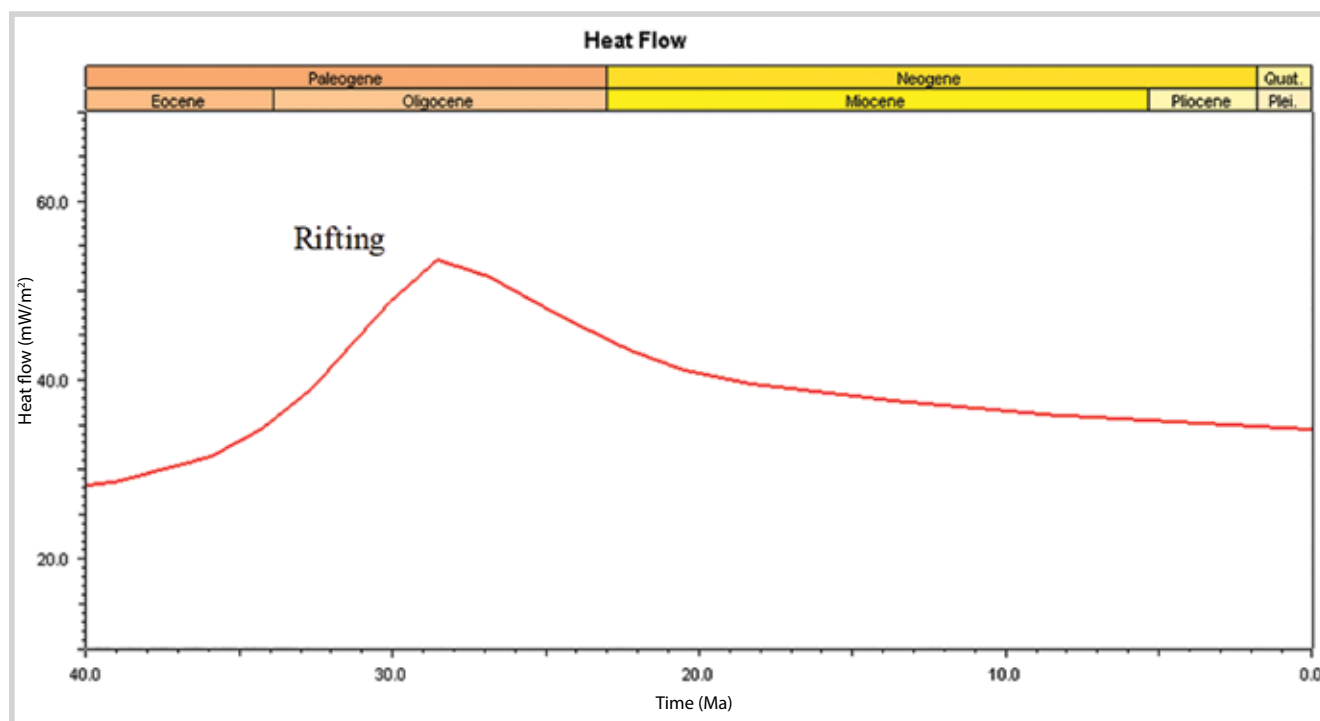


Figure 9. Heat flow curve of study area based on the McKenzie model.

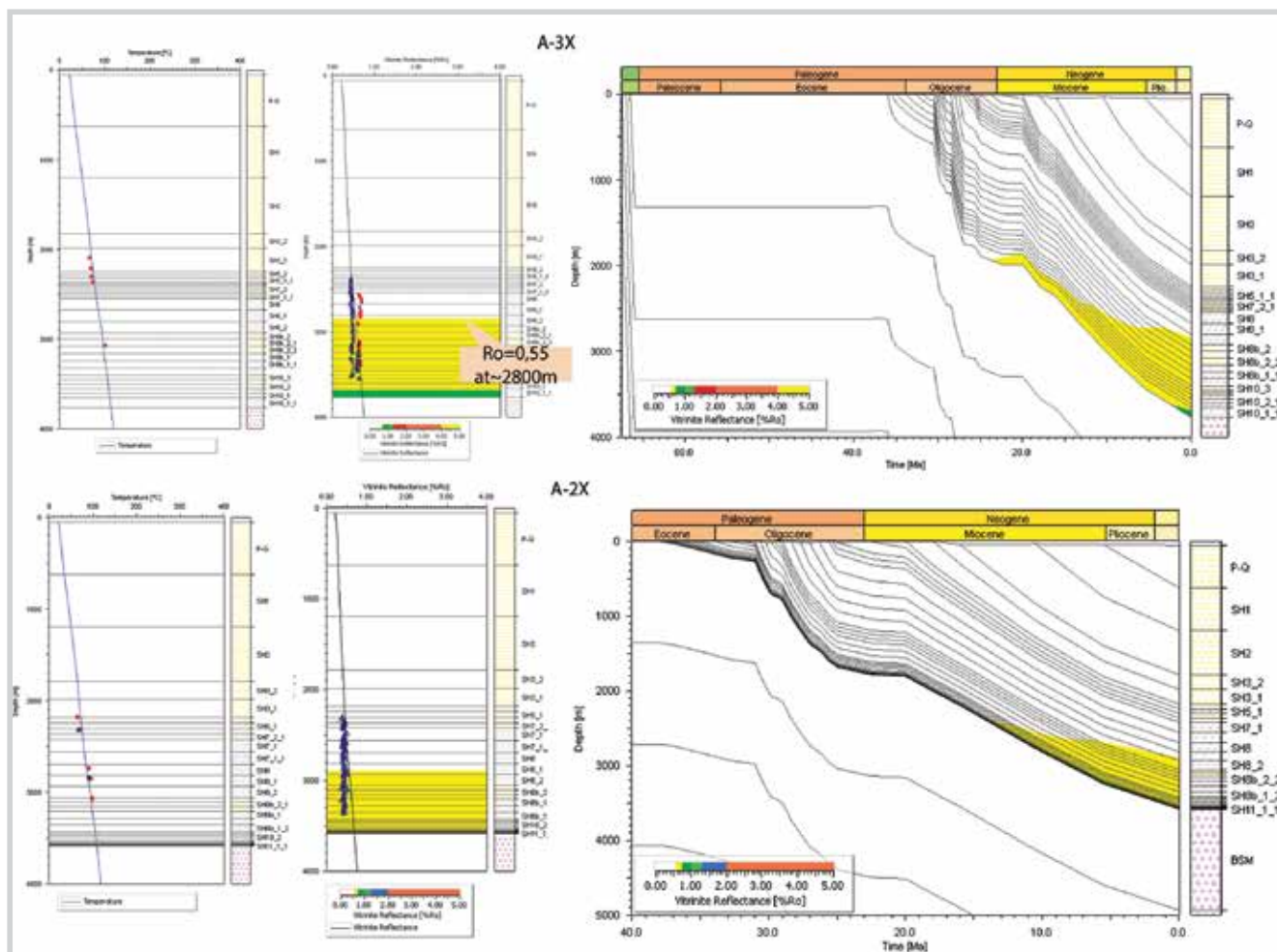


Figure 10. 1D basin modelling at A-3X and A-2X.

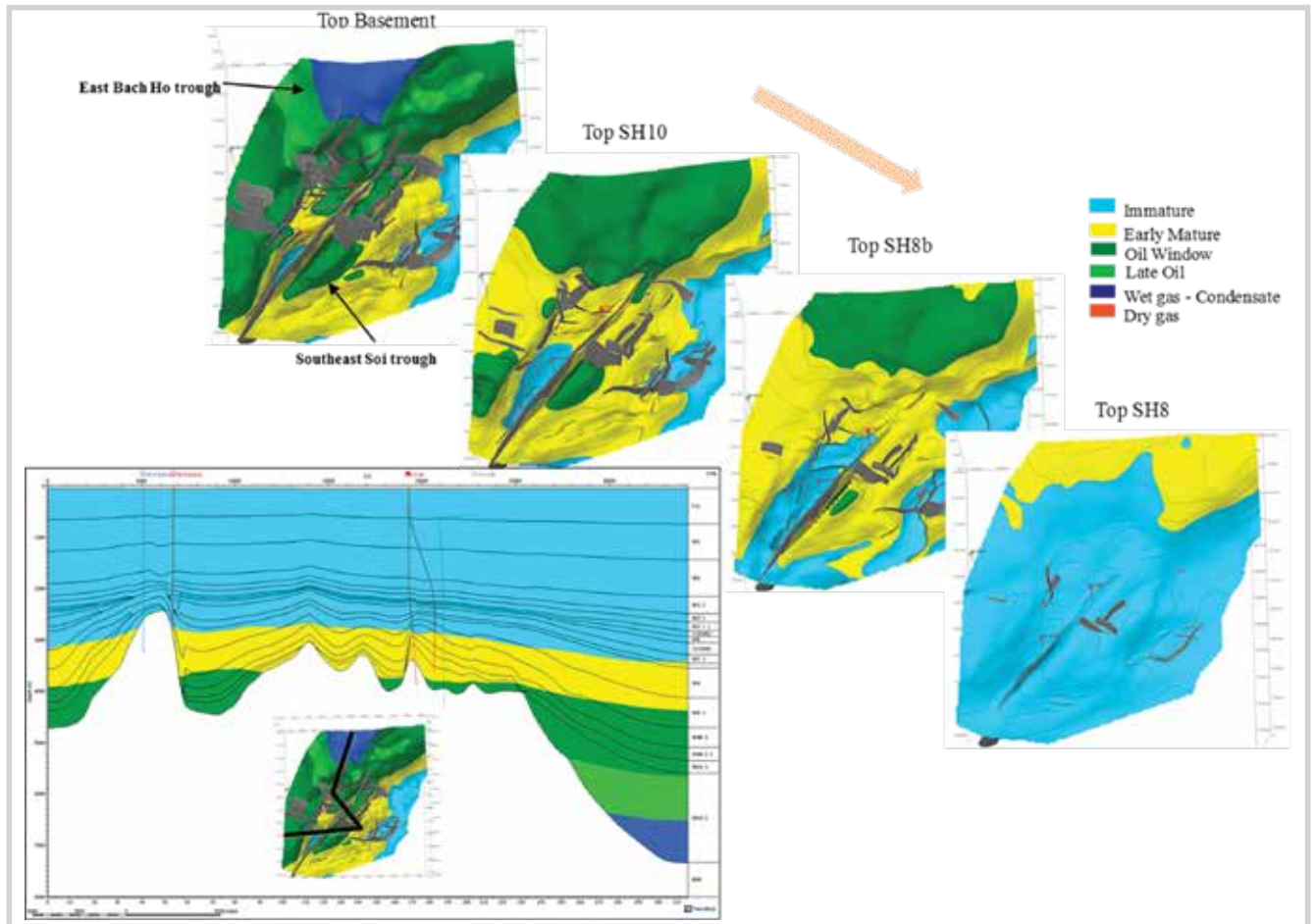


Figure 11. Maturity maps of top basement, SH10, SH8b and SH8.

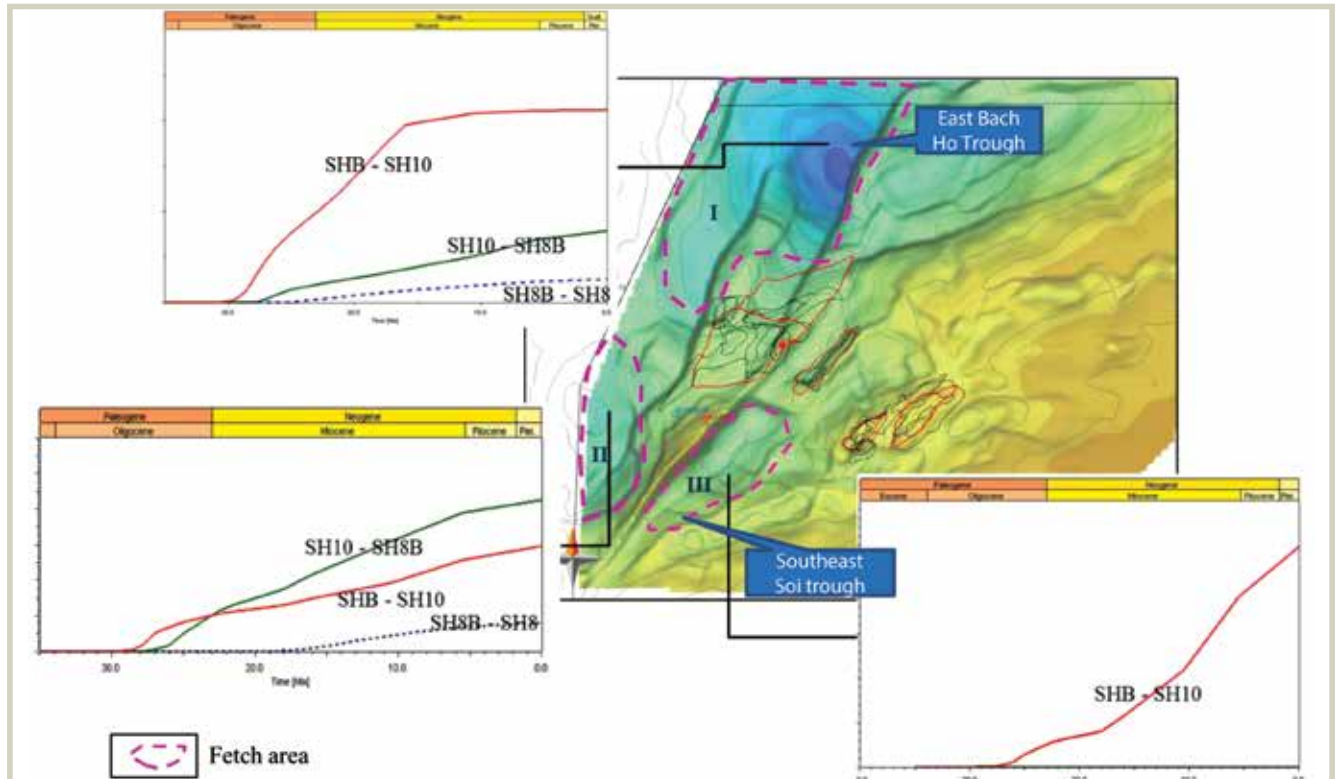


Figure 12. Generation timing of hydrocarbon.

In general, the 1D model results show good agreement between the output and the measured Ro and temperature in the wells (Figure 10). Evaluation of the source rock at the well shows most of the Oligocene source rocks are in the early maturation window.

4. Model results

4.1. Source rock maturity

The start of the maturation depth (0.55 - 0.72%Ro) is about 2,700 - 3,900m; the oil window depth (0.72 - 1.3%Ro) is about 3,520 - 6,500m; and the condensate/wet

gas window depth is from 6,500m. In the study area, there exist 2 main kitchens for the A prospect group, which are the Southeast Soi and East Bach Ho troughs.

The East Bach Ho trough is the main kitchen area, which is currently in the condensate/wet gas stage (1.3 - 2.0%Ro) in the deepest part, while the Southeast Soi trough is just in the oil window with Oligocene source rock (Figure 11).

In general, most of the hydrocarbon accumulations are from the products of the Oligocene source rock. Meanwhile,

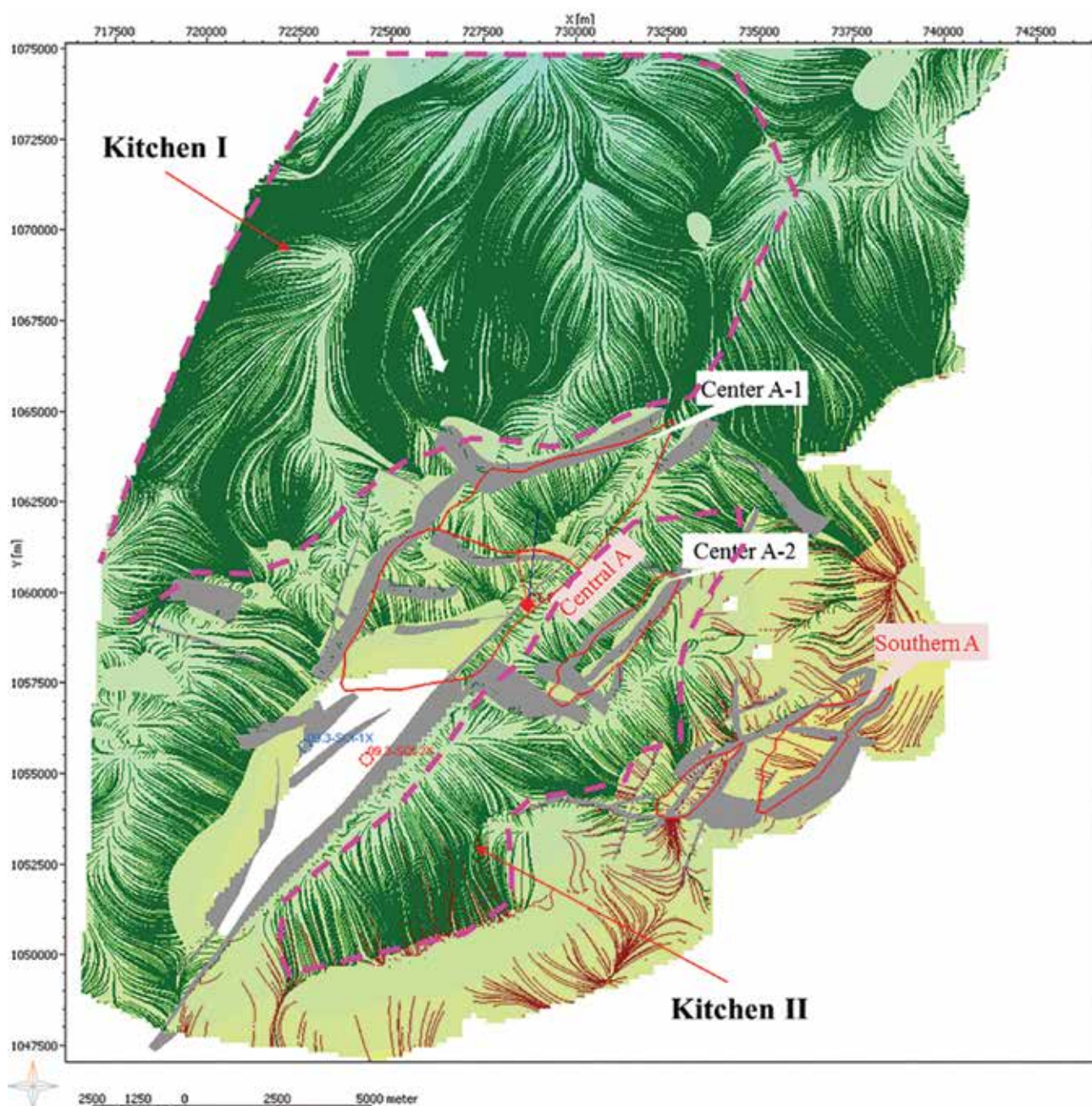


Figure 13. Hydrocarbon migration pathway for Upper Oligocene reservoirs (upper) and 2D cross-section through the A Centre structure (lower).

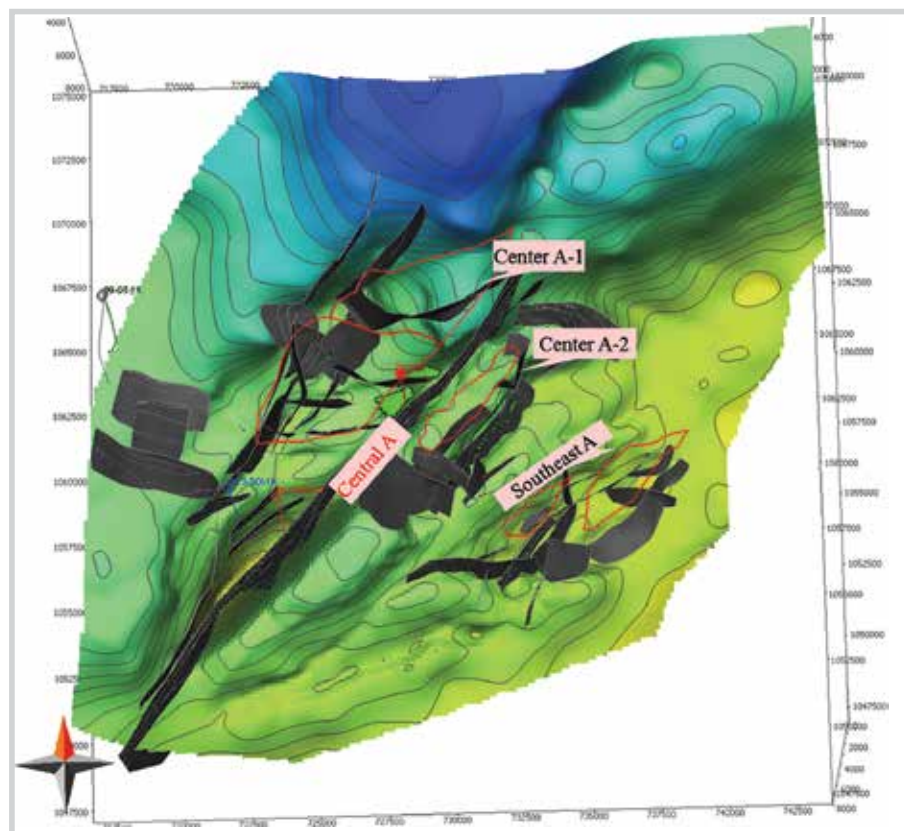


Figure 14. Hydrocarbon accumulation for Upper Oligocene reservoirs.

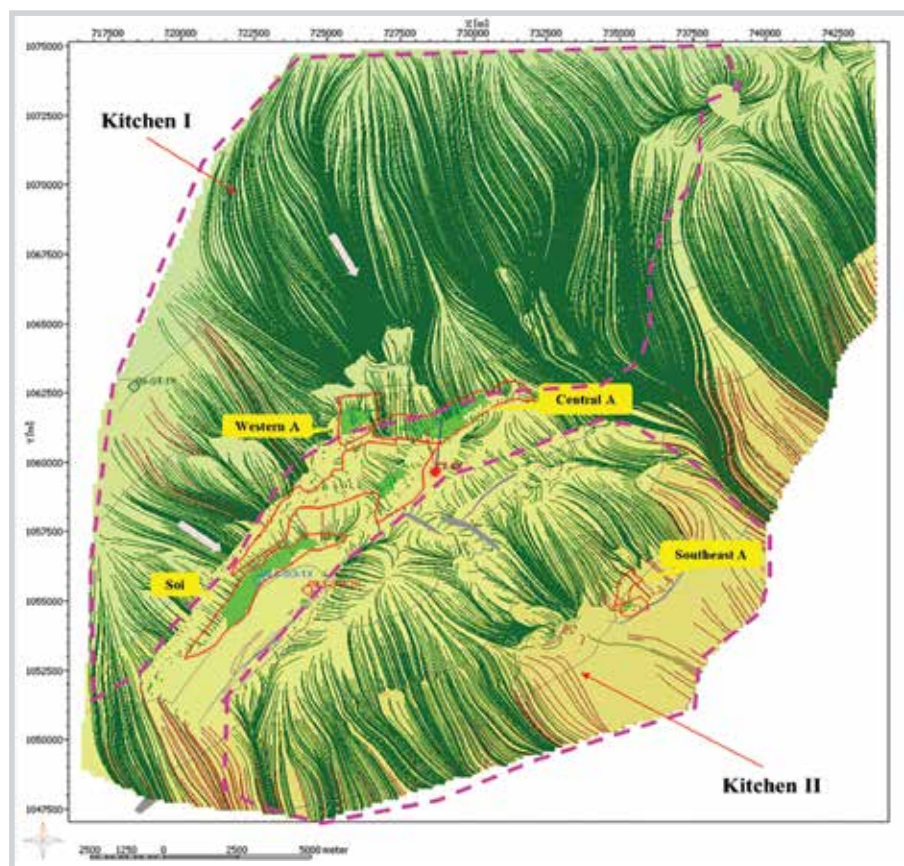


Figure 15. Hydrocarbon migration pathway for Lower Miocene reservoirs (upper) and 2D cross-section through the Soi structure (lower).

the Lower Miocene shale does not meet the requirements for an effective source rock in the study area due to low organic matter concentration and low maturity level. Through the source rock maturity and transformation ratio results from the 3D petroleum system modelling, it can be predicted that the source rock in the East Bach Ho trough (area I and II) has gone through different maturity levels and is the main source rock for the study area. The oil and gas generation history from the Upper Oligocene source rock (SHB-SH10) in area I and II (Figure 12) started from about 28Ma; hydrocarbon migration was strong at about 20Ma, until Middle Miocene. For the SH10-SH8 layer, the hydrocarbon generation took place later and peak oil generation varies from Upper Miocene to Pliocene. While in the Southeast Soi trough (area III), only the SHB-SH10 sequence source rock is in the hydrocarbon generation stage.

4.2. Hydrocarbon migration and accumulation

The most important output for the 3D petroleum system model is the restoration of the migration and accumulation process of hydrocarbon from the past to the present [5]. Based on the newest geological interpretation, 3 prospects in the A prospect group are identified, including: Western area, Central area (Blocks Ia, Ib, and II) and Southeast area (Blocks I and II). In the Central area (Blocks Ia and Ib), there are two exploration wells: A-2X and A-3X.

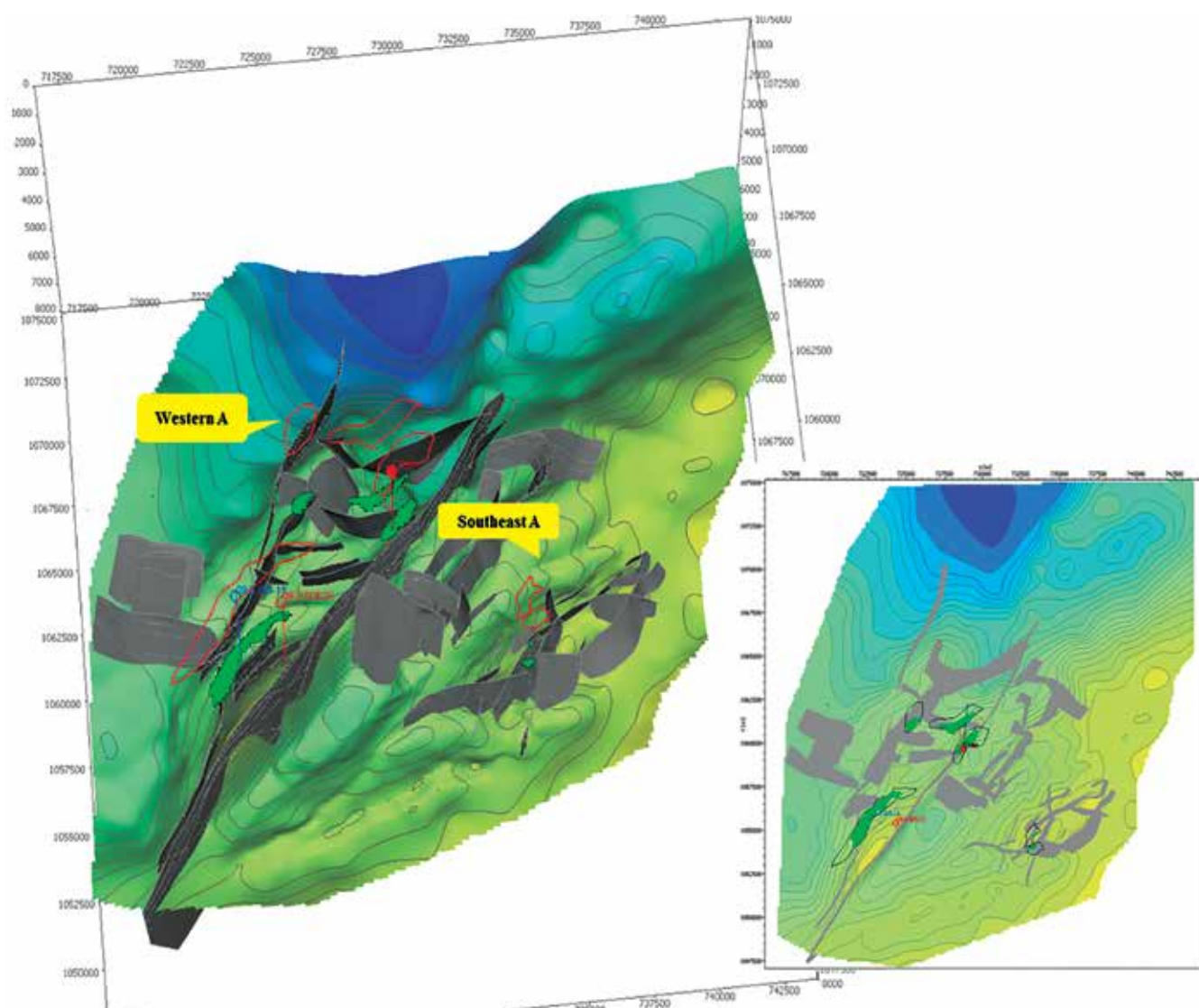


Figure 16. Hydrocarbon accumulation for Lower Miocene reservoirs.

4.2.1. Upper Oligocene reservoir (SH10-SH8b layer)

The results from two wells A-2X and A-3X show that this is an important reservoir in the study area, especially the Central A area. The result of the migration simulation in this region indicates that for the Upper Oligocene reservoir, there are two main kitchen areas: the East Bach Ho trough (Kitchen I) and the Southeast Soi trough (Kitchen II). Kitchen I charges Blocks Ia and Ib, while Kitchen II charges Block II of the Central A cluster as well as the Southeast A cluster (Figures 13 and 14).

Because Kitchen I has a larger extent compared to Kitchen II, and has gone through most of the maturation stages, it has better charge potential than Kitchen II. As a result, Blocks Ia and Ib have better conditions for receiving oil (migration direction denoted by the green

arrows) than Block II of the Central A cluster and also the Southeast structure.

The predictions indicate that the migration and accumulation of hydrocarbon for the Central A-I and II are very favourable and consistent with the results of the A-2X and A-3X. Meanwhile, the Southeast A prospect is predicted by the petroleum system model to contain no hydrocarbon, due to source rock quality risks (Figure 13).

4.2.2. Lower Miocene reservoir

The results of drilling and well tests from A-2X/3X wells have proven the existence of oil bodies in the Upper Oligocene and Lower Miocene interval. The main kitchen area for the prospects in the Lower Miocene section is the Oligocene source rock in the East Bach Ho trough

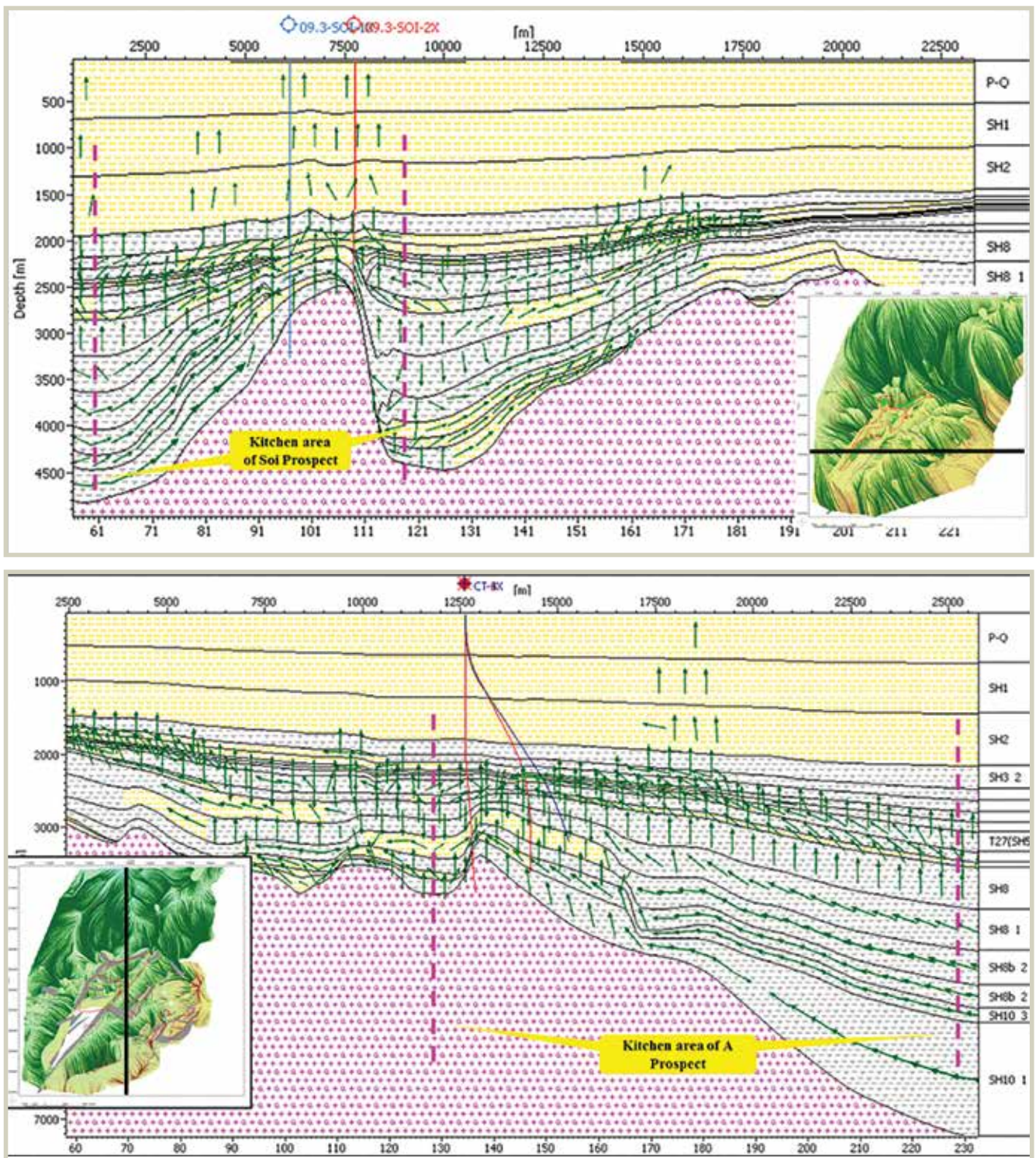


Figure 17. 2D hydrocarbon migration cross-section through the Soi structure (upper) and A Centre structure (lower).

(Kitchen I) (Figure 15). The migration and accumulation model at the Lower Miocene reservoir shows the presence of hydrocarbon in Central & Western A prospect and Soi structure which are mainly provided by the Oligocene source rock from Kitchen I (Figures 16 and 17) while for the accumulation in Southeast A prospect charged by Kitchen II.

In general, based on the results of the 3D Petroleum System Model, for the undrilled structures the Western A and Block II of the Central A prospects are the most favourable for receiving hydrocarbon, with the main kitchen being the East Bach Ho trough. The Southeastern prospect group has lower potential due to limited hydrocarbon pathways and charge volume. This study

was carried out before the drilling of well A-3X and its conclusions contributed to the decision of the well location. A-3X was a discovery, which is consistent with the study's results.

5. Conclusions and recommendations

In particular, the Oligocene source rock in the East Bach Ho trough is the main hydrocarbon source for the Central and Western A prospect group. Meanwhile the source rock in the Southeast Soi trough provides hydrocarbon for the Southeastern prospect group.

The early maturation threshold of the source rock is at about 2,700 - 3,900m, the oil window is at about 3,500 - 6,500m, and the condensate/wet gas window is below 6,500m. The oil and gas generation history from the Upper Oligocene source rock in the East Bach Ho trough started from about 28Ma. Hydrocarbon migration was strong at about 25Ma, until Middle Miocene. For the SH10-SH8 layer, the hydrocarbon generation took place later, from Lower Miocene to the present. In the Southeast Soi trough, only the SHB-SH10 sequence source rock is in the hydrocarbon generation stage.

The simulation result shows the presence of hydrocarbon (oil) accumulations in Lower Miocene

and Oligocene reservoirs for the Central and Western A structure, and in Lower Miocene for the Southeastern structure. Among those, Western A and Block II of the Central A structure have the most favourable conditions for hydrocarbon migration and charge.

References

1. VSP. *Cơ sở địa chất lựa chọn vị trí giếng khoan A-4X Lô 09-3/12*. 2016.
2. Armin I.Kauerauf, Thomas Hantschel. *Fundamentals of basin and petroleum systems modeling*. Springer. 2009.
3. VPI. *Báo cáo địa hóa mẫu vụn và mẫu dầu - Giếng khoan A-3X*. 2016.
4. Kenneth E.Peters, Clifford C.Walters, J.Michael Moldowan. *The Biomarker Guide, Volume 2: Biomarkers and isotopes in petroleum systems and earth history*. Cambridge University Press. 2005.
5. Lê Hải An. *Tổng hợp tài liệu Địa chất - Địa vật lý và chính xác hóa tiềm năng dầu khí sau khi khoan giếng khoan A-2X*. VSP. 2015.

Sources, mechanism and prediction method of scale formation in oil production in Vietnam

Kieu Anh Trung¹, Nguyen Minh Quy¹, Hoang Long¹, Truong Van Dung¹, Le Thi Thu Huong¹, Pham Thi Thuy², Vu Huu Huy²

¹Vietnam Petroleum Institute, ²Hoan Vu Joint Operating Company

Email: trungka.epc@vpi.pvn.vn

Summary

This paper presents the typical sources and mechanism of scale formation in oil production in Vietnam. A workflow of prediction method to find scale formation during oil production was presented. The main sources of scale problem in oil production are incompatible mixing between different water sources and the change of pressure/temperature along the production system. A case study using the prediction method was also introduced in the article. The decrease of productivity index of the observed well can be caused by the dominant build-up of scale at downhole. Based on the mechanism of scale formation, a suitable scale control strategy was given.

Key words: Scale formation, scale prediction, water production, productivity index.

1. Introduction

Today, the problem of inorganic scaling becomes more and more serious in many oil fields in Vietnam, such as Bach Ho, Te Giac Trang, Ca Ngu Vang, Rang Dong, and Su Tu Vang. Few production problems strike fear into the hearts of engineers the way scale can. Scale is an assemblage of deposits that cake perforations, casing, production tubing, valves, pumps and downhole completion equipment, thereby clogging the wellbore and preventing fluid flow. Scale, just like the scale found in home plumbing or tea kettles, can be deposited all along water paths from injectors through the reservoir to surface equipment. Most scales found in oil fields in Vietnam form either by direct precipitation from the water that occurs naturally in reservoir rocks, or as a result of produced water becoming oversaturated with scale components when two incompatible waters meet downhole. Whenever an oil or gas well produces water, or water injection is used to enhance recovery, there is the possibility that scale will form.

The buildup of scale inside wellbore and production equipment (both subsurface and surface) has badly affected oil production efficiency, causing millions of dollars in damage every year. Scale can develop in the formation pores near the wellbore and reduce formation porosity and permeability. It can block the flow by clogging perforations or forming a thick lining in

production tubing. It can also coat and damage downhole completion equipment, such as safety valves and gas-lift mandrels. The productivity index can fail half in just several weeks and therefore that requires serious study of scale problem to find out the suitable cures [1].

In this article, we present the mechanism and source of scale buildup during oil production. Knowing the conditions that lead to scaling and when and where it occurs helps in understanding how to prevent and/or remove scale to restore long-term well productivity. A scaling assessment job that has been done at an offshore oil field by the Vietnam Petroleum Institute (VPI) and Hoan Vu Joint Operating Company (Hoan Vu JOC) will also be presented in this paper as a case study.

2. Main mechanism of scale in oil production

The production of water is a natural consequence of the production of oil and gas from subterranean reservoirs. Water that is present in these reservoirs contains dissolved salts and dissolved gases. Under certain conditions these salts precipitate and become scale deposits [1]. It is not possible to produce oil and gas for any significant time before water is also produced. The water/oil boundary will rise over time and channelling from water permeable zones will cause increased water to be produced. Scales are formed due to precipitation and crystal growth at the water surface. Scale begins to form when the state of any natural fluid is perturbed such that the solubility limit for one or more components is exceeded. Mineral solubility itself has a complicated dependence on temperature and pressure.

Date of receipt: 17/4/2018. Date of review and editing: 17 - 20/4/2018.

Date of approval: 7/5/2018.

There are two basic mechanisms by which scales are formed in the petroleum reservoir [2]:

- Autoscaling

A reservoir fluid experiences changes in temperature and pressure as it is produced. If such changes take the fluid composition beyond the solubility limit for a mineral, it will precipitate as scale, this phenomenon is called autoscaling or self-scaling. Sulfate and carbonate scales can precipitate as a result of pressure changes within the wellbore or at any restriction downhole. Sodium chloride scale (halite) forms in a similar way from highly saline brines undergoing large temperature drops.

Another serious problem occurs when carbonate scales precipitate from produced fluids containing acid gases. Reduction in pressure during production outgases the fluid, which raises pH and causes scale deposition. The deposition of carbonate can extend from the near-wellbore matrix, along tubing and into surface equipment as the produced water continuously changes in pressure and temperature. For carbonate scales, temperature effects often work against pressure effects. For example, the pressure drop at the point of entry into the wellbore can lead to matrix scale. As the fluid progresses up the tubing to surface temperatures and wellhead pressure, the resulting temperature drop may override the pressure effect, reducing scale formation in the tubing. On the other hand, subsequent release of pressure from the wellhead to the surface can lead to massive deposits of scale in surface equipment and tubing.

- Incompatible mixing

Mixing incompatible injection and formation waters can cause scale formation. Seawater is often injected into reservoirs during secondary and enhanced-recovery water flooding operations. Seawater is typically rich in SO_4^{2-} anions with concentrations often above 2,000mg/L (0.02ppg), while formation waters contain divalent cations Ca^{2+} and Ba^{2+} . Fluid mixing in the near-wellbore matrix generally produces new fluids with combined ion concentrations that are above the solubility limits for sulfate minerals. Calcium sulfate (CaSO_4) scale forms in limestone formations, and barium sulfate (BaSO_4) and strontium sulfate (SrSO_4) scales form in sandstone formations. If these scales form in the formation, they are difficult to remove chemically and impossible to remove mechanically. Incompatible water mixing can also occur in tubing, producing scales that are accessible to both chemical and mechanical removal.

- Forming scale

Although the driving force for scale formation may be a temperature or pressure change, out-gassing, a pH shift, or contact with

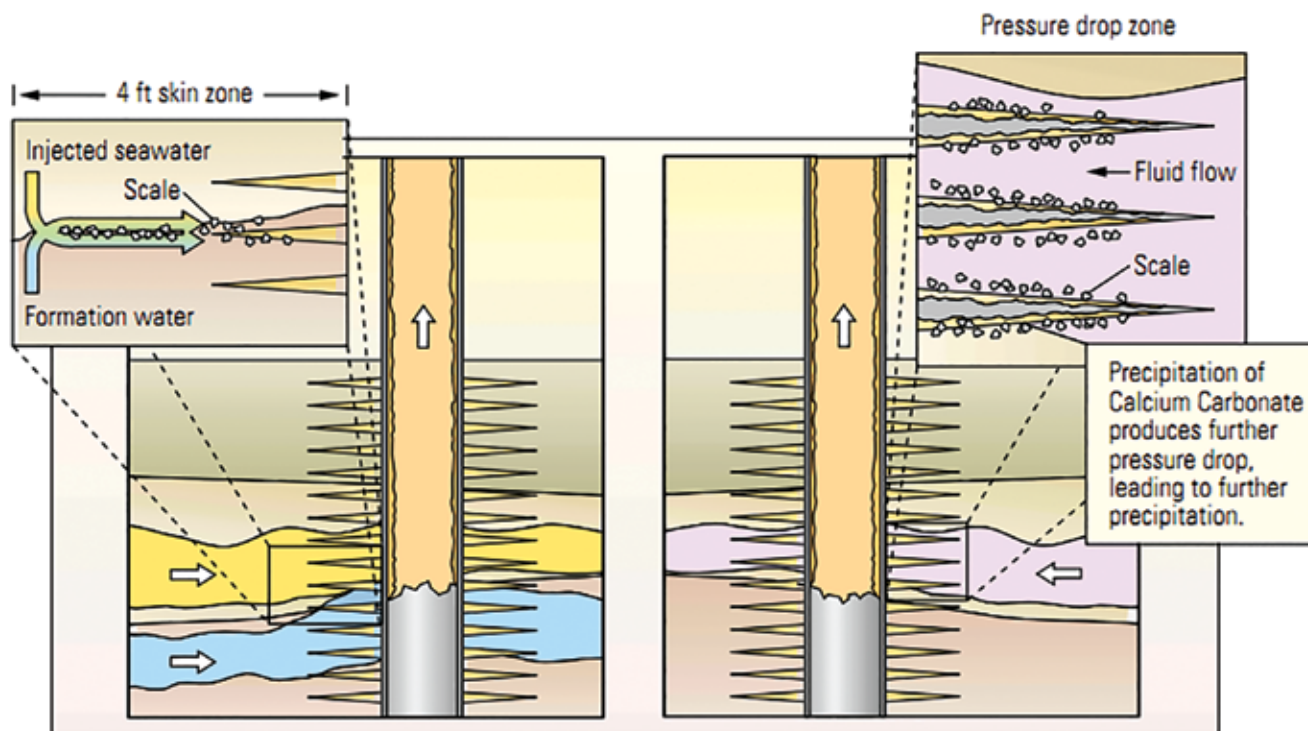


Figure 1. Two basic mechanisms of scales formed in the petroleum reservoir [1].

Table 1. The location and composition of the scale deposit

Location	Observation	Main source	Major component
Tubing and surface equipment	Scale occurs as a thick layer adhering to the inside of the tubing, valve and surface equipment	- Change of temperature and pressure. - Fine scale from downhole is lifted up surface and adhering to the inside of tubing.	Dependence of water composition, however scale often includes CaCO ₃ , FeS, asphaltene
Downhole and near wellbore area	Finer particle size than tubing scale, blocking gravel pack as well as matrix pores	- Pressure drop; - CO ₂ leaving; - Incompatible water mixing.	Mainly CaCO ₃ and CaSO ₄ , sometimes BaSO ₄ and SrSO ₄

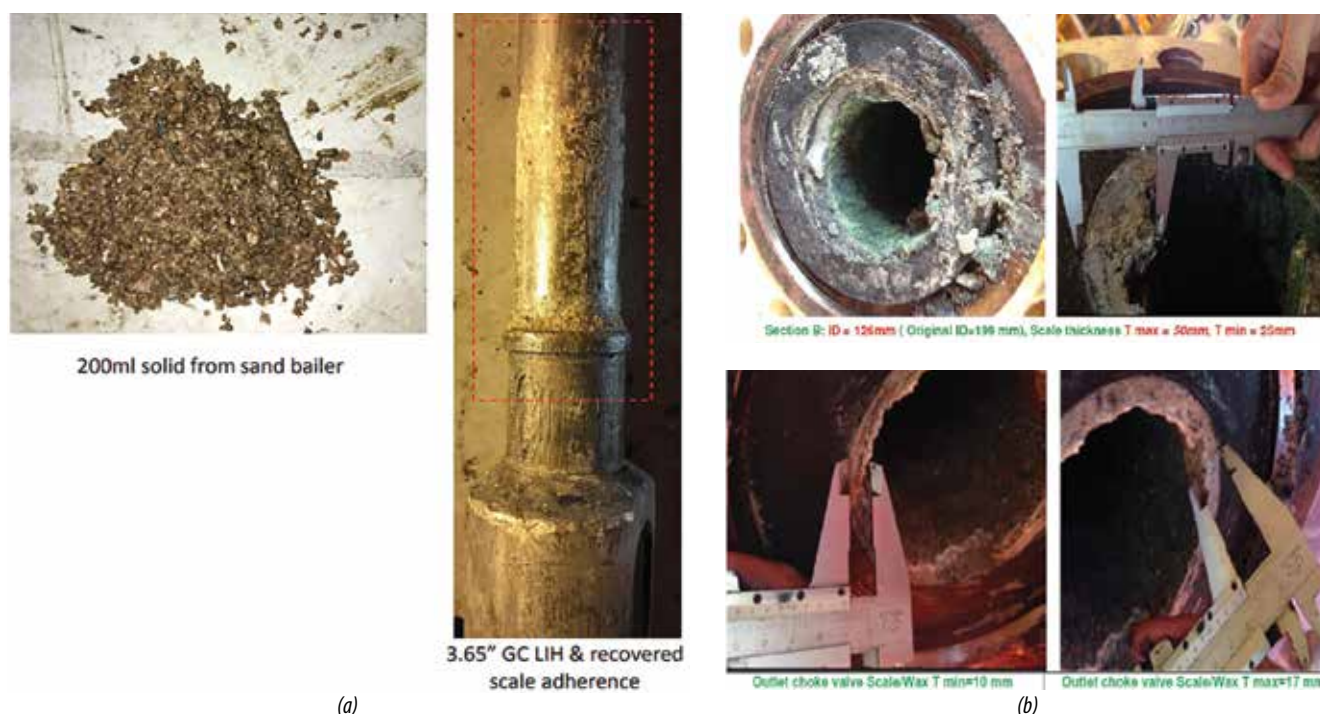


Figure 2. Inorganic scale formed in the production system, Vietnam's oil field (a: at tubular; b: at choke valve).

incompatible water, many produced waters that have become oversaturated and scale-prone do not always produce scale. In order for a scale to form it must grow from solution. The first development within a saturated fluid is a formation of unstable clusters of atoms, a process called homogeneous nucleation. The atom clusters form small seed crystals triggered by local fluctuations in the equilibrium ion concentration in supersaturated solutions. The seed crystals subsequently grow by ions adsorbing onto imperfections on the crystal surfaces extending the crystal size. The energy for seed crystal growth is driven by a reduction in the surface free energy of the crystal, which decreases rapidly with increasing radius after a critical radius is exceeded. This implies that large crystals favour continuing crystal growth, and also implies that

small seed crystals may rediscover. Thus, given a large enough degree of supersaturation, the formation of any seed crystal will encourage an increase in the growth of scale deposits. The seed crystal, in effect, is a catalyst for scale formation. Crystal growth also tends to initiate on a pre-existing fluid-boundary surface, a process called heterogeneous nucleation. Heterogeneous nucleation sites include surface defects such as pipe surface roughness or perforations in production liners, or even joints and seams in tubing and pipelines. A high degree of turbulence can also catalyse scale deposition. Thus, the accumulation of scale can occur at the position of the bubble point pressure in the flowing system. This explains why scale deposits rapidly build on downhole completion equipment.

- Identifying scale

Identifying the location and composition of the scale deposit is the first step in designing a cost-effective remediation programme (Table 1).

3. Scale control method to reduce problem cost by scale formation

The direct cost of removing scale from one well can be as high as USD 2.5 million, and the cost of deferred production even higher [3]. Just as prevention is better than cure in medical practice, keeping producing wells healthy is ultimately the most efficient way to produce hydrocarbons. In most cases, scale control method starts with scale prediction (forecast) and needs to be updated regularly based upon surveillance. This method will balance preventive measures and remediation (removal method). From the results of prediction of scale, a suitable scale control strategy will be described including prevention and remediation methods.

- Prevention

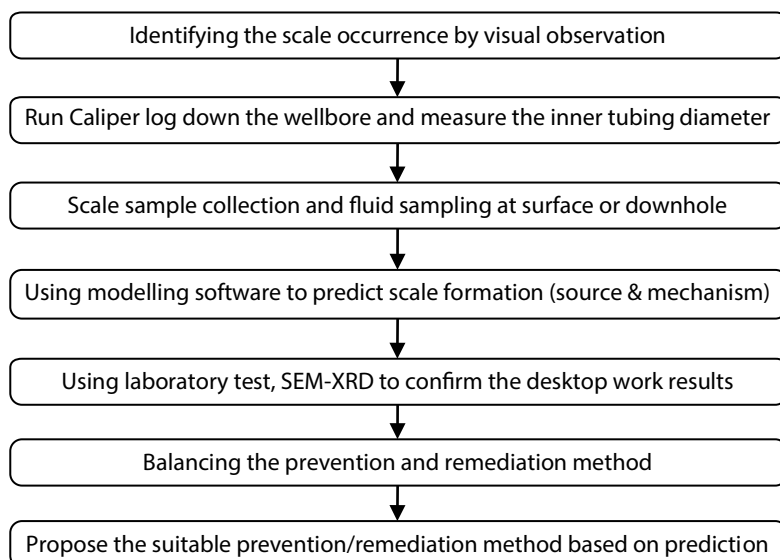
Choosing suitable chemical inhibition - continuous or periodic squeezes;

In most cases, scale prevention through chemical inhibition is the preferred method of maintaining well productivity. Inhibition technique can range from basic dilution method, to the most advanced and cost-effective method of threshold scale inhibitor.

- Remediation: Scale removal, either chemical or physical.

Scale removal techniques must be quick, non-damaging to the wellbore, tubing or formation environment, and effective at preventing reprecipitation. The best scale-removal technique depends on knowing the type and quantity of scale, and its physical composition or texture. A poor choice of removal method can actually promote the rapid recurrence of scale.

The following workflow is presented to summarise the scale control method:



4. Case study using scale prediction method done by VPI and Hoan Vu JOC

The A oil field has produced oil from fractured basement reservoir with 4 produced wells, in which 1P-SCL has the highest production rate. However, the well productivity index (PI) of 1P-SCL significantly dropped from 6.2 to 3.0bpd/psi after just 2 years of first oil during a short period (several weeks). The pressure survey is carried out in an yearly basis to determine reservoir pressure and well PI. The skin factor could not be estimated in the 1P-SCL well due to wellbore storage effects. It is essential to quantify and characterise the scale formation downhole in 1P-SCL, focusing on near-wellbore area where pressure drop takes place in flowing condition. Therefore, the best strategy in combating losses experienced due to scaling is periodical prevention of scale formation. VPI has conducted this study for Hoan Vu JOC to propose the suitable method with the scale problem of 1P-SCL in the A oil field.

All data relating to drilling, completion and operation phases of the 1P-SCL well were gathered and reviewed. Current production water of 1P-SCL was also sampled and analysed. To support for this study, many experimental tests and analyses were conducted including the filtration membrane tests, self-scaling tests and incompatible mixing test using HTHP (high temperature, high pressure) laboratory system. Additionally, a computational modelling has also been undertaken with the support from the latest version of ScaleChem software to evaluate the scale tendency and scale amount.

4.1. Production water composition

Initially, the reservoir pressure decreased continuously with very low water cut < 3%. The reservoir pressure decreased from around 7,200psia to 5,600psia after 5 years of operation. It means that there has been no aquifer support for the reservoir pressure. Besides, the composition of 1P-SCL water at the beginning was very

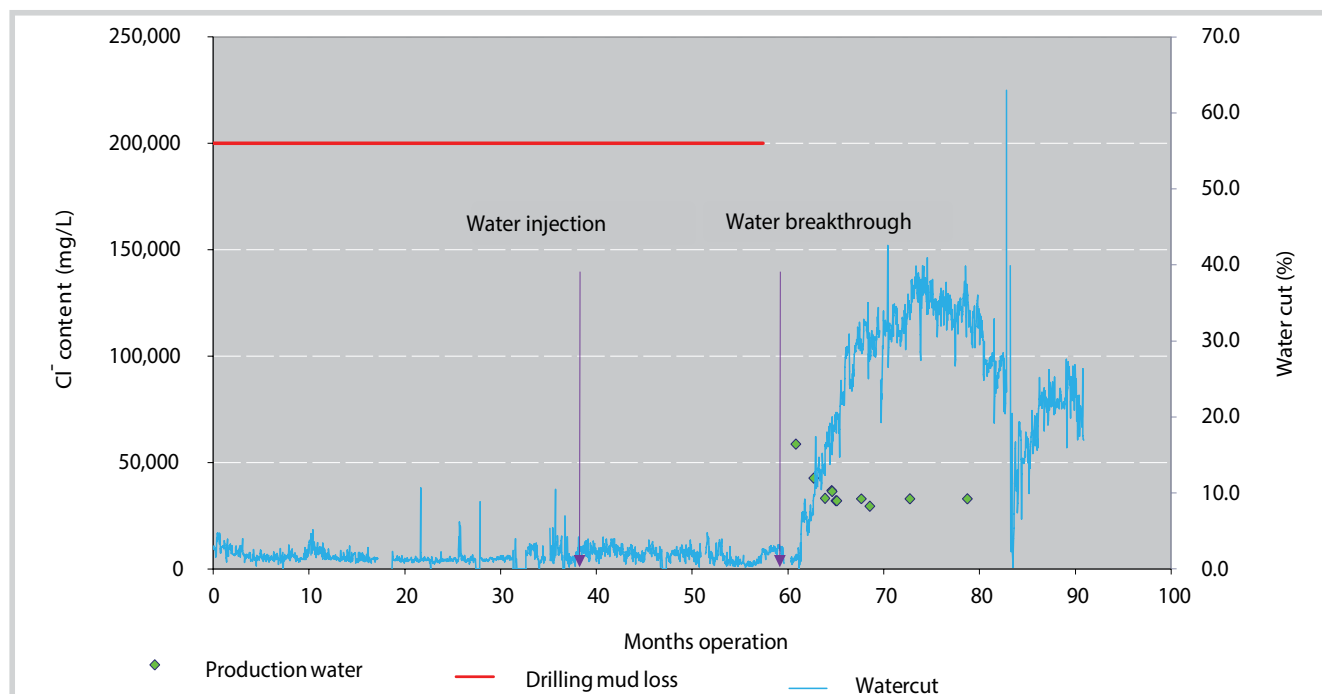


Figure 3. Cl⁻ content and water cut in historical production water composition of 1P-SCL well.

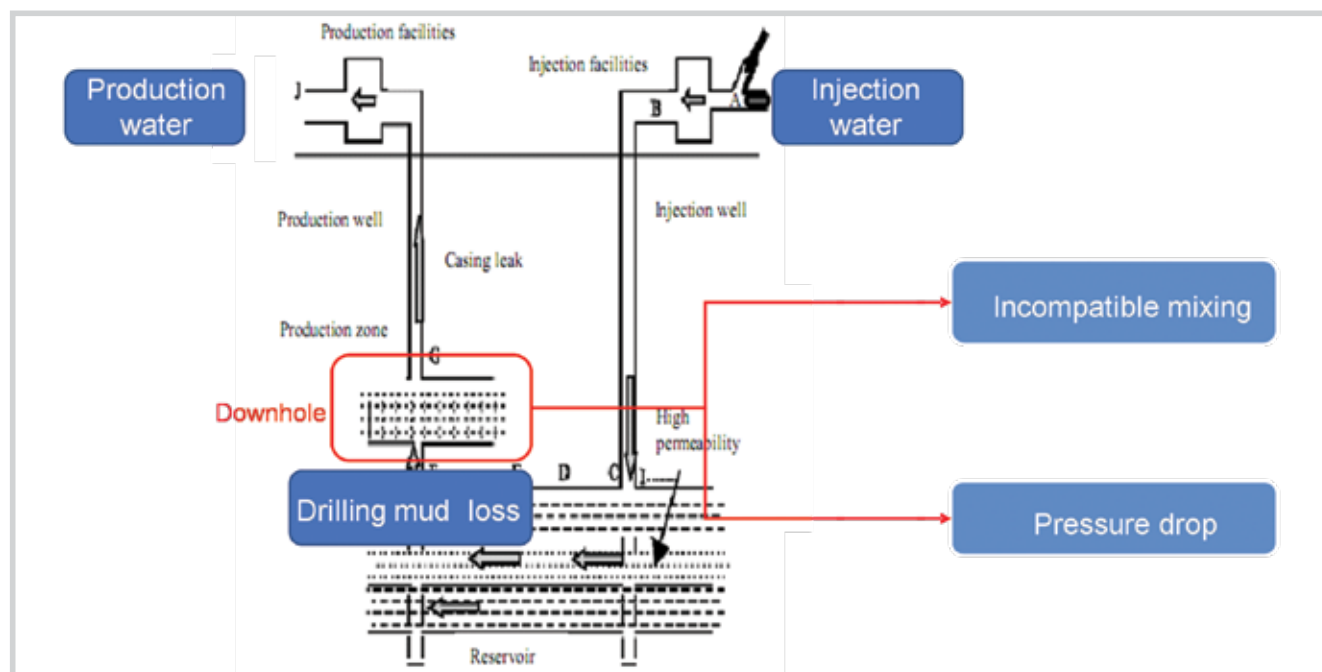


Figure 4. Scale scenario at downhole of 1P-SCL [6].

rich in Cl⁻, then the Cl⁻ content decreased right after the water breakthrough. The 1P-SCL has its production target at basement reservoir (more than 4,000mD), therefore, during the drilling phase, a very high density drilling mud was used. This drilling mud was CaCl₂ with very high content of Cl⁻ (200,000mg/L). Generally, in the basement of the referent oil field in the South East offshore Vietnam, the connate formation water (if available) may be immigrated from above reservoir (Oligocene) with low

total dissolved solid (TDS) value (< 40,000mg/L). However, the TDS value of 1P-SCL production water is quite high (> 90,000mg/L). Hence, the production water of 1P-SCL can be considered as drilling mud losses only (at the initial time of production) and the mixture of drilling mud losses with injection water at a later phase.

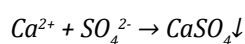
After water breakthrough occurred the water rate and cut increased within a few months to approximately 1,500 barrels/day and 38% respectively. Seawater breakthrough,

from injection well to 1P-SCL was marked also by a rapid decline in Cl⁻ in production water (Figure 3) and approximately coincided with the start of water production in this well suggesting that breakthrough occurred within the oil-leg (Cl⁻ is used as a conservative natural tracer [4]). Before water breakthrough, around 105,000 barrels of drilling losses (brine) were recovered. The remaining approximate 25,000 barrels of brine could be mixed with injection water during several months leading to the decrease of Cl⁻ content in production water. The Cl⁻ content sharply decreased and then kept stably at around 30,000mg/L during 15 months. By calculation, the mixing ratio at this period is about 95% of injection water. This ratio is acceptable if compared to the remaining drilling mud loss out of total production water.

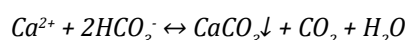
4.2. Scale scenarios at 1P-SCL well

By analysis of the water composition of production water and the drilling mud loss, the scale may form at downhole of 1P-SCL according to 2 scenarios:

- The incompatible mixing between injection water and drilling mud loss at the time of water breakthrough. The contact of seawater rich in SO₄²⁻ with drilling mud loss (CaCl₂) will form CaSO₄, an inorganic salt with very low solubility at high pressure and high temperature [5]:



- The change of pressure from reservoir to downhole. As these fluids will experience drop in pressure, CO₂ leaving leading the formation of CaCO₃:



4.3. Prediction of scale tendency at downhole of 1P-SCL by ScaleChem software

Desktop scale study is simulated and predicted the scaling tendency and severity for oil production system including auto-scaling at subsurface and surface facilities and incompatible mixing between different sources of water by ScaleChem software. The

results of the scaling prediction are frequently used to determine whether scaling is likely to occur and the scale species likely to be formed at subsurface/surface condition.

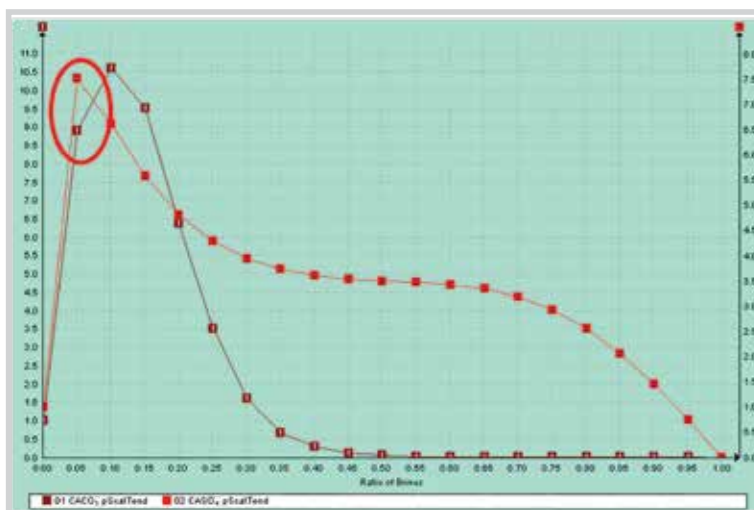


Figure 5. Scale tendency at the different mixing ratio at downhole of 1P-SCL.

Table 2. Scale amount formed at downhole of 1P-SCL by ScaleChem

	CaSO ₄ (mg/L)	CaCO ₃ (mg/L)	Total (mg/L)
Incompatible mixing	2,293	48	2,341
Pressure drop	0	32	32
			2,373



Figure 6. High pressure, high temperature laboratory system.

Table 3. Composition of injection water and drilling mud loss for the test

Composition	mg/L	Composition	mg/L
Injection water			
Na ⁺	11,068	Cl ⁻	19,564
K ⁺	407	SO ₄ ²⁻	2,418
Mg ²⁺	1,138	HCO ₃ ⁻	138
Ca ²⁺	414	pH	7.72
Drilling mud loss			
Ca ²⁺	115,800	Cl ⁻	205,000

Table 4. Dynamic data of 1P-SCL for the test

Location	Temperature (°C)	Pressure (psi)
Reservoir	150	5,350
Downhole	140	4,000

as input data of ScaleChem software. The results of incompatible mixing are given at Figure 5. Thereby, at mixing ratio of 95% injection water, two inorganic materials were found as CaCO₃ (calcite) and CaSO₄ (anhydrite). When the fluid comes out to downhole of 1P-SCL, the pressure drop leads to the formation of CaCO₃ scale. The detail calculation of scale amount was summarised in Table 2.

4.4. Laboratory tests to simulate the formation of scale at downhole

Scale prediction tests were conducted to confirm the results of the computer scale predictions and capture the types of scale precipitation at downhole of 1P-SCL due to mixing incompatibility or change of pressure/temperature condition. Using the high pressure, high temperature laboratory system to assess the scaling risk associated with several of pressure at different temperatures of oil process system and interaction between water sources.

The mixing ratio between 2 sources is 95-5 as calculation above. The solid scale obtained in the tests on the membrane will be analysed by SEM-EDS and XRD to determine the type of scale. The amount of scale is also determined.

- Laboratory test results:

The SEM image shows clearly that there are two types of crystal formed in the test, one of needle-shaped crystal and the other of powder shaped and smaller.

EDS results (element composition analysis) on the needle-shaped crystal show the elements of calcium, sulphur and oxygen account for CaSO₄ and on the powder-shaped crystal show the elements of calcium, carbon and oxygen account for CaCO₃.

Element	(keV)	Mass (%)
O	0.525	13.47
S	2.307	43.21
Ca	3.690	43.32
Total		100.00

Element	(keV)	Mass (%)
C	0.277	14.65
O	0.525	19.92
Ca	3.690	65.43
Total		100.00

The XRD results also illustrate two types of peak of two crystals: anhydrite (CaSO₄) and calcite (CaCO₃) with weight fraction of 96% and 4% accordingly.

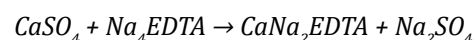
4.5. Evaluation and recommendation

The desktop work results show abundance of CaSO₄ scale with some CaCO₃ that can be formed by the incompatible mixing between injection water and drilling mud brine and by the pressure

drop. As per the computational modelling results, the worst case predicts a total amount of scale precipitation of approximately 2,373mg/L in near well-bore/downhole area. Using the laboratory test, a solid amount of around 2,089mg/L was collected in the test conducted under near-wellbore/downhole condition. Hence, both results of laboratory and modelling are in the same range.

Through reviewing the data and evaluating the laboratory test results as well as software modelling results, the major cause of PI drop of the 1P-SCL well is recognised. The results show that the incompatibility between calcium-based brine drilling mud fluid and injection water containing high sulfate causes scale precipitation. However, at the moment of water sampling, the existence of drilling mud in the production fluid is almost negligible, therefore this decrease of PI caused by CaSO₄ scale will not continue.

To restore the PI, the chelating-based chemical (such as EDTA) should be applied for the downhole of 1P-SCL well. The following reactions illustrate the mechanism of dissolver performance [3]:



Generally, once the scale is dissolved through chelation, there is no re-precipitation. Stable at temperatures up to 250°C, the chelating agent is a low toxicity scale dissolver that is effectively noncorrosive on most steels - making the treatment extremely safe.

5. Conclusions

- Scale monitoring plan and prediction of the scale formation should be carried out frequently to minimise the bad effect of inorganic scale to oil production.
- The incompatibility between injection water (seawater) and formation water or drilling mud brine needs to be studied prior to water injection or EOR application.
- The selection of scale prevention and remedial method must be based on the mechanism and source of scale formation.

- High density calcium-based brine during drilling and completion phase should be used with special caution to minimise the incompatibility with injection water containing high sulfate content.

References

1. Mike Crabtree, David Eslinger, Phil Fletcher, Ashley Johnson, George King. *Fighting scale: Removal and prevention*. The BP Technology Magazine. 1998.

2. Guihong Pei, Chunyang Wang, Lili Liu. *Experimental study on the cause of inorganic scale formation in the water injection pipeline of Tarim oilfield*. Journal of Chemistry. 2014.

3. J.Moghadasi, H.Müller-Steinhagen, M.Jamialahmadi, A.Sharif. *Scale deposition in porous media and their removal by EDTA injection*. Engineering Conferences International Symposium Series: Proceedings of 7th International Conference on Heat Exchanger Fouling and Cleaning - Challenges and Opportunities, Tomar, Portugal. 1 - 6 July, 2007.

4. Francisco J.Alcalá, Emilio Custodio. *Using the Cl/Br ratio as a tracer to identify the origin of salinity in aquifers in Spain and Portugal*. Journal of Hydrology. 2008; 359(1 - 2): p. 189 - 207.

5. Amer Badr Bin Merdhah, Abu Azam Mohd Yassin. *Study of scale formation in oil reservoir during water injection - A review*. Marine Science & Technology Seminar, Kuala Lumpur, Malaysia. 22 - 23 February, 2007.

6. Amer Badr Bin Merdhah, Abu Azam Mohd Yassin. *Scale formation in oil reservoir during water injection at high-salinity formation water*. Journal of Applied Sciences. 2007; 7(21): p. 3198 - 3207.

7. M.Amiri, J.Moghadasi. *Prediction the amount of barium sulfate scale formation in Siri oilfield using OLI ScaleChem software*. Asian Journal of Scientific Research. 2010; 3(4): p. 230 - 239.

Maximising production in shale reservoirs

Hon Chung Lau

National University of Singapore

Email: ceelhc@nus.edu.sg

Summary

This paper describes the interaction between hydraulic fractures and the multi-porosity system of shale reservoirs. During the process of hydraulic fracturing, a complex fracture network consisting of primary and secondary fractures is created. It is postulated that only shale porosities that are in contact with these hydraulic fractures will contribute to hydrocarbon production. Furthermore, we propose a way to maximise well productivity by injecting micro-sized proppants into the secondary hydraulic fractures and reactivated natural fractures to prevent them from closing during production and thereby extending the fracture network. Both laboratory experiments and field tests have shown encouraging results of using micro-sized proppants to enhance the productivity of Barnett shale. More research is warranted to study the applicability and optimisation of micro-sized proppants in production enhancement in other shale formations.

Key words: Shale reservoir, micro-sized proppant, maximizing production, natural fracture, hydraulic fracture.

1. Introduction

The shale revolution in North America in the last decade has captured the attention of both researchers and practitioners in the oil and gas industry. The current research & development effort focuses on the optimisation of multi-stage hydraulic fracturing in long horizontal wells in shale reservoirs. However, a fundamental understanding of the interaction between hydraulic fractures, natural fractures and the pore system of the shale reservoir is lacking. The objective of this paper is to fill this knowledge gap. Based on this understanding, we propose a way to maximise productivity of shale reservoirs by increasing the connectivity between the hydraulic fractures and the pore system of the reservoir.

2. Pore system in shale reservoirs

The pore structure of a shale reservoir is more complicated than that of a conventional reservoir because shale contains both organic matter and inorganic matter. The former consists of kerogen and the latter carbonate, quartz, feldspar and clays. The various types of natural porosities of a shale formation can be classified as Figure 1.

- Organic pores

Organic matter such as kerogen tends to develop intraparticle pores during the evolution and expulsion of

hydrocarbons from the kerogen [1]. These intraparticle pores have been observed in all mudstones, and believed to contribute dominantly to the total porosity. Their shapes can be semispherical, bubble-like, or pendular. Organic porosity can also be enhanced by cracks or fractures within the organic matter.

- Inorganic pores

Inorganic pores are those that exist in inorganic minerals such as clays, quartz and feldspar. Microscopic observations show that they exist as partially open floccules, triangular pores at clay platelet junctions or lenticular, slit-like pores between clay flakes. These inorganic pores may reduce in size during hydrocarbon production due to compression of the slit-like pore structures because of the increase in effective vertical stress [1].

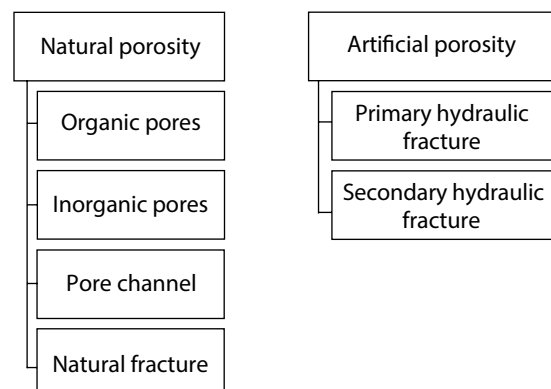


Figure 1. Porosity system in shale reservoirs.

- Pore channels

Pore channels are interparticle pores. They form connections among organic pores, inorganic pores, and between them. They exist in inorganic matter as triangular, slit-shaped pores or vuggy pores [1].

- Natural fractures

Thermally mature shales usually contain vertical, sub vertical and in some cases horizontal natural fractures. These fractures are usually filled with mineral precipitates, such as calcite, dolomite, pyrite, barite and clays. In some cases, non-mineralised natural fractures may contribute to substantial gas storage capacity as observed in the Bakken shale [1].

3. Gas storage in shale reservoirs

Natural gas can be stored in any of the aforementioned natural porosities of a shale reservoir. It can exist as free gas in the pore space, absorbed gas on the surfaces of the organic and inorganic pores and on the wall of the natural fractures. Furthermore, it can be stored as dissolved gas in the kerogen. During production from shale reservoirs, free gas is produced first. The initial production and subsequent rapid decline in gas rate are both due to free gas production. This decline rate is hyperbolic. Only later is the absorbed gas produced and the decline rate is exponential [2]. Gas absorbed on the surface of the pore system can be 6 - 8 times the amount of free gas [3]. Due to its slow diffusion rate from the kerogen to the pore system, dissolved gas contributes insignificantly to hydrocarbon production.

The relative amount of gas stored in the organic pores, inorganic pores, pore channels and natural fractures varies from shale to shale. Usually natural fractures do not exhibit significant gas storage capacity, most often at best 0.5% [3]. However, in the highly fractured Bakken shale, a significant amount of gas comes from the non-mineralised natural fractures [1].

4. Permeability in shale reservoirs

Permeability is due to both pore size and interconnectivity between pores. The pore size in shale reservoirs is very small. Figure 2 shows the pore size distribution in various North American shales [4]. It ranges from less than 1 to 200nm. An examination of pore size distribution of global unconventional shale reservoirs by Zou also concludes that it varies from about 5 - 200nm [5]. A study by Nelson concludes that the pore-throat

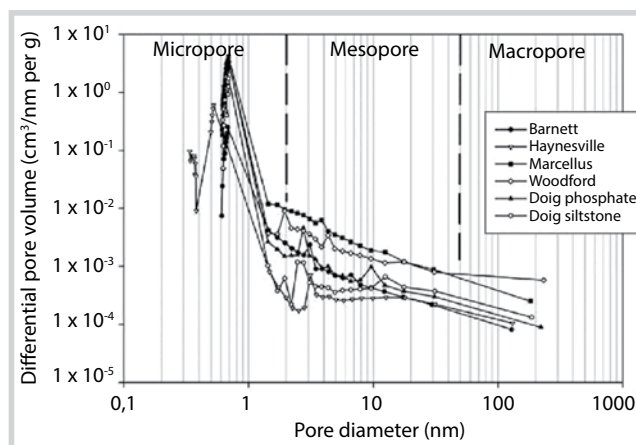


Figure 2. Pore size distribution of North American shales [4].

size distribution in shale reservoirs ranges from several to hundreds of nm [6]. In addition, the pores within a shale reservoir are usually poorly connected. Both the small pore size and the poor connectivity between pores lead to the extremely low permeability of shale reservoirs (< 0.001 - 0.01 mD).

5. Gas transport in shale reservoirs

Gas transport in a shale reservoir is different from that in a conventional reservoir due to the very small pores. As the pore size shrinks, the mean free path of gas molecule is comparable to that of a pore or pore channel. Under this condition, Darcy's law does not apply. Other flow mechanisms such as slip flow, surface diffusion, Knudsen diffusion, Langmuir desorption, and molecular diffusion come into play. These flow mechanisms are usually much slower than Darcy's flow. Hence, in the absence of reservoir stimulation by hydraulic fracturing, there is practically no production from shale reservoirs.

6. Interaction between horizontal well, hydraulic fractures and shale porosities

In conventional reservoirs, a horizontal well usually has a production rate several times that of a vertical well due to larger contact area between the well and the reservoir. However, in a shale reservoir, a horizontal well by itself does not lead to increase in hydrocarbon production due to the very low reservoir permeability. The function of a horizontal well, however, is to allow multiple hydraulic fractures to be placed along its length. It is the hydraulic fractures that create the connection between the well and the reservoir thus allowing flow of gas into the well. Each stage of hydraulic fracture increases the contact between the well and the reservoir. Therefore, when a horizontal well consists of multi-stage hydraulic

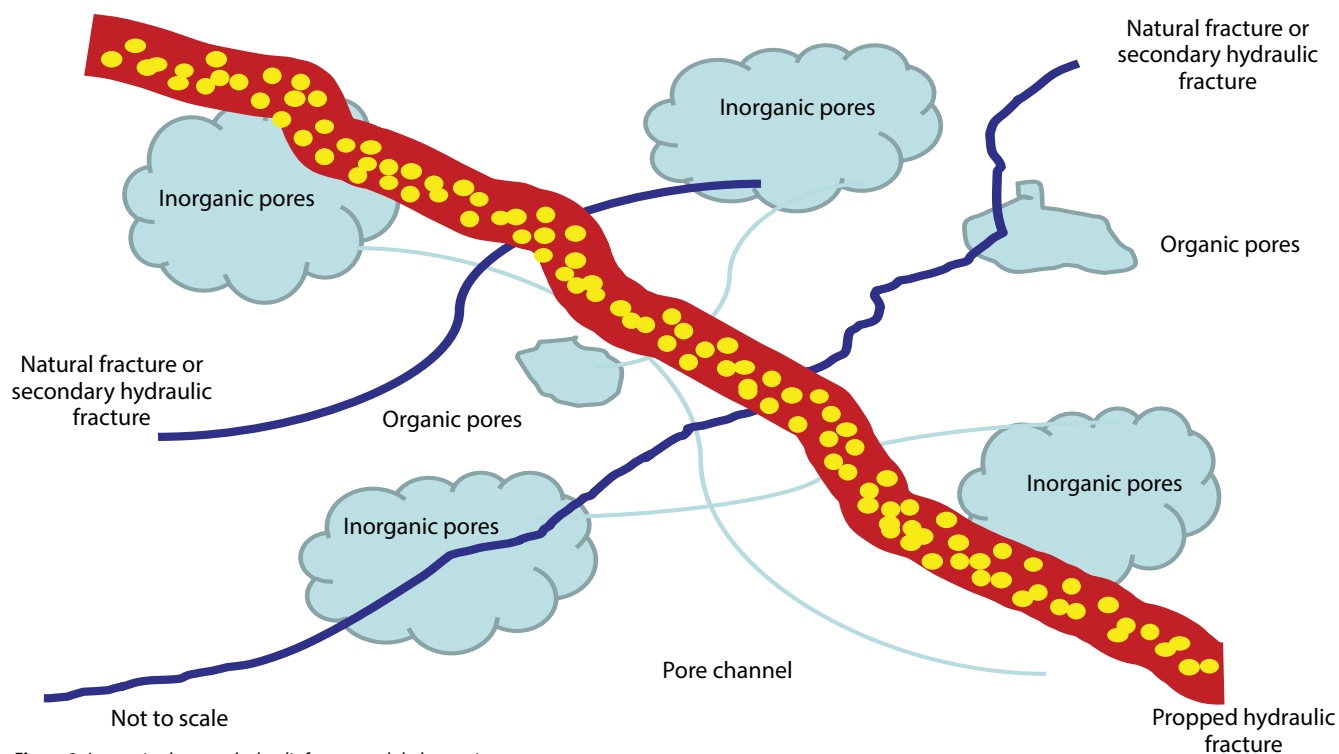


Figure 3. Interaction between hydraulic fracture and shale porosity system.

fractures, the contact between the reservoir and the well is multiplied many times, thus leading to significant hydrocarbon production. However, only the porosity connected to the hydraulic fractures contributes to flow. Porosities that are not connected to the hydraulic fractures do not contribute to flow due to the very low reservoir permeability. This is the major difference between a conventional and unconventional reservoir. In a conventional reservoir, hydrocarbon flows from the reservoir to the hydraulic fracture by Darcy's flow. In an unconventional reservoir, the flow of hydrocarbon to the hydraulic fracture is too slow to be effective. Therefore, only the porosity that is contacted to the hydraulic fractures will contribute to production. Figure 3 depicts the interaction between the hydraulic fracture and the shale porosity system.

7. Maximising interaction between hydraulic fractures and shale porosities

One way to maximise the production of a shale reservoir is to increase the interconnectivity between the hydraulic fractures and the natural porosities of the reservoir. This can be done by reactivating and propping the natural fractures and the secondary hydraulic fractures.

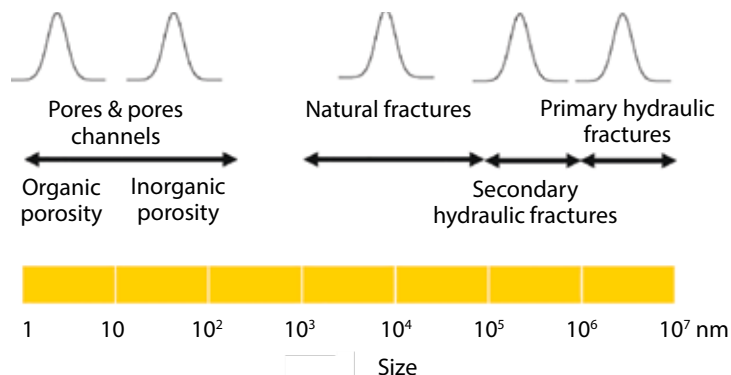


Figure 4. Relative size of porosities in shale reservoirs.

- Connection between natural and hydraulic fractures

Field data suggest that some natural fractures are reactivated during the pumping stage of the hydraulic fracturing [7]. However, conventional proppants are too large (hundreds of microns) to enter the reactivated natural fractures (1 - 100µm). Consequently, when pumping stops, the natural fractures close and do not form conductive flow channels. In some cases, there may be some residual conductivity due to incomplete closing of the natural fractures.

- Connection between shale porosity system and hydraulic fractures

A hydraulic fracture extends from the wellbore to the shale reservoir when the injection pressure exceeds the fracture pressure of the shale. In conventional reservoirs, the fracture

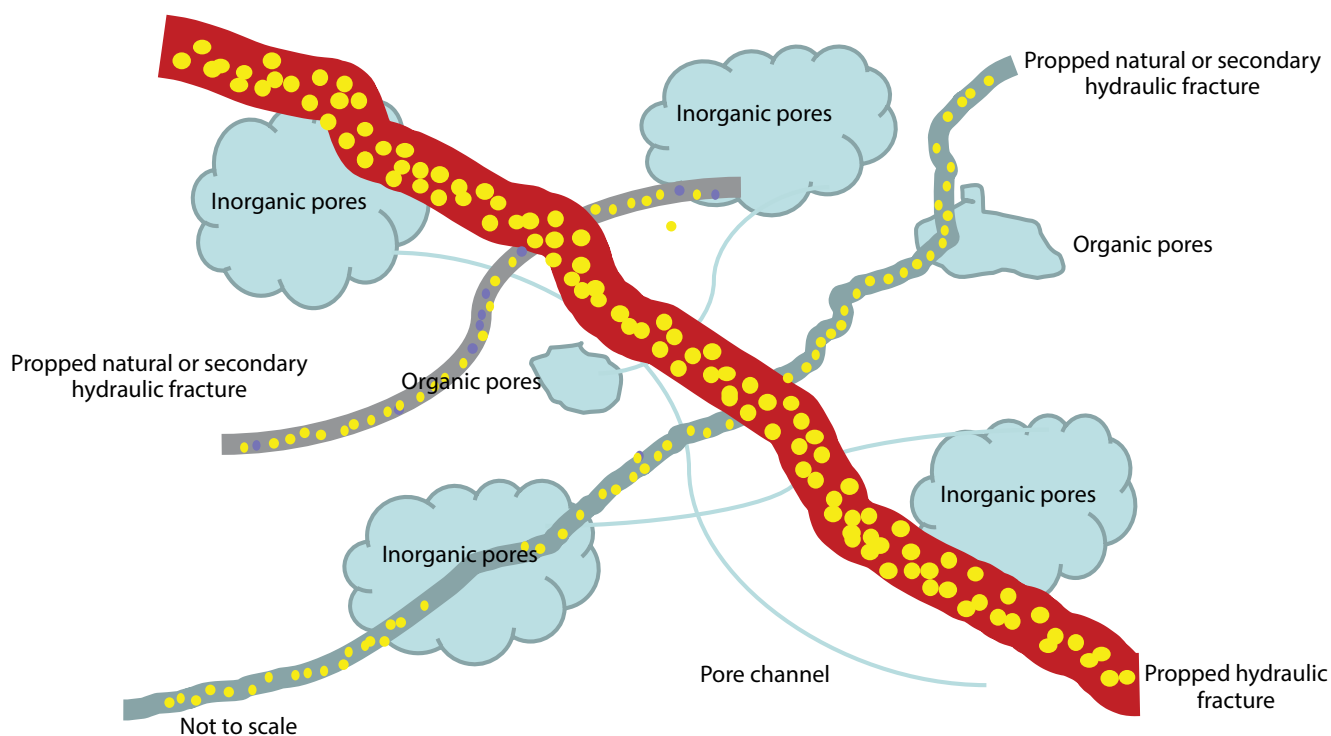


Figure 5. Increasing connectivity between hydraulic fractures and natural porosities by micro-sized proppants.

geometry is relatively simple and may be described as a planar fracture with well-defined fracture half length and fracture width. However, in very low permeability shale reservoirs, the fracture geometry becomes complex. Microseismic data suggest that the fractures are no longer planar, but have a rather complicated geometry [8] and resemble a network of complex fractures [9]. At present, microseismic is the tool most often used to map the fracture geometry. However, microseismic only measures locations in the reservoir where a shear failure occurs. It does not tell us whether these locations contribute to flow during production. Various authors have proposed different geometries of hydraulic fracture. However, the exact geometry of the hydraulic fracture is unknown to a large extent.

We postulate that the hydraulic fracture network has the following characteristics: (1) larger width, primary fractures extending from the horizontal well into the shale reservoir, (2) smaller width, secondary fractures extending from the primary fractures to other parts of the reservoir, and (3) connection between primary and secondary hydraulic fractures with natural fractures forming an extensive fracture network (Figure 3).

Figure 4 compares the relative size of porosities in a shale reservoir. Size of pores and pore channels ranges from 1 - 200nm. Natural fractures have an aperture

between 1 - 100 microns. Primary hydraulic fractures have a width between 1 - 10mm, whereas secondary hydraulic fractures have a width between that of natural fractures and primary hydraulic fractures.

Conventional fracture designs assume a relatively simple planar fracture geometry and the treatment volume and flow rate are designed to create a fracture of pre-determined half length and fracture width. Furthermore, the fracture is propped with high-permeability proppant to resist crushing during production. Thus the fracture forms a highly conductive pathway for transport of hydrocarbon.

When applied to shale reservoirs, this type of design is inadequate because it assumes a single fracture width and uses a proppant size which is too big to enter into the secondary fractures or reactivated natural fractures. Since the secondary fractures and natural fractures are not propped, they contribute little to flow.

Our proposal is to inject micro-sized proppants small enough to enter the secondary and reactivated natural fractures. These propped fractures will greatly enlarge the fracture network and the stimulated reservoir volume (Figure 5).

8. Micro-sized proppants

In order to enter the reactivated natural fractures and secondary hydraulic fracture, micro-sized proppants

should have diameter of 1 - 100 microns, i.e. 70 mesh or higher. Currently, proppants of this size range are not readily available.

- Laboratory study

So far, one operator and a service company have conducted a study on the use of micro-sized proppants for enhancing well production in Barnett shale [10, 11]. The micro-sized proppant used was a ceramic material having an average diameter of 30 μ m. Experiments were done with outcrop samples. Results show that the micro-sized proppant can increase the effective permeability of a micro fracture by as much as ten folds.

- Field pilot

A field pilot was conducted in eleven condensate rich gas wells in the Barnett shale in Wise County, Texas [10, 11]. Results show that incorporation of micro-sized proppant in the pad ahead of main hydraulic fracture treatment has resulted in a significant increase in well productivity over a 400-day period. Wells with micro-sized proppant exhibited 36 - 55% improvement in gas production and 23 - 47% improvement in condensate production compared to those without the micro-sized proppant. However, Barnett shale is known to have well developed natural fractures, although most of them are sealed except the largest ones [7].

- Future research

Reported results on the use of micro-sized proppants to increase the effectiveness of hydraulic fracturing on Barnett shale have been encouraging. Future research should focus on other shale reservoirs with a less developed natural fracture network. It is also worthwhile to test the relative importance of propping the natural fractures versus secondary hydraulic fractures in various shale formations. Also, development of micro-sized proppants of various sizes, material and strength will be important for future application.

9. Conclusions

The following conclusions can be drawn from our study.

Shale reservoirs have a multi-porosity system consisting of organic pores, inorganic pores, pore channels and natural fractures. Due to the very small pore size (1 - 200nm), poor pore interconnectivity, and sealed natural fractures, shale reservoirs have very low permeability (< 0.001 - 0.01mD).

In shale reservoirs, horizontal wells by themselves are incapable of inducing flow. Multi-stage hydraulic fractures are needed to connect the horizontal wellbore to the shale porosity system. However, only those porosities which are connected to the hydraulic fractures will contribute to hydrocarbon production. Porosities not connected to the hydraulic fractures will not contribute to flow.

Hydraulic fractures in shale reservoirs consist of a complex network of fracture. We postulate that hydraulic fractures consist of primary and secondary fractures of different widths. Both types of fractures can connect with the natural fractures.

During hydraulic fracturing, some natural fractures are reactivated and are connected to the hydraulic fractures. However, since conventional proppants are too big to enter them and secondary hydraulic fractures, they close when pumping stops and do not contribute significantly to hydrocarbon production.

One way to maximise well productivity is to inject micro-sized proppants (1 - 100 microns) into the secondary hydraulic fractures and the reactivated natural fractures, thereby extending the fracture network. This will also increase the stimulated reservoir volume.

Recent laboratory results have shown that a micro-sized ceramic proppant is effective in enhancing the permeability of micro-fracture in Barnett shale. In addition, an eleven-well pilot test showed that incorporation of the micro-sized proppant in the pad of fracture treatment increased the productivity of these wells by up to 50%.

Future research is needed to study the use of micro-sized proppants for productivity enhancement in other shale formations. Research is needed to tailor the size, type and strength of micro-sized proppants for particular shale formations.

References

1. Brian J.Davis, Russell Maharidge, Joel Walls. *Chapter 10: Laboratory tests and considerations to complement the overall reservoir understanding*. In "Unconventional oil and gas resources exploitation and development". CRC Press.
2. Abdus Satter, Ghulam M.Iqbal. *Reservoir engineering: The fundamentals, simulation, and management of conventional and unconventional recoveries*. Elsevier. 2016.
3. Matt W.Bratovich, Frank Walles. *Formation evaluation and reservoir characterization of source rock*

reservoirs. In "Unconventional Oil and Gas Resources Exploitation and Development". CRC Press. 2016.

4. Gareth Chalmers, Ian M.Power, R.Marc Bustin. *Characterization of gas shale pore systems by porosimetry, pycnometry, surface area, and field emission scanning electron microscopy/transmission electron microscopy image analyses: Examples from the Barnett, Woodford, Haynesville, Marcellus, and Doig Units.* AAPG Bulletin. 2012; 96(6): p. 1099 - 1119.

5. Caineng Zou. *Unconventional petroleum geology.* Elsevier. 2017.

6. Philip H.Nelson. *Pore-throat sizes in sandstones, tight sandstones and shales.* American Association of Petroleum Geologists Bulletin. 2009; 93(3): p. 329 - 340.

7. Julia Fiona Wells Gale, Robert M.Reed, Jon Holder. *Natural fractures in the Barnett shale and their importance for hydraulic fracture treatments.* American Association of Petroleum Geologists Bulletin. 2007; 91(4): p. 603 - 622.

8. Koras Shah, Robert Frank Shelley, Deepak Gusain, Lyle V.Lehman, Amir Mohammadnejad, Matthew

T.Conway. *Development of a Brittle shale fracture network model.* SPE 163829. SPE Hydraulic Fracturing Technology Conference, Woodlands, Texas, USA. 4 - 6 February, 2013.

9. Martin Rylance, Tony Martin. *Flushing away the profit: The potential misapplication of unconventional fracturing technology on a global scale.* SPE 170773. SPE Annual Technical Conference and Exhibition, Amsterdam, the Netherlands. 27 - 29 October, 2014.

10. Jeff Dahl, Philip Nguyen, Ron Dusterhoft, James Calvin, Shameem Siddiqui. *Application of micro-proppant to enhance well production in unconventional reservoirs: Laboratory and field results.* SPE 174060. SPE Western Regional Meeting, Garden Grove, California, USA. 27 - 30 April, 2015.

11. Jeff Dahl, James Calvin, Shameem Siddiqui, Philip Nguyen, Ron Dusterhoft, Eric Holderby, Bill Johnson. *Application of micro-proppant in liquids-rich, unconventional reservoirs to improve well production: Laboratory results, field results, and numerical simulations.* SPE 177663. Abu Dhabi International Petroleum Exhibition and Conference, Abu Dhabi, UAE. 9 - 12 November, 2015.

Combining low frequency spectral decomposition and post-stack seismic inversion to identify Middle Miocene gas bearing sands at Hai Thach field

Dao Ngoc Huong¹, Nguyen Trung Hieu¹, Nguyen Tien Thinh¹, Phan Dang Thai Son²

¹Vietnam Petroleum Institute, ²Bien Dong POC

Email: huongdn@vpi.pvn.vn

Summary

Located in the Nam Con Son basin, offshore Vietnam, Middle Miocene gas bearing turbidite sands at Hai Thach field are very difficult to identify on conventional seismic data due to their complex architectures and geometries [1]. The purpose of this study is mapping this reservoir in terms of its geometry and distribution by applying an integration of rock physics analysis, seismic attributes and post-stack seismic inversion. In the study areas, the P-impedance of sand is the same values with shale and the presence of gas in sand causes a decrease of acoustic impedance, which can be used to differentiate gas saturated sandstone from water saturated sandstone and shale. Seismic attributes applied based on the rock physics analysis result can also be used to define gas sand distributions. Low-frequency amplitude anomalies from 17 - 19Hz, obtained from spectral decomposition, have a high gas content where penetrated by wells, whereas low gas saturation zones in the wells do not correlate with the observed high amplitudes. Moreover, the gas sand distribution was successfully identified in the extracted P-impedance slice along horizon from an inverted P-impedance volume. Thus, the combination of low frequency spectral decomposition and seismic inversion may be used to successfully map gas distribution. Proposed workflow for mapping sand and gas sand can be used for future drilling programmes.

Key words: Gas sand, P-impedance, post-stack seismic inversion, low frequency spectral decomposition.

1. Introduction

Hai Thach field is located in Blocks 05-2 and 05-3, Nam Con Son basin, offshore Vietnam (Figure 1). The major types of reservoirs identified in the Nam Con Son basin are pre-Cenozoic weathered fractured basement, Oligocene and Miocene clastics, and Miocene carbonates [2]. This paper focuses on the Middle Miocene turbidite sandstones which are complicated due to their complex architecture and geometry. The HT-3P and HT-2X wells at Hai Thach field encountered reservoir with vertical thickness of 45m and 32m, respectively. Results from core description indicate that those intervals are turbidites deposited in deep water with mainly clean sandstone and minor interbedded siltstone and mud stone. Intense post depositional faulting further complicated the reservoir distribution. Since using conventional seismic data to predict reservoir distribution is not reliable enough, a combination of spectral decomposition and post-

stack seismic inversion was utilised to investigate this reservoir in term of lithology and hydrocarbon distribution.

2. Methodologies

- Rock physics analysis

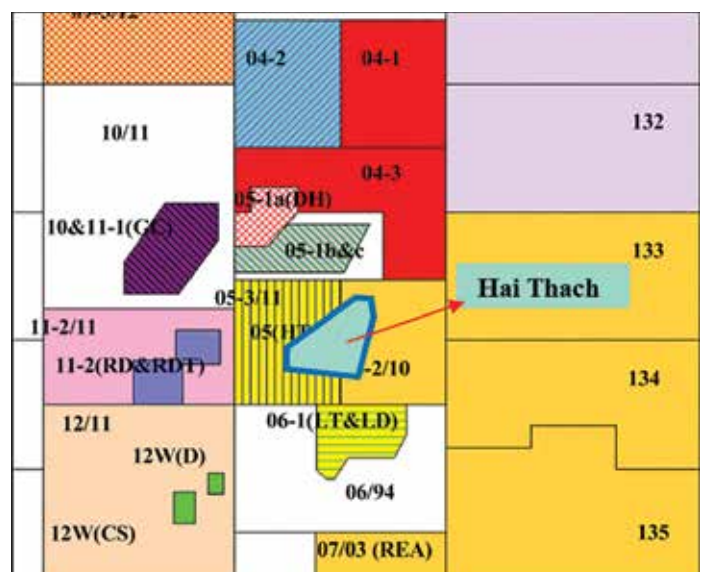


Figure 1. Location of the study area in offshore Vietnam.

Rock physics analysis aims to determine the rock properties based on logging curves. From these properties, gas bearing and water bearing sands, and bounding shale can be discriminated. Cross plots of acoustic impedance (product of density and compressional velocity) versus gamma ray (GR), clay volume (VCL) and water saturation (SW) are useful technique to differentiate in terms of lithology and fluids [3, 4].

- Spectral decomposition

Spectral decomposition is a mathematical tool for transforming seismic data from the time domain to frequency domain. In the low-frequency range, the abnormal amplitude associated with the presence of hydrocarbon, validated by well data, provides useful information for reservoir characterisation [5].

- Seismic post-stack inversion

Seismic inversion is a technique that has been used to transform seismic data into acoustic impedance, which is useful for predicting lithology and fluid distribution [6].

3. Results and interpretations

3.1. Rock physics analysis

The rock physics was analysed at wells

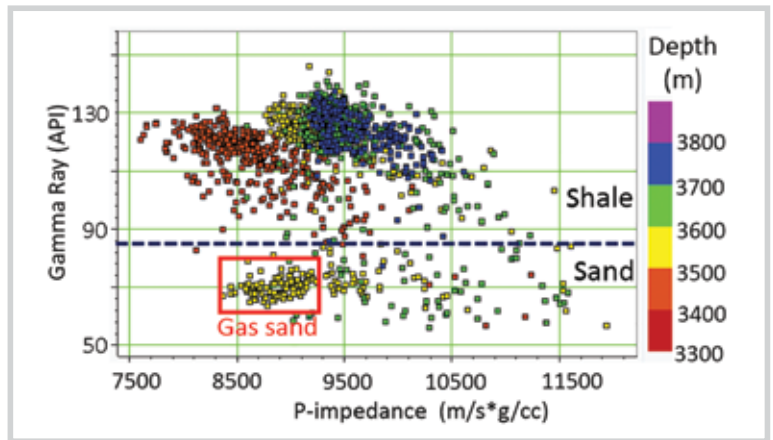


Figure 2. Cross plot of P-impedance and GR coloured by depth for well HT-3P showing the acoustic impedance overlapping when analysed in large depth intervals.

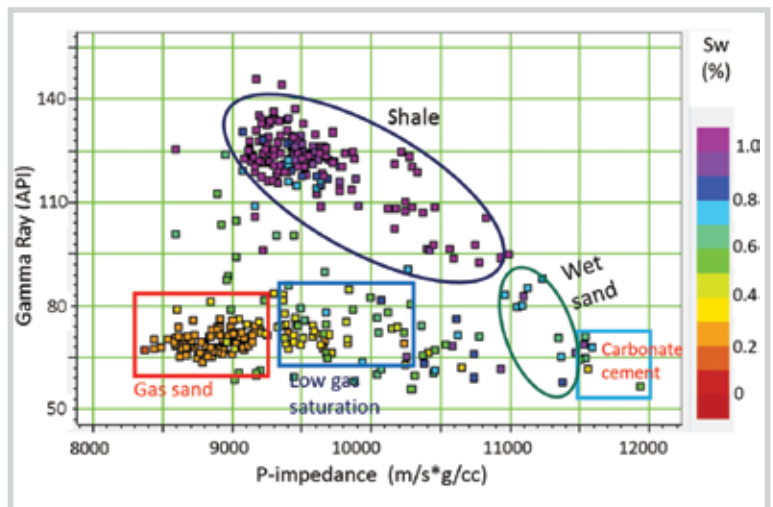


Figure 3. Cross plot of P-impedance and GR coloured by water saturation from a narrower depth interval of 3,550 - 3,650m in well HT-3P.

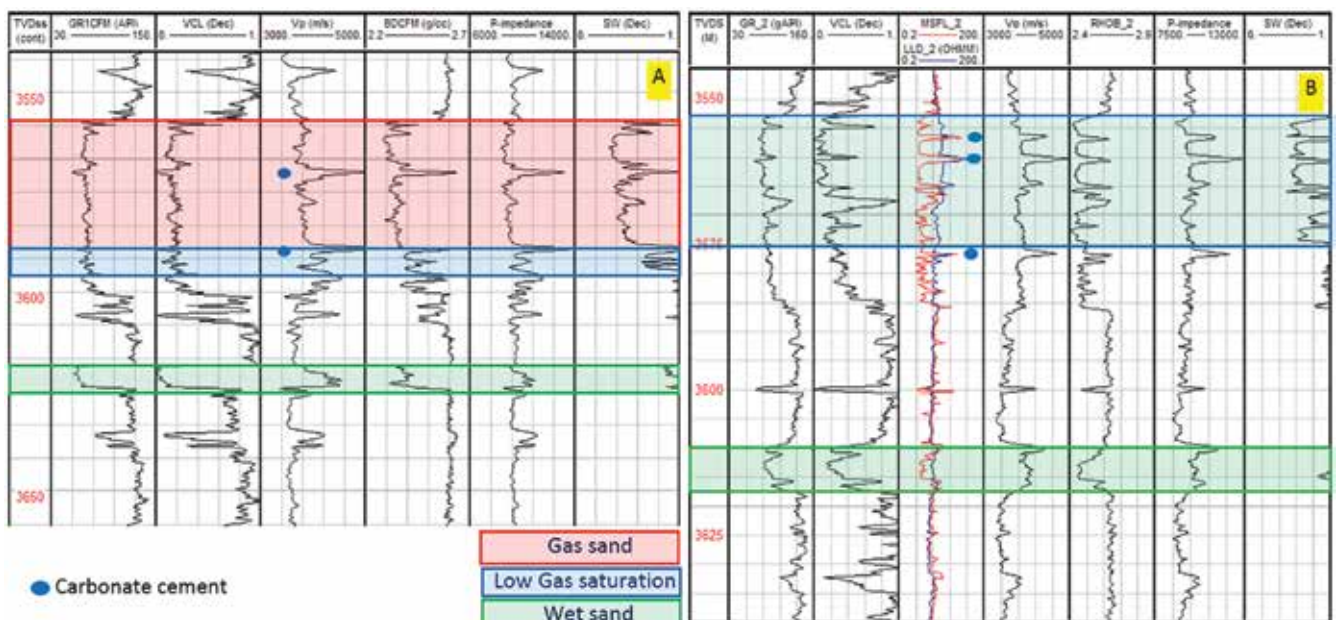


Figure 4. Well log data comprising gamma ray (GR), clay volume (VCL), P-wave (Vp), density, computed acoustic impedance and water saturation for depth interval 3,550 - 3,650m at well HT-3P (a) and well HT-2X (b).

HT-2X and HT-3P. The gas sand has been defined by using a clay volume; water saturation cut-off is about 40% and 60% respectively. The cross plot of the GR and P-impedance (computed from density and P-wave logs) from the zone of interest (3,300 - 3,800m) shows that the P-impedance of gas sand cannot be separated with

shale in terms of 500 thickness of sediment (Figure 2). In another test analysis of narrower interval which consists of reservoirs from 3,550 - 3,650m, a clear difference of P-impedance can be observed among gas sands, wet sands and shale (Figure 3). This shows that the presence of gas caused reduction of P-impedance in sand reservoir;

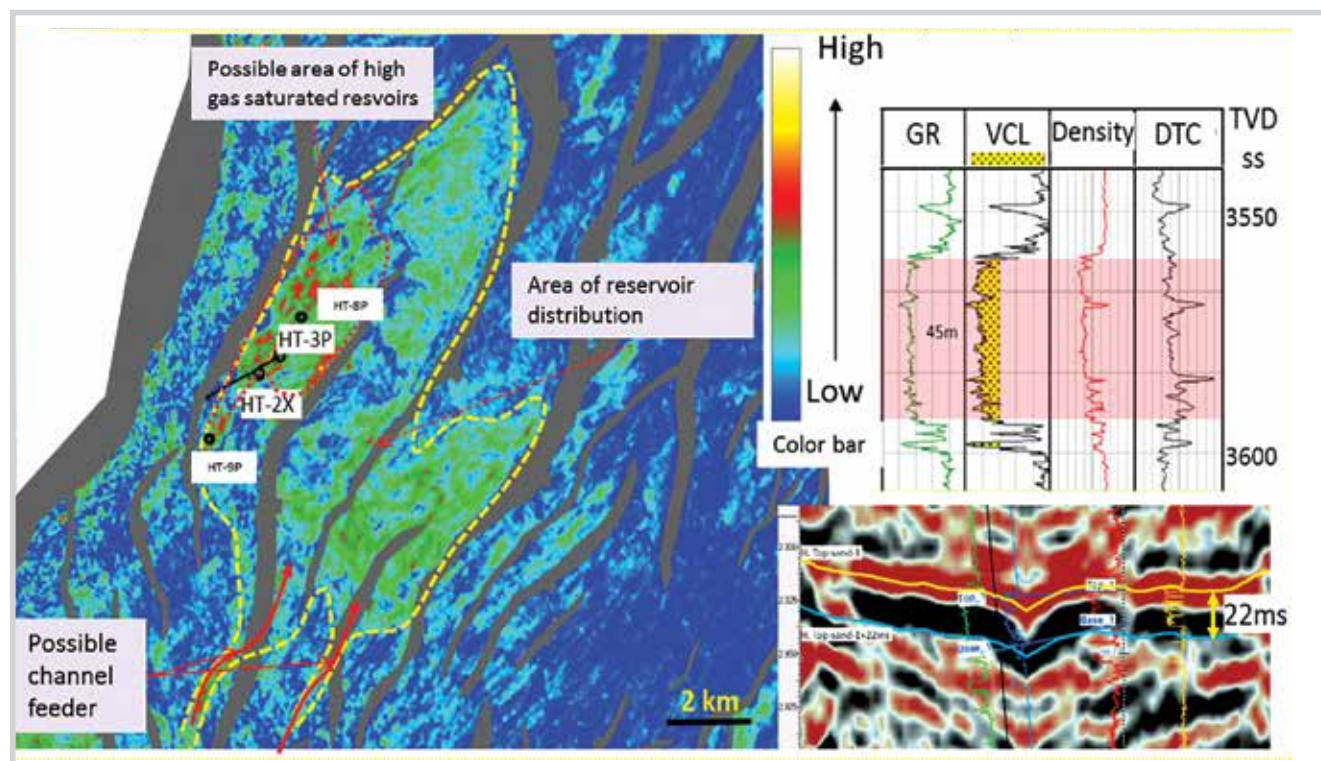


Figure 5. The RMS amplitude map of Horizon top-sand. The well logs show the RMS window range (red zone) covered in well HT-3P and the seismic section along well bores.

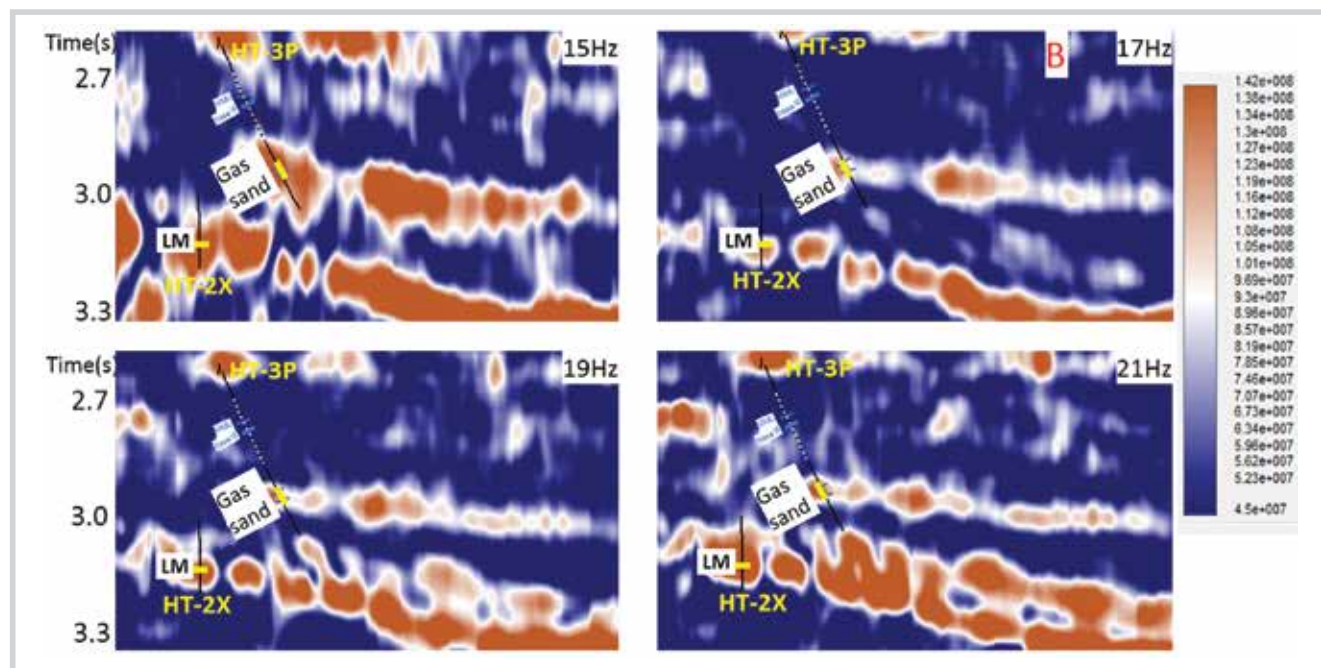


Figure 6. Spectral decomposition section with different frequency range.

therefore, using P-impedance in this interval is useful to determine high saturated gas sand [3].

A petrographic report for well HT-2X proved the existence of carbonate cement in core plugs at depths of 2,598m, 3,593m, and 3,605m, which is characterised by low GR, high density and high Vp (velocity) and density (Figure 4).

3.2. Sand body prediction

Delineating sand body distribution is the first step to investigate this reservoir. An extraction of amplitude from conventional seismic data was applied using RMS (root mean square calculation). The RMS amplitude attribute covers a 22ms window determined from interpreted top of the sand predicted by tracking high amplitude events. This window is estimated good enough to ensure it can cover all of the turbidite sandstone bodies, the thickest of which was penetrated at HT-3P with a thickness of about 45m (Figure 5). The results of amplitude extraction maps show the predicted distribution of sand body (yellow polygon). Sediment supply from SW-NE, and the extension of sand body to the west and east sides is possibly controlled by syndepositional faults.

3.3. Spectral decomposition

For further investigation of the reservoir in terms of its bearing gas capability, low frequency spectral decomposition attributes have been applied to observe the gas response within reservoir [5, 7]. By screening frequency amplitude to seek the best match with existing gas at wells (Figure 6), it is shown that the most suitable frequency is estimated at around 17 - 19Hz. Hence, high amplitude extraction from 17 - 19Hz spectral decomposition can be useful for identification of gas areas. An extraction amplitude map derived from 19Hz spectral cube shown in Figure 7 shows a high gas saturated in HT-3P, and low gas saturated in HT-2X amplitude response.

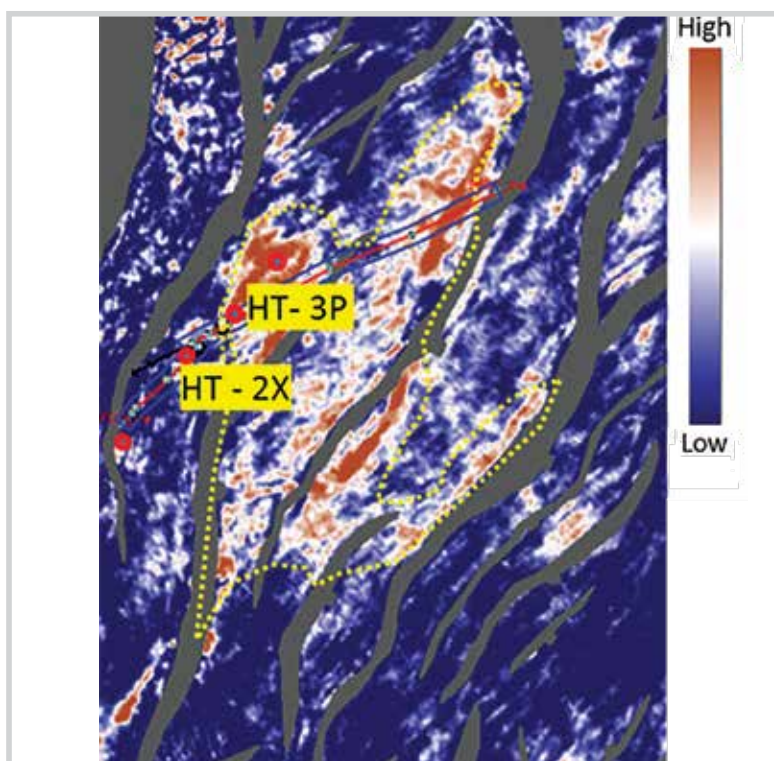
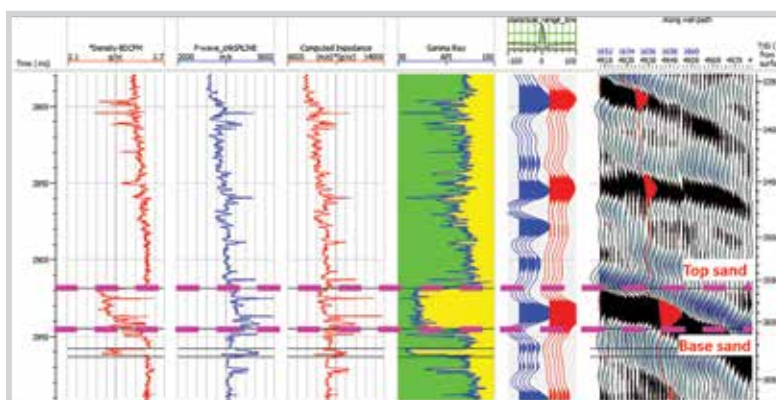
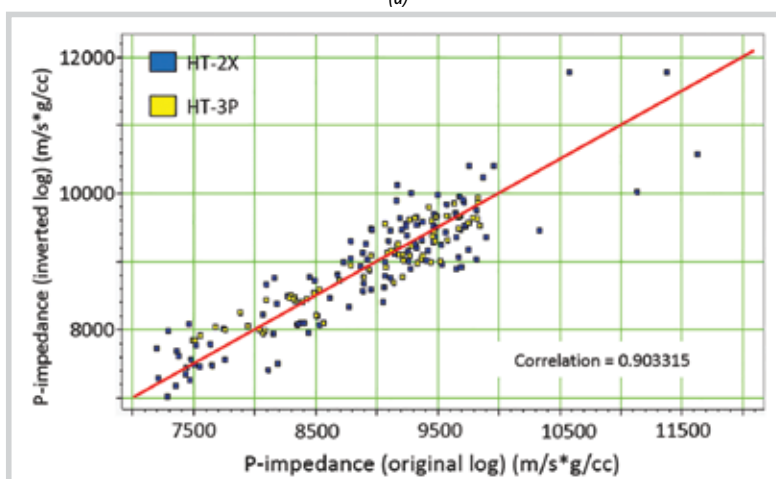


Figure 7. RMS amplitude extraction of 19Hz spectral decomposition cube at the top of sandstone.



(a)



(b)

Figure 8. Synthetic seismogram for well HT-3P(a). The linear relationship showing a good correlation in P-impedance of original logs and inverted results at two well locations (b).

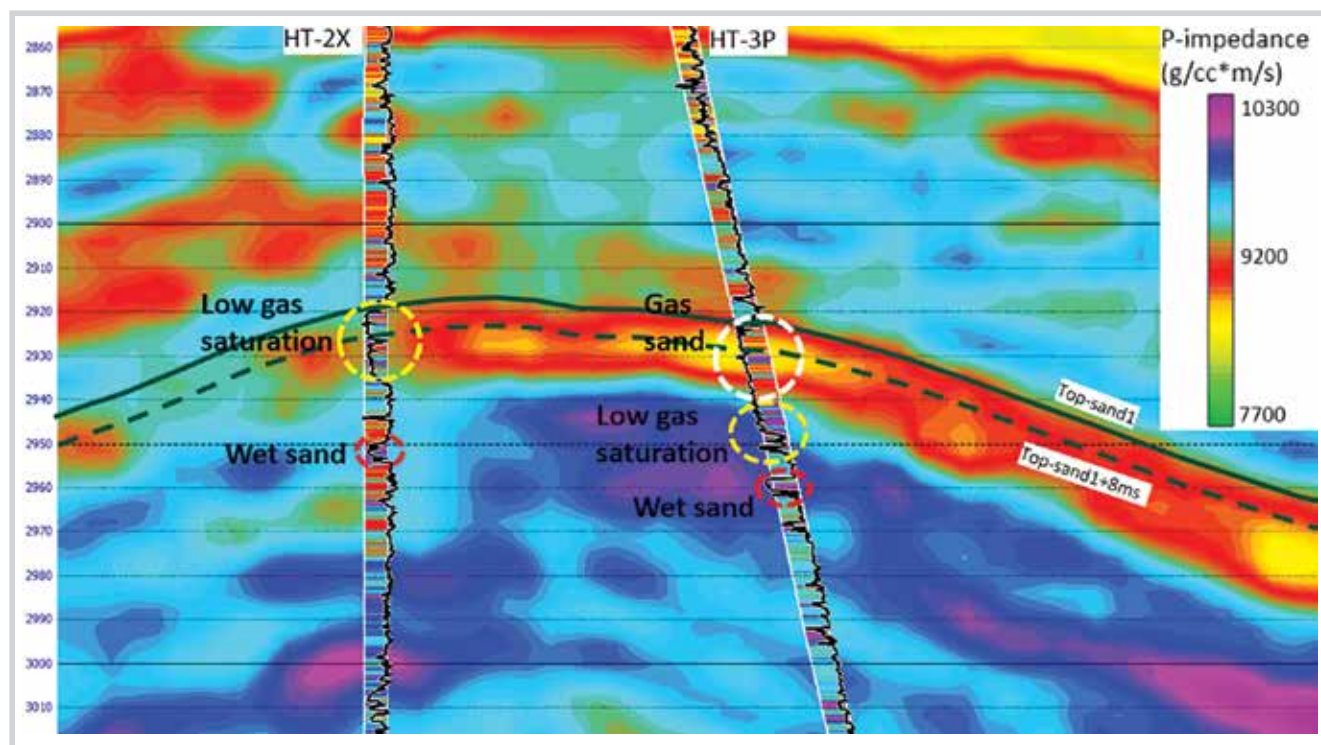


Figure 9. P-impedance generated using model-based inversion at well HT-3P and well HT-2X. The log curve displayed in cross-section is the GR.

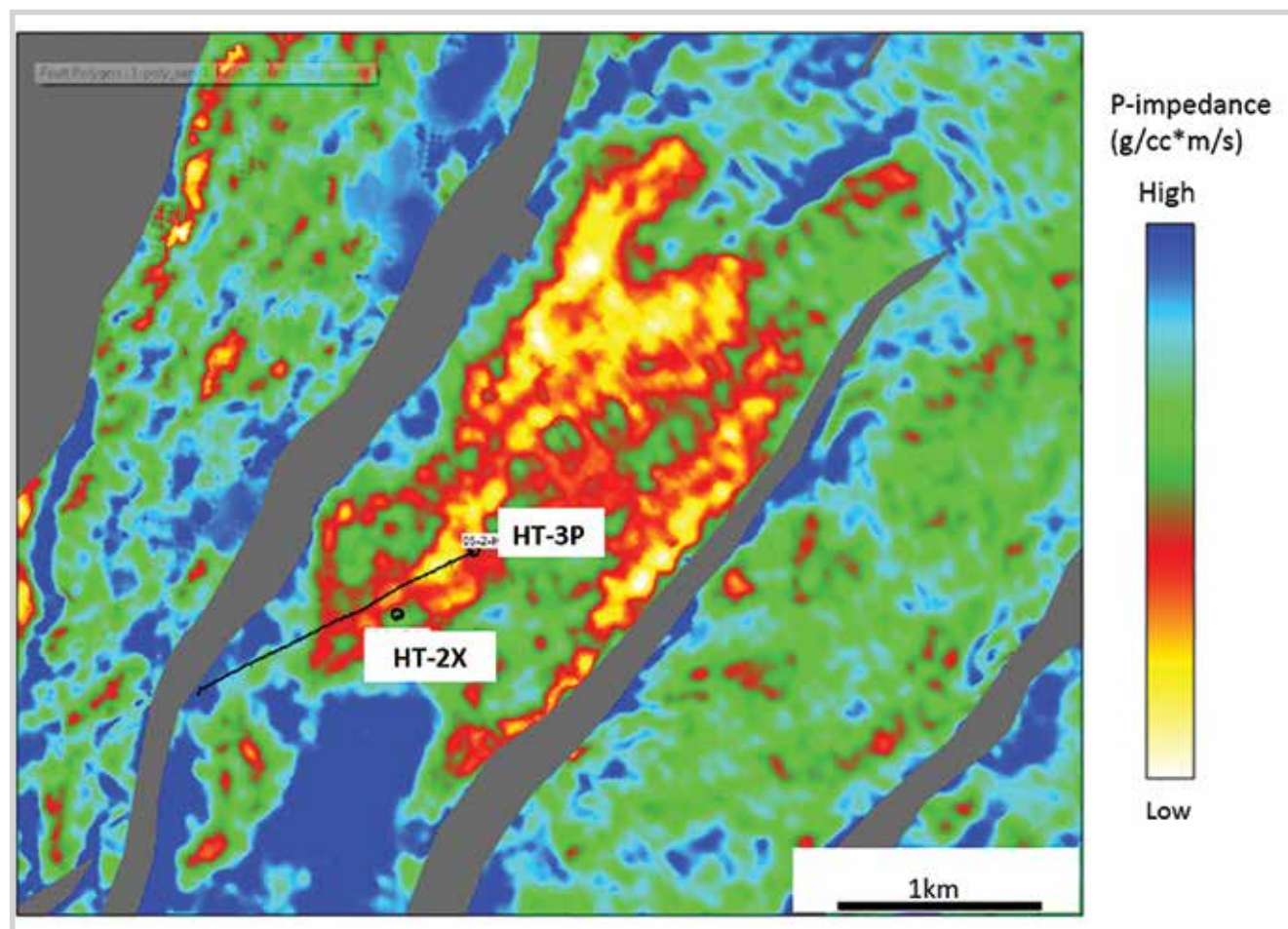


Figure 10. Horizon slice of inverted P-impedance volume extracted at phantom horizon top-sand 1 + 8ms. Low P-impedance only represents at high gas saturation well HT-3P.

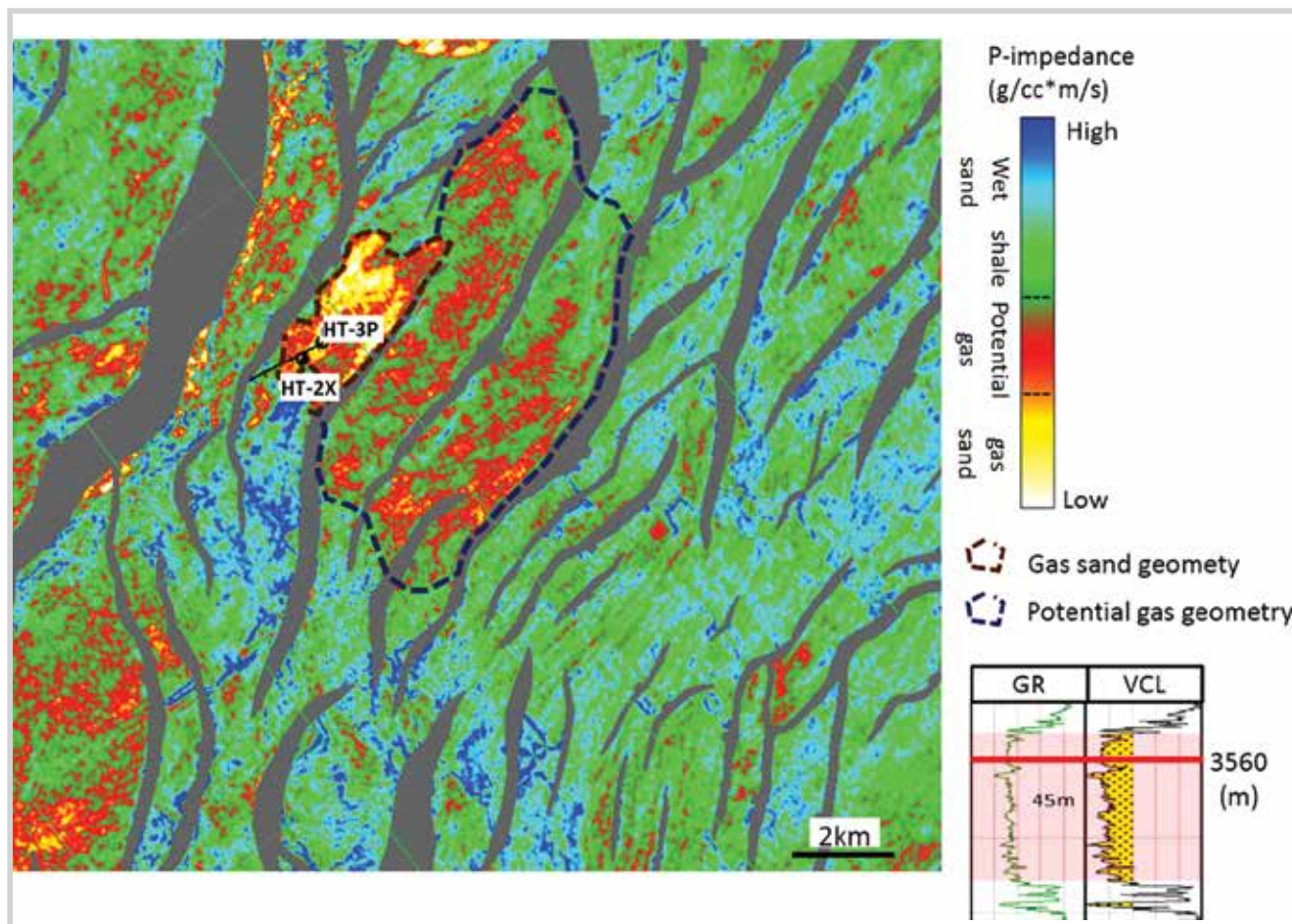


Figure 11. Horizon slice of inverted P-impedance volume extracted at phantom horizon top-sand 1 + 8ms. Low P-impedance indicates gas sand.

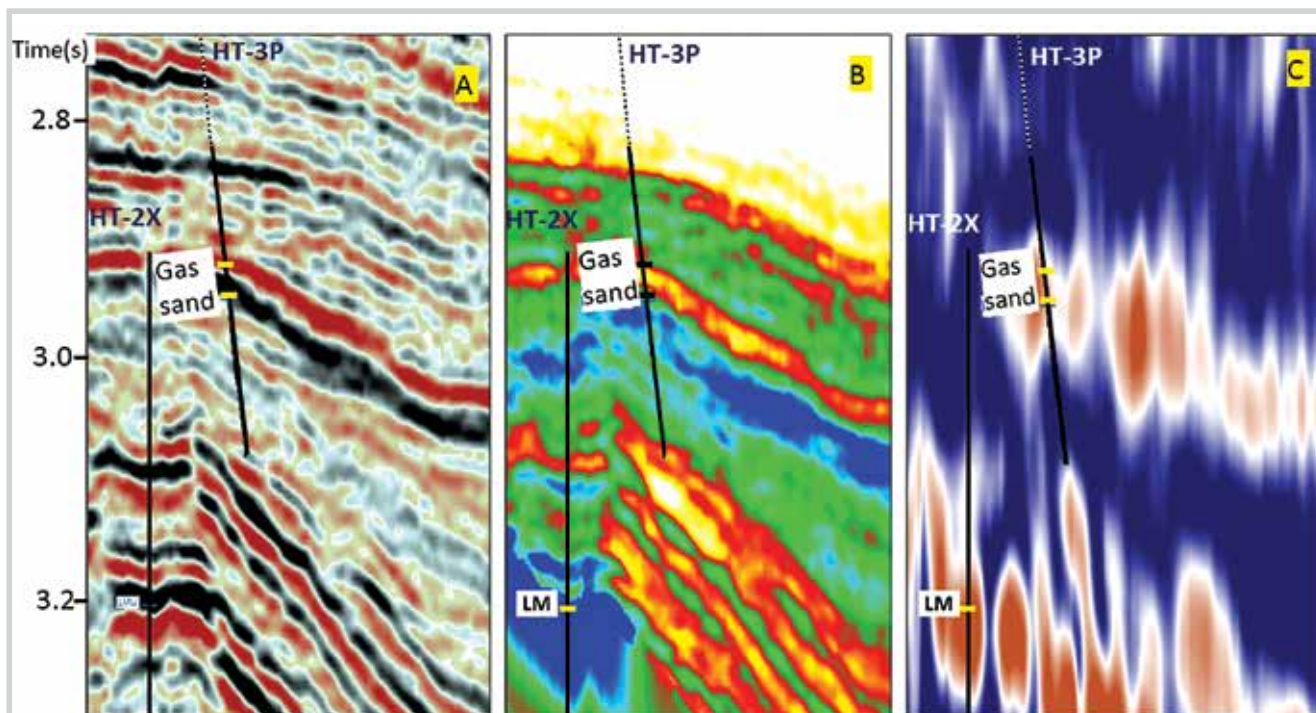


Figure 12. Comparison of full stack seismic data (a) with inverted acoustic impedance section (b) and low frequency (19Hz) spectral decomposition. (c) The gas sand interval was defined at well HT-3P.

3.4. Seismic post-stack inversion

Synthetic seismogram was generated to link the well data and seismic data (Figure 8a). The decrease of acoustic impedance computed on well from sonic and density at the top of reservoir sand corresponds to trough on seismic section. Based on the results of post-stack inversion analysis, it is shown that inverted P-impedance and the well-log calculated P-impedance have a good correlation coefficient, more than 90% (Figure 8b) within the zone of interest from horizon Middle Miocene to horizon Lower Miocene, which covers the reservoir sand interval. Thus, the inverted P-impedance can be reliable for gas sand distribution prediction [8, 9].

At well HT-3P, the lower part of the reservoir (2,920 - 2,930ms) shows a high P-impedance; this interval has low gas saturation as defined from the wells (Figure 9). However, the thickness of wet sand body of two wells (from 2,950 - 2,960ms approximately 8m in thickness) is too thin for inverted P-impedance to work, thus it cannot be recognised on inverted cube due to the resolution of original seismic. Therefore, the inverted P-impedance cube is possibly helpful with sufficient reservoir thickness.

To predict gas sand distribution, extracted P-impedance along horizon with 8ms shifted down top-sand 1 was applied (Figure 9). This extracted low P-impedance surface from inversion volume can provide the possible lateral distribution of gas sands. The low value of the inverted P-impedance along this horizon represents the gas sand distribution of well HT-3P, whereas the low gas saturation well HT-2X location shows high P-impedance (Figure 10). The predicted gas-saturated area is bounded by fault blocks and distributed around the drilled wells (Figure 11).

3.5. Combination of RMS, spectral decomposition low frequency attributes and seismic post stack inversion.

RMS amplitude attribute may be useful as a quick tool to observe the distribution of sands in the area. RMS map shows bright amplitudes for sands. However, RMS computation depends on a window length that may not be appropriate for the variable thickness of sands or sand/shale interbedded layers.

Starting from the preliminary distribution of sand defined by RMS attribute in the study area, a spectral decomposition (limited to frequency of 19Hz) and a seismic post-stack inversion were applied to further

detect gas sand distribution. The position of highly saturated gas sand may be differentiated from low saturated gas sand by observing the high amplitude indication on the low frequency spectral decomposition section. In fact, a high amplitude from the 19Hz spectral decomposition can be observed at the location of well HT-3P, which has high gas saturated sands and similarly, a low amplitude at the location of well HT-2X which has low gas saturation.

Furthermore, in order to investigate the gas sand body, the method of seismic post-stack inversion can provide additional information which does not show up on the low frequency spectral decomposition volume. From the post-stack inversion results, the boundary between higher and lower P-impedance in the inverted volume matched with the formation top and base of gas sand layer at well HT-3P. Thus, the thickness of gas sand layer may be predicted by the thickness of low P-impedance layer observed in inverted section.

Thus, the combination of RMS, spectral decomposition low frequency attributes and seismic post-stack inversion for gas sand prediction can reduce the uncertainty and provide valuable additions to reservoir characterisation in Hai Thach area. Lastly, further information about geology, lithology and drilling is beneficial to make the best possible prediction on gas sand quality and distribution.

4. Conclusions

At Hai Thach field, sands have the same acoustic impedance with interbedded shale. The presence of gas is the main cause for the reduction of the acoustic impedance of sand within the depth interval of 3,500 - 3,600m. Therefore, using inverted volume is effective for gas sand identification.

The RMS attribute is useful to predict sand distribution. High gas saturation zones were delineated by amplitude anomalies of spectral decomposition low-frequency from 17 - 19Hz.

Acoustic impedance extracted from inverted volumes can predict gas sand distribution. The acoustic impedance section can be used for defining the boundary of the gas sand zones effectively.

The combination of acoustic impedance and low-frequency amplitude analysis is critical for reservoir characterisation in Hai Thach area. However, the combination still has some uncertainty, especially within

areas of low gas saturation sand and highly saturated thin gas sands.

References

1. Pham Thanh Liem, Phan Giang Long, Le Hai An. *Some comments on the possibility of Middle/Late Miocene-Pliocene stratigraphic traps in the centre of Nam Con Son basin*. Petrovietnam Journal. 2013; 10: p. 26 - 31.
2. CCOP. *Vietnam petroleum geology and potential*. 2002.
3. Naseer Ahmad, P. Rowell. *Mapping of fluvial sand systems using rock physics analysis and simultaneous inversion for density: Case study from the Gulf of Thailand*. First Break. 1973; 31(5): p. 49 - 54.
4. Bagus Priyanto. *Lithology prediction using rock physics analysis and seismic inversion within Miocene fluvial reservoir interval in the Songkhla basin, Gulf of Thailand*. Chulalongkorn University. 2012.
5. John P.Castagna, Shengjie Sun, Robert W.Siegfried. *Instantaneous spectral analysis: Detection of low-frequency shadows associated with hydrocarbons*. The Leading Edge. 2003; 22(2): p. 120 - 127.
6. Abhinav Kumar Dubey. *Reservoir characterization using AVO and seismic inversion techniques*. The 9th Biennial International Conference & Exposition on Petroleum Geophysics. 2012.
7. Jesus M.Rodriguez. *Spectral decomposition and inversion: Case study of a production area in the Cook Inlet basin, Alaska, USA*. University of Houston. 2009.
8. Mayura Dangprasitthiporn. *Lithology prediction using rock physics and acoustic impedance for reservoir distribution in Northern Pattani basin, Gulf of Thailand*. Chulalongkorn University. 2015.
9. Patricia E.Gavotti, Don C.Lawton, Gary F.Margrave, J.Helen Isaac. *Post-stack inversion of the Hussar low frequency seismic data*. 2013.

KRES-ES™ revamp produces more ammonia from less natural gas by energy substitution

Vikram Singh, Shashi Singh

KBR

Email: vikram.singh@kbr.com

Summary

The 5th KRES™ technology based Ammonia Plant is now in operation in a grass-root project at P.T. Panca Amara Utama (PAU), Indonesia. This follows earlier successful operations in revamp projects - one since 2009 and another since 2015. KBR has therefore studied various schemes in which KRES technology could benefit ammonia plant operators. As a result, KBR is now offering low cost KRES-ES™ technology (patent pending) for revamping ammonia plants by energy substitution.

Ammonia plants having either expensive or curtailed/uncertain supply of natural gas may find this technology a solution to their problem if an alternative source of energy, e.g. coal, is available. It offers an ideal solution for locations facing natural gas shortage or where natural gas is likely to become too expensive to allow viable operations, after building the plant. This enjoys reliability of reforming process (over coal gasification). It also allows the plant to switch totally to natural gas in the future if natural gas becomes available. The revamped ammonia plant requires oxygen and steam imports. Steam import can be met by either using existing capacity or an alternative source of energy. Alternative source of energy may be fossil fuel like coal or other sources. Total natural gas consumption is reduced to less than 6.35 Gcal/MT of ammonia by adding a new reforming exchanger to the existing primary and secondary reformers.

Three examples of KRES-ES based revamps are presented including technical and economic analysis to illustrate the application of this technology.

Key words: KRES™ - KBR reforming exchanger system, ammonia plant, coal, natural gas, ammonia, energy saving.

1. Introduction

Vietnam has a large range of domestic primary energy sources. These resources however are fast depleting. The power sector has grown in Vietnam as also the consumption of natural gas in the generation of power, thus leading to a competing use of natural gas for power generation versus downstream industry. This, along with the government's continued thrust on implementation of energy efficiency measures in operating plants, gives an opportunity to the ammonia industry to consider technology options to address both these needs (a) use of alternate source of energy for ammonia production, e.g. coal and (b) implementing energy reduction measures in their plants.

KRES™ - KBR reforming exchanger system that replaces conventional primary and secondary reformers in an ammonia plant has been in successful commercial

operation [1, 2] in the ammonia plants in Methanex, Canada, since 1994 and in Liaohe, China, since 2003. A reforming exchanger is the heart of the KRES technology. It uses high temperature process heat exiting the secondary reformer (or exiting an auto-thermal reformer) to produce syngas by reforming an additional flow of natural gas and steam. As described in a previous paper [3], KRES has been offered as two process schemes. One of these two schemes is used at Methanex and Liaohe. The other scheme is used in the third KRES unit in the Chambal Fertilizers & Chemicals Ltd Plant. Chambal Fertilizers & Chemicals Ltd. (CFCL) in India commissioned their KRES based revamp project in their ammonia plant-1 that is in successful operation since April 2009. Since then, two more plants have implemented KRES, one in PCS Lima Plant in Ohio (US) in 2015 (Foster Wheeler Technology) and another in the 1,900 million ton per day grassroots KBR technology ammonia plant in P.T. Panca Amara Utama (PAU), Banggai, Indonesia in 2018.

KBR is now offering KRES-Energy Substitution (KRES-ES™) technology (patent pending) as another application

Table 1. CFCL performance summary

	Base 2005	Total revamp expected	Actual 2009 revamp stage-1
Ammonia production (metric tons per day)	1600	2000	1781
Natural gas (Feed + Fuel) (Gcal/MT)	7.84	7.33	7.36
Natural gas + Electric power + Steam (Gcal/MT)	7.88	7.31	7.60

of KRES for revamping ammonia plants. This technology provides a low-cost revamp solution to any existing ammonia plant that has either an expensive, curtailed and/or uncertain supply of natural gas but has an alternative source of energy available. The revamped ammonia plant requires oxygen and steam imports. Steam import can be met by using either existing or new capacity. The source of energy for steam could be fossil fuel (e.g. coal) or another non-fossil energy source.

Total natural gas consumption is reduced to less than 6.35 Gcal/MT of ammonia by adding a new reforming exchanger to the existing primary and secondary reformers. This technology can be used to dramatically reduce the dependence on natural gas while either keeping the same ammonia production capacity or increasing it. Three examples of KRES-ES based revamps are presented in this paper with their technical and economic analysis to illustrate the application of this technology.

2. CFCL revamp project

CFCL operates two ammonia plants in Gadepan, India. The first plant having a 1,500 ton per day design capacity, based on Haldor Topsoe technology, was commissioned in 1994. In 2005, CFCL decided to revamp this plant to increase its capacity and improve energy efficiency and therefore awarded revamp studies to both, Haldor Topsoe, the technology provider of the original plant, and KBR. After comparing the revamp process technologies offered by both parties, CFCL decided to implement the revamp project using KBR technology, including KRES as its key feature, as it provided better energy efficiency as well as better operability.

From 2006 to 2008, the revamp project went through its basic and detailed engineering, procurement and construction. The project had been divided into two phases; and stage-1 was successfully commissioned in April 2009. Stage-1 includes KRES, a synthesis loop upgrade plus other miscellaneous items. After implementing the full revamp changes, KRES application will increase syngas generation capacity by more

than 30%. The loss of ISBL steam generation per ton of ammonia due to KRES is offset by improved heat recovery as well as by reducing the ISBL energy consumption. Thus the energy efficiency of the ammonia plant is improved as summarised in Table 1.

The prior conventional reforming system of primary and secondary reformers has been upgraded with KRES consisting of the existing primary reformer, a secondary reformer and the reforming exchanger. KRES in operation in the CFCL ammonia plant since April 2009 is shown in Figure 1. The CFCL reforming exchanger, a compact piece of equipment, is located in front of the large side fired reformer furnace. The reforming exchanger effluent flows to the inlet of the existing reformed gas waste heat boiler. It contributes more than 30% of the syn-gas generation capacity. Besides contributing to capacity and efficiency improvement of the ammonia plant, it has improved the performance of the old reformed gas waste heat boiler by reducing its inlet temperature and thus its thermal and mechanical stresses. Boiler outlet temperature is lower so it improves the HT shift converter conditions. Operating conditions of the primary reformer are also milder as radiant duty is reduced.

3. KRES-ES™ process scheme

The KRES-ES process is configured to enable all ammonia plants to reduce their dependence on natural gas requirement by adding minimum equipment to provide a low-cost revamp technology solution. Ammonia plants having one or more of the following problems in the supply of their natural gas feed-stock can benefit from this technology: expensive, uncertain supply in the future, erratic or curtailed. Due to high product demand, some owners also need to increase their plant capacity but are hesitant due to lack of long term natural gas supply commitments. Ammonia plants in some countries are also looking for revamp options to reduce their CO₂ emissions and carbon footprint. KRES-ES process technology provides the right solution to all such ammonia plant owners, provided a suitable alternative source of energy is available to owners to



Figure 1. KRES in operation in CFCL ammonia plant.

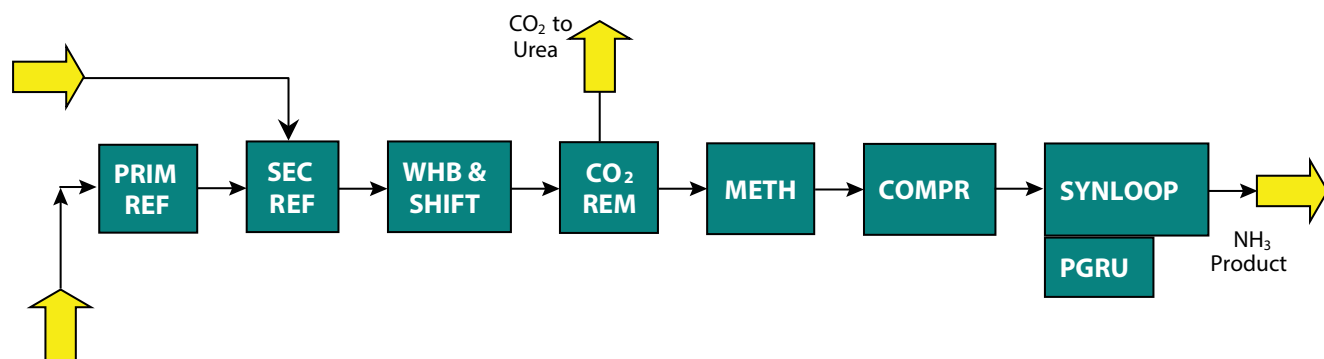


Figure 2. Ammonia Plant before revamp.

enable the “Energy Substitution (ES)” function to reduce use of natural gas.

Existing ammonia plants with a conventional reforming system have a primary reformer furnace followed by a secondary reformer to produce synthesis gas as shown in Figure 2. All such conventional plants can be revamped by upgrading their reforming system to KRES-ES as conceptually shown in Figure 3. A reforming exchanger will be tied in between the secondary reformer and the reformed gas waste heat boiler. A portion of the feed natural gas and steam mixture is fed to the reforming exchanger having conventional nickel based catalyst in its

tubes where syngas is produced using high grade process waste heat.

Comparing the two schemes on equal syngas production basis as shown in Figures 2 and 3, heat duty on the existing primary reformer is reduced to about one third of that in the conventional existing system (Figure 2). Fuel gas consumption is significantly reduced. The existing furnace is reconfigured to a “Lite Reformer” by making minor mechanical changes. Imported oxygen is mixed with process air - to make enriched air with about 30 mol% O₂ which is fed to the secondary reformer to complete the revamped system.

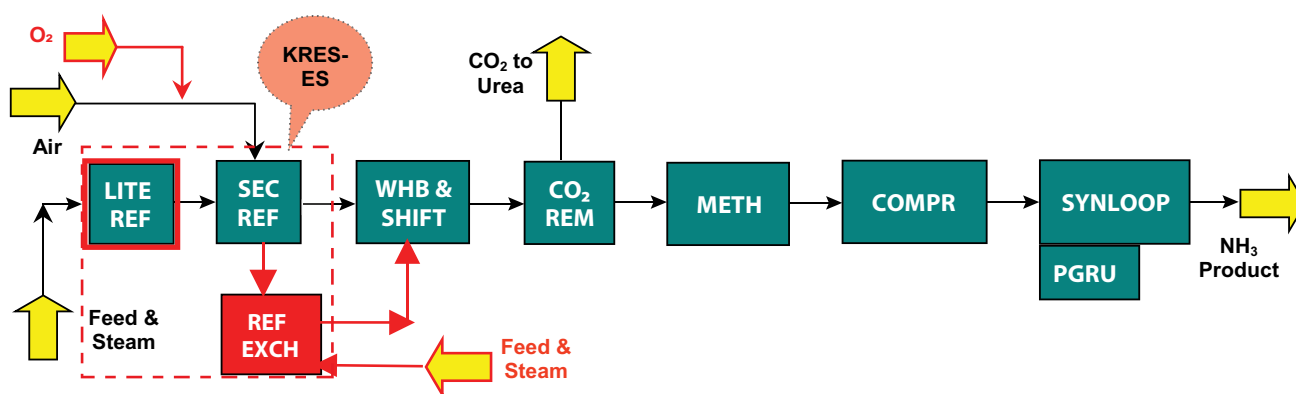


Figure 3. Ammonia Plant after revamp.

Table 2. Comparison of parameters before and after revamp

	Before	After revamp
Primary reformer radiant duty (%)	100	33
Primary reformer mixed feed & outlet temperatures (°C)	560 & 800	Much Less
RG waste heat boiler inlet temperature (°C)	960 - 1,000	700 - 800
RG waste heat boiler heat duty (%)	100	60 - 70

Substitute energy (to replace natural gas) can be from any source that can provide steam to the ISBL ammonia plant to meet the shortfall created due to the reduced duty of the reformed gas waste heat boiler. For example, a coal or pet coke fired boiler can be used to accomplish this or surplus steam from a power plant using non-fossil fuel may be used. A supply of oxygen is also required to enrich the process air. Oxygen can be drawn from a close-by plant or from an existing pipeline network, if available or produced in new oxygen package unit using alternative source of energy. Process steam import requirement will depend on how much heat load of the HP Boiler is being used for meeting reforming reaction's endothermic heat requirement in the KRES unit. However, steam import can be reduced by switching some turbine drivers to electric drivers or by improving ISBL waste heat recovery or by reducing ISBL process heat consumption in the CO₂ removal system. Depending upon the conditions of the existing plant, it may be possible to avoid or significantly minimise the requirement of import steam by using suitable heat integration.

In most cases, the natural gas consumption of the ammonia plant is reduced to below 6.35 Gcal/MT of ammonia from present natural gas consumption of 7.3 to 9.5 plus Gcal/MT irrespective of the technology of the current plant and its furnace type. However, the total energy (natural gas plus the substitute source) consumption may or may not be reduced.

4. Low-severity equipment duty

KRES-ES has additional advantages as it reduces operating parameter severity which leads to improved mechanical reliability of the existing equipment post revamp. Operating conditions of both (a) primary reformer furnace and (b) reformed gas waste heat boiler become very mild post revamp, and typical benefits are identified in Table 2. Thus plants requiring maintenance/replacements in these two critical and expensive pieces of equipment may expedite implementation of their KRES-ES based revamp to avoid such expensive repair and/or equipment replacement including a furnace re-harp.

5. Increased CO₂ availability

In most cases KRES-ES produces sufficient CO₂ by-product that is adequate to convert all the NH₃ production to urea. This is very valuable to plants that can sell only urea (no ammonia) and have a CO₂ shortfall, since surplus syngas need not be diverted to fuel or an expensive flue gas CO₂ recovery unit is not required for production of additional CO₂.

6. Revamp examples

Examples of ammonia plant revamps help illustrate how incorporating KRES-ES technology in the revamp flowsheet reduces the dependence on natural gas supply. It significantly improves the economics of the whole operation with or without a capacity increase of the

Table 3. Key features of revamp example 1

	Base	Revamped
Plant capacity (metric tons of ammonia per day)	1,200	1,200
*Average capacity utilisation per year	85%	100%
Incremental ammonia produced per year (MT)	-	61,200
ISBL natural gas consumption (Gcal/MT)	9.0	6.35
Coal used OSBL to substitute energy (Gcal/MT)	0	2.65
**Mild operating condition of reformer furnace & RG-WHB	No	Yes
Reduced annual cost of energy - since coal costs less	-	Yes
Energy wastage avoided - stable throughput, no turndown	No	Yes
***Simple payback period (years)	-	2

*Loss of capacity utilisation due to other factors (than natural gas curtailment) is excluded for clarity. Costs of natural gas and coal are USD 4.0 and USD 2.0 per MMBTU respectively. Ammonia sale price at the gate is USD 250 per metric ton. **Savings made by avoiding reharp of the reformer furnace and a RG-WHB maintenance is not considered in payback. ***Benefit of additional CO₂ is not considered in payback.

Table 4. Key features of revamp example 2

	Base	Revamped
Plant capacity (metric tons of ammonia per day)	1,200	1,500
Capacity utilisation using revamp case natural gas flow (MT/day)	1,060	1,500
Incremental ammonia produced per year (MT)	-	149,600
ISBL natural gas consumption (Gcal/MT)	9.0	6.35
Coal used OSBL to substitute energy (Gcal/MT)	0	2.65
**Mild operating condition of reformer furnace & RG-WHB	No	Yes
Reduced annual cost of energy - since coal costs less	-	Yes
Energy wastage avoided - stable throughput, no turndown	No	Yes
***Simple payback period (years)	-	3.2

*Loss of capacity utilisation due to other factors (than natural gas curtailment) is excluded for clarity. Costs of natural gas and coal are USD 4.0 and USD 2.0 per MMBTU respectively. Ammonia sale price at the gate is USD 250 per metric ton. **Savings made by avoiding reharp of the reformer furnace and a RG-WHB maintenance is not considered in payback. ***Benefit of additional CO₂ is not considered in payback.

plant. Here are three examples based on KBR studies and projects.

6.1. Example 1: Improved capacity utilisation

This example describes a revamp where the plant has curtailed and erratic supply of natural gas. Natural gas curtailment is greater in winter when more gas is diverted by the supplier to higher priority users. The plant operates at capacities as low as 70% throughputs in winter and annual average capacity utilisation is only 85% for this 1,200 metric ton per day capacity plant. The increased capacity of over 1,200 metric tons per day is not required so the plant is revamped using the KRES-ES scheme (Figure 3) to reduce its dependence on natural gas and thus enabling it to operate at 1,200 metric ton per day capacity throughout the year even as gas supply is curtailed by up to 30%. Key features of this revamp case are summarised in Table 3.

6.2. Example 2: Revamped to increase plant capacity

This example describes a revamp where the plant has

curtailed and erratic supply of natural gas as well as a robust market demand for ammonia. The plant operates at reduced throughputs, especially in winter. The owner is expecting a new natural gas supply contract but is concerned that the plant may be caught with curtailments in long term after spending on the capacity increase revamp project.

The revamp project is implemented to increase capacity to 1,500 metric tons per day from the present 1,200 metric tons per day using KRES-ES scheme (Figure 3). Besides revamping of the reforming system to KRES-ES, other parts of the plants are also modified to accommodate the increased throughput. Total natural gas consumption is 12% lower even at 1,500 metric ton per day production than what it was before the revamp and the plant will operate at 1,500 metric ton per day capacity throughout the year even as gas supply is curtailed. Key features of this revamp case are summarised in Table 4.

6.3. Example 3: CO₂ emission reduction

This example describes a revamp where the plant must reduce its CO₂ emissions significantly to meet new

Table 5. Key features of revamp example 3

	Base	Revamped
Plant capacity (metric tons of ammonia per day)	1,200	1,200
ISBL natural gas consumption (Gcal/MT)	9.0	6.35
Mild operating conditions of reformer furnace & RG-WHB	No	Yes
*CO ₂ emissions reduced	Base	30%

*Incremental CO₂ by product flow is excluded from the quoted emissions; since it is either used in the urea plant or recovered as a product. Note: Savings made by avoiding reharping of the reformer furnace and RG-WHB maintenance is not considered in payback.

Table 6. KRES-ES revamp example summary

Example	1	2	3
Ammonia production increased (metric tons per year)	61,200	149,600	None
Energy cost reduced significantly by substitution	Yes	Yes	Yes
Furnace/RG-WHB reliability improved & more CO ₂ for urea	Yes	Yes	Yes
Typical payback period (years)	2	3.2	-
Potential CO ₂ emissions reduction	None	None	30%

regulations. Revamping this vintage plant to improve its energy efficiency to the level of a new plant in order to reduce CO₂ emission is cost prohibitive. KRES-ES is incorporated to reduce consumption of natural gas of the ammonia plant to 6.35 Gcal/MT. The ISBL ammonia plant requires HP steam import as well as O₂ from OSBL. Both of these requirements are met by sourcing suitable quality of steam from a nearby power plant that uses non-fossil fuel as the source of energy. The oxygen plant drives its air compressor using this imported steam or alternatively it can use electric power supplied by the same power plant. Feasibility of sourcing the steam to OSBL of ammonia plant from such a non-fossil fuel based power plant needs to be confirmed for specific location. Key features are summarised in Table 5.

7. Conclusions

KRES-ES™ technology provides an economical revamp solution to any existing ammonia plant that is suffering from either expensive or curtailed and uncertain supply of natural gas but has an alternative source available for energy substitution (ES). It also has potential application for reducing ISBL ammonia plant’s CO₂ emission or carbon footprint for countries where such regulation is enforced. The revamp examples illustrate that KRES-ES can be used to provide a customised revamp flowsheet to all ammonia plants that can benefit from energy substitution as summarised in Table 6.

Cost of revamp would depend on the extent of modification required in the flowsheet including other constraints which the plant has to incorporate in those changes, eg. steam balance, air compressor capacity and reformer furnace constraints.

References

1. X.Shen, X.Xu, W.Feng, S.Singh, A.Malhotra. *Largest KRES reformer in service in China*. Nitrogen and Methanol. 2005; 274: p. 39 - 46.
2. Avinash Malhotra, Paul Kramer, Shashi Singh. *Revamp of Liaohes ammonia plant with KRES technology to reduce natural gas usage*. AIChE Ammonia Safety Symposium, Denver, USA. 2004.
3. S.Singh, A.Jing. *KRES technology makes ammonia plant revamping viable*. GazChem 2007, Trinidad & Tobago. 2007.
4. Danish Energy Agency. *Vietnam energy outlook report*. 2017.
5. Upendra Singh, Shashi Singh, Avinash Malhotra. *Successful operating experience of CFCL ammonia plant revamped with KBR KRES™ technology*. Ammonia Technical Manual. 2011.
6. Timothy Kearns, Kim Taniguchi, Akhil Nahar, Tim Rembold. *Successful project execution and commissioning of largest capacity KRES™ ammonia unit*. AIChE 2016.

Approaches to enhance the value of Ca Voi Xanh gas via its transformation into nanocarbon materials

Nguyen Huu Luong¹, Nguyen Hoang Viet¹, Nguyen Van Dung²

¹Vietnam Petroleum Institute

²Ho Chi Minh City University of Technology

Email: luongnh@vpi.pvn.vn

Summary

Ca Voi Xanh gas has high contents of impurities, namely H₂S, CO₂ and N₂. The transformation of this gas into high-value products is a potential approach to enhance its value without pre-treatment. In fact, it is a promising feedstock for nanocarbon production, including carbon nanotubes (CNT) and carbon nanofibres (CNF). Their applications can be found in various areas of which markets are promising. Two methods for nanocarbon production can be considered, namely methane decomposition and dry reforming of methane. Methane decomposition brings higher nanocarbon yields while dry reforming of methane can produce better quality nanocarbon products. A number of issues need to be solved before these processes can be commercialised, such as improvements of nanocarbon yields and their recovery methods.

Key words: Ca Voi Xanh gas, carbon nanotubes, carbon nanofibres, methane decomposition, dry reforming.

1. Introduction

In 2011, Ca Voi Xanh gas field was discovered about 100km off the coast of the central region of Vietnam. Its reserve was found more than 150 billion m³ of natural gas. However, its gas composition consists of high contents of impurities, namely H₂S, CO₂ and N₂. Table 1 shows its hydrocarbon and non-hydrocarbon composition [1]. It can be seen that this gas contains significant contents of undesired components, including 0.21% of H₂S, 9.88% of N₂ and 30.26% of CO₂. As fuel for power generation, the gas will be treated for H₂S removal so that its remaining H₂S content is less than 30ppm. On the other hand, CO₂ and/or N₂ removal should be considered upon its uses and available technologies for its treatment and deep processing. It is, therefore, interesting and significant to develop new technologies that can transform Ca Voi Xanh gas into high-value products without pre-treatment for CO₂ and/or N₂ removal.

A potential approach to enhance the value of Ca Voi Xanh gas is to transform it into high-value products such as carbon nanotubes (CNT) and carbon nanofibres (CNF). Nanocarbon materials can be produced from hydrocarbons, oxygens, and even CO₂. One of the

Table 1. Composition of Ca Voi Xanh gas

Component	Composition (mol %)
N ₂	9.88
CO ₂	30.26
H ₂ S	0.21
C ₁	57.77
C ₂	0.92
C ₃	0.31
C ₄	0.18

popular feedstocks for CNT production is methane. In terms of economy, a preliminary estimation shows that dry reforming of methane and methane decomposition are possible approaches to compete with the current method of hydrogen production using steam reforming of methane if the values of CNT and CNF as by-products are included [2]. In fact, by this approach, Ca Voi Xanh gas can be processed without any pre-treatment for CO₂ and N₂ removal. However, a number of issues need to be resolved before it can be commercialised, including the improvement of feed conversion and nanocarbon selectivity, as well as recovery methods. Therefore, it is important to investigate the potential of transformation of this gas into nanocarbon materials.

2. Markets for nanocarbon materials

The world demand for CNT was 5,000 tons/year in 2014 and predicted to be 20,000 tons/year by 2022. CNT's

Table 2. Market analysis for various carbon products [3]

Type of carbon	Types of applications	Expected price for carbon	Size of the market (current/ projected)	Corresponding hydrogen production ^(a)
Carbon black	Tires, printing inks, high-performance coatings and plastics	USD 0.4 - 2+/kg depending on product requirements	U.S. market • ~2M MT (2017) Global market • 12M MT (2014) • 16.4M MT(2022)	U.S. market • 0.67M MT Global market • 4M MT (2014) • 5.4M MT (2022)
Graphite	Lithium-ion batteries	USD10+/kg	Global market • 80K MT (2015) • 250K MT (2020)	Global market • 27K MT (2015) • 83K MT (2020)
Carbon fibre	Aerospace, automobiles, sports and leisure, construction, wind turbines, carbon-reinforced, composite materials and textiles	USD 25 - 113/kg depending on product requirements	Global market • 70K MT (2016) • 100K MT (2020)	Global market • 23.3K MT (2016) • 33.3K MT (2020)
Carbon nanotubes	Polymers, plastics, electronics, lithium-ion batteries	USD 0.10 - 600/gram depending on application requirements	Global market • 5K MT (2014) • 20K MT (2022)	Global market • 1.7K MT (2014) • 6.7K MT (2022)
Needle coke	Graphite electrodes for electric arc steel furnaces	~USD 1.5/kg	Global market • ~1.5M MT(2014)	Global market • ~0.50M MT (2014)

^(a)Based on stoichiometric ratio of carbon to hydrogen present in methane. Does not take into account process efficiency or use of hydrogen to provide process heat or loss of hydrogen during hydrogen recovery.

sale price is in the wide range of USD 0.1 - 600/gram depending upon its quality and application [3]. For high quality SWCNT (single-walled CNT), the market price can be well above USD 1,000/gram. Applications of CNT can be found in various areas, including plastics, electronics, and batteries, etc. The global demand for CNF is even higher than for CNT, with 70,000 tons/year in 2016 and is forecasted to be 100,000 tons/year by 2022. The sale price of CNF is in the range of USD 25 - 113/kg [3]. CNF can be used in various industries such as energy, materials, aerospace, textiles, and construction, etc. Table 2 shows market analysis for various carbon products.

The CNT market is predicted to grow from USD 3.95 billion in 2017 to USD 8.7 billion by 2022 [4]. A certain of current CNT producers can be listed as Arkema S.A. (France), Arry International Group Ltd. (China), Carbon Solutions Inc. (US), Cheap Tubes Inc. (US), CNano Technology Ltd. (US), CNT Company Ltd. (South Korea), Hanwha Chemical Co. Ltd. (South Korea), Hyperion Catalysis International Inc. (US), Kumho Petrochemical Company Ltd. (South Korea), Nano-C Inc.(US), Nanocyl S.A. (Belgium), NanoIntegris Inc. (US), NanoLab, Inc. (US), Nanoshell LLC (US), Nanothinx S.A. (Greece), Showa Denko K.K. (Japan), SouthWest NanoTechnologies Inc. (US), Thomas Swan & Co. Ltd. (UK), and Toray Industries, Inc. (Japan). Currently, the United States, China, and Turkey are the top countries in CNT production with productivity of 34%, 32%, and 12%, respectively [3].

3. Methods to transform natural gas into nanocarbon materials

Being a valuable material, it is evident that much focus in academia and industry is on the synthesis of this material, especially from abundant sources such as natural gas. Based on methane or natural gas as feedstock, CNT and CNF can be produced in two ways: (1) methane decomposition; (2) dry reforming [4 - 10]. These processes also generate hydrogen or syngas that can be used as feedstock for refineries and petrochemical plants.

3.1. Methane decomposition

To date, CNT is often produced via arc discharge, laser ablation or catalytic chemical vapour deposition (CCVD). Of these approaches, CCVD is the most promising for medium scale production due to its high yield of CNT from the precursor, low energy cost and good controllability [10]. Currently, CNT and CNF production is mainly based on methane decomposition (Equation 1). It has been found that selectivity to CNT and CNF is 50 - 70% and depends on feed purity, reaction temperature, and catalyst nature. From Table 1, it can be seen that Ca Voi Xanh gas owns very low concentration of C₂₊ hydrocarbons, therefore, it seems to be an ideal feedstock for high quality CNT and CNF production.



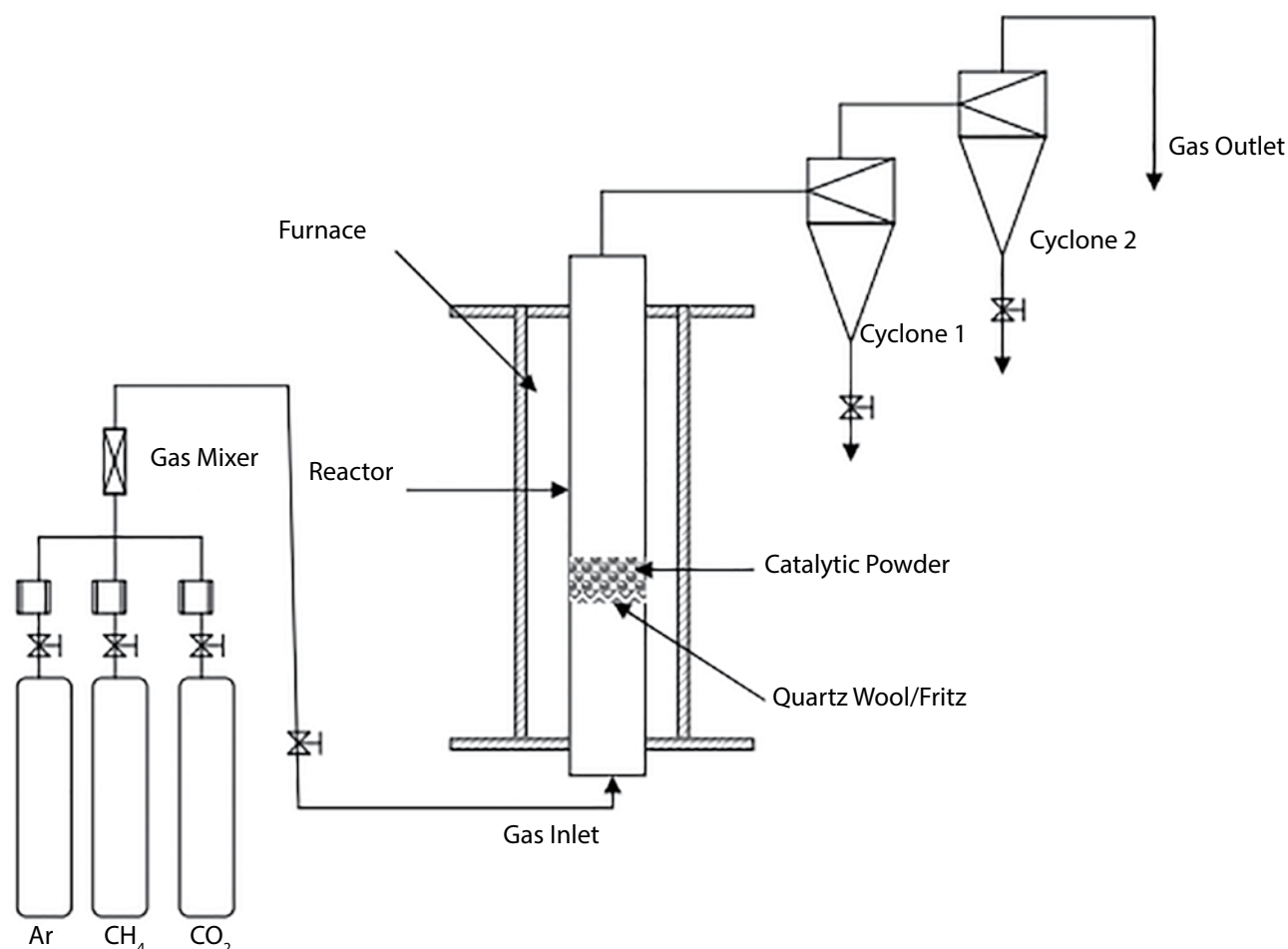


Figure 1. Diagrammatic representation of the CCVD for CNT production [11].

The CCVD process of natural gas principally involves the decomposition of methane molecules to form deposited carbon and hydrogen gas, which is a valuable by-product. Due to strong C-H bonds, this decomposition process is typically conducted inside the range of 750 - 1,000°C [11, 12]. It is well known that CNT is formed at elevated temperature, whilst carbon nanofibres (CNF) is formed at lower temperature. This fact is explained by the competition between carbon nucleation step on the catalytic surface and diffusion of carbon atoms along the formed CNT. A diagrammatic representation of the CCVD is illustrated in Figure 1.

Main catalysts used in the synthesis of CNT are Ni, Fe and Co because these materials are economical, catalytically active and having good carbon solubility [9, 12]. Particularly for Ni, the formation of amorphous carbon at high temperature is an issue which requires special design of carrier phase [13]. Depending on the strong or weak interaction between catalytic particles and carrier phase, base-growth (e.g. most Fe-based catalysts) or tip-growth are the two widely accepted mechanisms

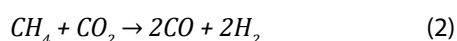
for the formation of CNT. The use of substrate with well-defined distribution of catalytic particle sizes successfully permits the alignment and diameter control of SWCNT growth from ethylene [14] and highly pure methane [15]. Synthesis of SWCNT from methane was also reported at "soft" conditions (i.e. 680°C) using Fe and promoter Mo on alumina as catalyst, though the product yield (by catalyst weight) is only about 20% [16]. Production of CNT from usual catalyst powder is possible, but potential drawbacks are the lack of directional control and additional purification step, which can be time-consuming. Growth of CNT from metal-free substrate such as SiO_x or SiC is attractive since metal impurities in end products are low but the underlying mechanism is less well understood [17, 18].

Although the presence of CO₂ in the feedstock reduces carbon yield during CCVD process, the following benefits are also included: (1) CNF selectivity is increased because amorphous carbon is removed; (2) required temperature for CNF formation is lowered, from higher than 700°C down to 600°C; and (3) smaller tube diameter

and improved oxidative properties of the CNF/CNT products [8]. It has been found that feed with an equal molar ratio of CH₄/CO₂ brings the best result. In addition, if the reaction is carried out at 700°C, CNT is found to be the main nanocarbon product. However, several challenges still need to be addressed before CNT production technology reaches maturity, for example the selective growing of metallic or semi-conducting CNT, control of wall number, chirality and defects in the final products [18]. Ca Voi Xanh gas contains approximately 30% of CO₂, it is therefore worthy to investigate its transformation into CNF and CNT products.

3.2. Dry reforming of methane

Dry reforming of methane has been studied for syngas production (Equation 2) but could not be commercialised due to strong coke formation, leading to fast catalyst deactivation.



Recently, this process has been interested in the aspect of CNT and CNF production. This process generates high-quality nanocarbon products but its conversion is much lower than methane decomposition [8]. Therefore, it is necessary to develop more effective catalysts and nanocarbon recovery methods. Compared with the way of methane decomposition, dry reforming can be carried

out at lower temperature and produce syngas as feedstock for petrochemical industry. Table 3 shows results for CNT production by various methods.

It has been reported that factors, namely ratio of CH₄/CO₂, reaction temperature, and catalyst composition, have significant influences on CNT yield and quality during dry reforming of methane. The optimum condition for the best result was obtained at the CH₄/CO₂ ratio of 2.125, temperature of 700°C, and Ni-based catalyst [5]. Thus, Ca Voi Xanh gas is a good candidate as feedstock for this process. Similar to CCVD, there are still a number of issues to be resolved so that this process can be commercialised, including: (1) development of new catalysts that lower the reaction temperature to below 700°C and improve conversions of CH₄ và CO₂ for CNT formation, as well as catalyst life; (2) development of effective methods of nanocarbon recovery; and (3) controllability of product physical and chemical properties.

4. Applications of nanocarbon materials

CNT has promising applications in development of materials science, electronic products and medical engineering. Because CNT is a good conductor, the material has been commercially used as a conducting additive for lithium-ion battery anode and cathode. Furthermore, loading of iron oxide into multi-walled CNT

Table 3. A summary of various methods of CNT production [19]

Synthesis method		Reaction catalyst	Conditions	Products
Dry reforming reactions	CH ₄ dry reforming	NiAl, NiAlMg, NiAlCe, NiAuAl, NiPtAl, NiAuPtAl, NiAuPtAlMg, NiAuPtAlCe	750°C, 1atm pressure, 24 hours long run test	9.48wt% bamboo-like CNTs on NiAuPtAl
	Glycerol dry reforming	Ni/Al ₂ O ₃ , 3wt% La-Ni/Al ₂ O ₃ , 5wt% La-Ni/Al ₂ O ₃	750°C, 1atm pressure	55wt% and 30wt% bamboo-like CNTs on Ni/Al ₂ O ₃ and 5wt% La-Ni/Al ₂ O ₃
Hydrocarbon thermal decomposition	Methane thermal decomposition	Ni nanoparticles	930°C, 1atm pressure	86wt% - 87.5wt% bamboo-like CNTs on Ni nanoparticles
		Ni-Cu/Al ₂ O ₃	720 - 770°C, 1atm pressure	0.7 - 33mg C/mg Ni bamboo-like CNTs on Ni-Cu/Al ₂ O ₃
		Ni and Ni-Cu alloys	750°C, 1atm pressure	407g C/g Ni bamboo-like CNTs on Ni ₄₇ Cu ₅₃ /CNT
Special chemical vapor deposition	Catalytic chemical vapor deposition	LaNiO ₃ perovskite	800°C and 900°C, 1atm pressure	68.8wt% and 49.3wt% bamboo-like CNTs on LaNiO ₃
	Detonation-assited chemical vapor deposition	Ni nanopartides with the doping of sulfur	900°C, 40MPa pressure	High quality bamboo-like CNTs on Ni without S
	Microwave plasma enhanced chemical vapor deposition	Thermally oxidised silicon substrates with a platinum thin film catalyst	1,000°C, 2,780Pa pressure	Vertically aligned bamboo-like CNTs on Pt film
Pyrolysis and gasification of plastic	Pyrolysis of low density polyethylene feedstock	Nickel, iron, cobalt and copper catalysts	800°C, 1atm pressure	45.7mg C/g plastic and ~180mg C/g plastic bamboo-like CNTs on Ni/Al ₂ O ₃ and Fe/Al ₂ O ₃

(MWCNT) has shown stable and high specific capacity after many cycles [19]. Protocol for development of field-effect transistor based on SWCNT has even been proposed, but widespread applications are yet to be seen due to inconsistent electrical performance [20, 21]. CNT can also be used as cathode in high-performance Field-Emission Lamp (FEL) thanks to the material's excellent conductivity and mechanical/chemical stability. In addition, the CNT-based cathode has low energy consumption, good efficiency and is able to generate different colours [21].

Thanks to exceptional stiffness and strength, CNT holds great promise for fabrication of nanoelectromechanical systems (NEMS), including mass/force sensors and actuators. Another area for potential application of CNT is biomedical engineering such as drug delivery system and tissue engineering scaffolds [22]. Especially regarding the latter, the inclusion of CNT into the natural tissues helps improve material resilience. However, issues of cytotoxicity need to be resolved to ensure safe applications of CNT-based components in human body. Combination of engineered polymers and MWCNT is another area which currently attracts attention [2]. Finally, CNT can also be used in paint coating, drilling muds and water purification systems [23].

5. Conclusions

Ca Voi Xanh gas is a promising feedstock for nanocarbon production, including carbon nanotubes (CNT) and carbon nanofibers (CNF). Two methods for nanocarbon production can be considered, namely methane decomposition and dry reforming of methane. Methane decomposition brings higher nanocarbon yield while dry reforming of methane can produce better quality nanocarbon products. However, several challenges still need to be addressed before CNT and CNF production technology reaches maturity, including: (1) development of new catalysts that lower the reaction temperature to below 700°C and improve conversions of CH_4 và CO_2 for CNT and CNF formation, as well as catalyst life; (2) development of effective methods of nanocarbon recovery; and (3) controllability of product physical and chemical properties.

References

1. ExxonMobil, PVN, PVEP, PSC Blocks 117-119. *Outline development plan (ODP) summary*. 2016.
2. Robert A.Dagle, Vanessa Dagle, Mark D.Bearden, Jamelyn D.Holladay, Theodore R.Krause, Shabbir Ahmed. *An overview of natural gas conversion technologies for co-production of hydrogen and value-added solid carbon products*. 2017.
3. R.Dagle, V.Dagle, M.Bearden, J.Holladay, T.Krause, S.Ahmed. *R&D opportunities for development of natural gas conversion technologies for co-production of hydrogen and value-added solid carbon products*. Argonne National Lab Report. 2017.
4. Marketsandmarkets. *Carbon nanotubes market worth 8.70 billion USD by 2022*. www.marketsandmarkets.com/PressReleases/carbon-nanotubes.asp.
5. Tiago P.Braga, Regina C.R.Santos, Barbara M.C.Sales, Bruno R.da Silva, Antônio N.Pinheiro, Edson R.Leite, Antoninho Valentini. *CO₂ mitigation by carbon nanotube formation during dry reforming of methane analyzed by factorial design combined with response surface methodology*. Chinese Journal of Catalysis. 2014; 35(4): p. 514 - 523.
6. Zirui Jia, Kaichang Kou, Ming Qin, Hongjing Wu, Fabrizio Puleo, Leonarda Liotta. *Controllable and large-scale synthesis of carbon nanostructures: A review on bamboo-like nanotubes*. 2017; 7(9): p. 256 - 276.
7. Kapil Moothi. *Carbon nanotube production from greenhouse gases during syngas synthesis*. University of the Witwatersrand. 2009.
8. Steven Corthals, Jasper Van Noyen, Jan Geboers, Tom Vosch, Duoduo Liang, Xiaoxing Ke, Johan Hofkens, Gustaaf Van Tendeloo, Pierre Jacobs, Bert Sels. *The beneficial effect of CO₂ in the low temperature synthesis of high quality carbon nanofibers and thin multiwalled carbon nanotubes from CH₄ over Ni catalysts*. Carbon. 2012; 50(2): p. 372 - 384.
9. S.Shukrullah, Norani Muti Mohammed, Maizatul Shaharun, Muhammad Yasin Naz. *Mass production of carbon nanotubes using fluidized bed reactor: A short review*. Trends in Applied Sciences Research. 2014; 9(3): p. 121 - 131.
10. Noel Peter Bengzon Tan, Bing Hui Chen. *Investigation of a fluidized bed chemical vapor deposition (FBCVD) reactor towards a large-scale multi-walled carbon nanotubes*. International Journal of Engineering Research & Technology. 2014; 3(5): p. 605 - 610.

11. Siang-Piao Chai, Sharif H.Zein, Abdul Rahman Mohamed. *A review on carbon nanotubes production via catalytic methane decomposition*. NAPCOL. 2004.
12. Jie Liu, Shoushan Fan, Hongjie Dai. *Recent advances in methods of forming carbon nanotubes*. *Advances in Carbon Nanotubes*. 2004; 29(4): p. 244 -250.
13. Arash Yahyazadeh, Behnam Khoshandam. *Carbon nanotube synthesis via the catalytic chemical vapor deposition of methane in the presence of iron, molybdenum, and iron-molybdenum alloy thin layer catalysts*. *Results in Physics*. 2017; 7: p. 3826 - 3837.
14. Kenji Hata, Don N.Futaba, Kohei Mizuno, Tatsunori Namai, Motoo Yumura, Sumio Iijima. *Water-assisted highly efficient synthesis of impurity-free single-walled carbon nanotubes*. *Science*. 2004; 306(5700): p. 1362 - 1364.
15. T.Maneerung, K.Hidajat, S.Kawi. *LaNiO₃ perovskite catalyst precursor for rapid decomposition of methane: Influence of temperature and presence of H₂ in feed stream*. *Catalysis Today*. 2011; 171(1): p. 24 - 35.
16. Avetik R.Harutyunyan, Bhabendra K.Pradhan, U.J.Kim, Gugang Chen, P.C.Eklund. *CVD synthesis of single wall carbon nanotubes under "soft" conditions*. *Nano Letters*. 2002; 2(5): p 525 - 530.
17. Chang Liu, Hui-Ming Cheng. *Carbon nanotubes: Controlled growth and application*. *Materials Today*. 2013; 16(1-2): p. 19 - 28.
18. Mukul Kumar, Yoshinori Ando. *Carbon nanotube synthesis and growth mechanism*. *Nanotechnology Perceptions*. 2010; 6(1): p. 7 - 28.
19. Poonam Sehwat, C.Julien, SS.Islam. *Carbon nanotubes in Li-ion batteries: A review*. *Materials Science and Engineering B*. 2016; 213: p. 12-40.
20. Sehwat et al. *Carbon nanotubes in Li-ion batteries: A review*. *Materials Science and Engineering B*. 2016; 213: p. 12 - 40.
21. Qing Zhang. *Carbon nanotubes and their applications*. CRC Press. 2012.
22. <http://www.yac.co.jp/en/-/fel/fel1>.
23. Chaenyung Cha, Su Ryon Shin, Nasim Annabi, Mehmet R.Dokmeci, Ali Khademhosseini. *Carbon-based nanomaterials: Multi-functional materials for biomedical engineering*. *ACS Nano*. 2013; 7(4): p. 2891 - 2897.
24. www.futuremarketsinc.com. *The global market for carbon nanotubes-forecast from 2010 to 2024*.

Stray current interference and mitigation for underground pipeline

Shaosong Chen¹, Yi Lu², Wei Cui¹, Xiaohu Zhang³, Guirong Wang³, Minxu Lu⁴

¹Beijing Ankocorr Technology Co., Ltd., Beijing, China, ²The Ohio State University, Columbus, Ohio, USA

³Beijing Safetech Pipeline Co., Ltd., Beijing, China, ⁴University of Science and Technology Beijing, China

Email: chenshs@ankopipe.com

Summary

Stray currents can have a wide range of interference effects on a pipeline, the most harmful being the creation of localised electrochemical corrosion cells that attack any buried metallic structure. Stray currents come from different sources, for example, DC rail transit systems and high voltage power transmission systems. It is important for the pipeline operators to determine whether stray currents are affecting the pipelines, identify the possible source(s) of stray currents, evaluate the severity of the stray current interferences on the pipelines and mitigate the interference effects. As urbanisation proceeds and more large-scale infrastructures are invested, oil and gas pipelines are threatened by stray current corrosion risks throughout their service life due to interference issues, which are not nuisance but rather major safety hazard that may take much effort to be taken care of. This article introduces two types of DC stray current interferences caused by DC rail transit systems and high voltage direct current transmission systems, and also gives a review on the state-of-the-art of best practices on mitigating these interferences for protection.

Key words: Stray current, corrosion, dynamic interference, high voltage direct current, transit system, mitigation, remote monitoring.

1. Introduction

Stray currents are caused by sources of current flowing through unintended paths. These can cause electrical interference and have significant effects on buried pipelines and other metallic structures. It is important for the pipeline operators to be aware of this as a type of risk as these stray currents can initiate and/or accelerate the corrosion of pipelines [1]. In this context, it is also obligated for the pipeline operators to determine whether stray currents are affecting the pipelines, identify the probable source(s) of stray currents, evaluate the severity of stray current interferences on the pipelines and mitigate the interference effects to protect the pipelines.

In the principle of electrochemistry, stray currents flow at the interface between electrolytes and metallic structures sitting in them through charge transfer reactions, governed by Faraday's Law. Stray currents have varied deleterious effects [2]. At the locations the current leaves the pipeline, oxidation reactions occur to convert electronic current to ionic current. If metallic matrices are involved in the oxidation process by releasing electrons directly, they are transformed into metallic ions and dissolved in the sitting electrolyte, which is known as

corrosion attack. Often this phenomenon is found in close proximity to the generation locations of stray currents or a holiday in the coating. At the locations the current flows into the pipeline, reduction reactions occur to convert ionic current to electronic current. Depending on what metallic structures are picking up stray currents, there might be different consequences. If the structure is coated and has its own cathodic protection (CP) system, stray current pickup, causing additional cathodic polarisation, may result in cathodic disbondment of the coating, and meanwhile, threaten the structural integrity by increasing the susceptibility of hydrogen embrittlement to sporadic hard spots of the pipeline (such as girth welds, plastically strained gouges, etc.) and the pipeline itself if made of high-strength steels. If the structure is made of amphoteric metals, the high pH niche developed at the structure/electrolyte interface caused by the reduction of water molecules can effect "cathodic" corrosion.

2. Sources of stray currents

Stray currents come from different sources and impose impacts on pipelines or other underground structures in varied manners, as summarised in Table 1. There are two types of stray currents, static and dynamic, both of which can be either direct currents or alternating currents. Static stray currents maintain a steady current

Table 1. Categorisation of stray current interferences

Types	Sources	Characteristics
DC interferences	HVDC transmission systems	Static, short-term
	DC transit rail systems	Dynamic, long-term
	Telluric currents	Dynamic, periodic
	Welding operations	Dynamic, intermittent
	Foreign CP systems	Static, long-term
AC interferences	HVAC transmission systems	Static, long-term
	High-speed railway systems	Dynamic, long-term
	Low voltage AC distribution systems	Static, long-term

flow and are often from other cathodic protection systems on pipelines or other underground structures conducting current flow via soil. Dynamic stray currents fluctuate over time and can come from natural or manmade sources.

Stray currents interfere with underground pipelines as a function of the way how they are generated.

a. High voltage direct current (HVDC) transmission can be performed using monopolar earth-return systems for regular inspection or accidental fault for a sustained period of time, during which thousands of amperes of current are injected into the earth. The monopolar earth-return operation mode causes the pipeline segments to be subject to cathodic or anodic interferences at different locations. The interference lasts a short term depending on the duration of the monopolar operation, normally a few hours, and is identified with an abrupt potential excursion on the potential-time plot.

b. Long-term interferences are often detected on the pipelines that are collocated with other infrastructures, such as DC-electrified transit systems, high voltage AC transmission systems, low voltage AC distribution systems, AC-electrified high-speed railway systems, and foreign cathodic protection systems. Long-term interferences can harm the integrity of the pipeline due to their accumulative effects throughout their service life. This necessitates not only the monitoring of the interference status on the pipeline but also the mitigation of the interferences.

c. Welding operations generate DC stray current intermittently as the welding machine is normally grounded. This poses the underground structures in proximity to the welding site in a situation of suffering from accelerating metal loss.

d. Telluric currents, natural stray currents, caused by the variations in the earth's magnetic field are well known to present difficulties to pipeline operators. These currents manifest themselves as pipe-to-soil potential fluctuations which are dependent on both location and time. Two

mechanisms are generally considered when discussing telluric current effects: classical electromagnetic induction that elucidates local changes in the earth's magnetic field will induce electrical current in stationary conductors such as pipelines; alternately, geomagnetic disturbances may result in large voltage gradients created in the earth's crust in which long metallic conductors such as pipelines merely carry the charge [3].

In the next paragraphs, this article will focus on two types of the above interferences - dynamic DC transit interference and HVDC interference - per the authors' experience in recent years.

3. Dynamic DC transit interference

3.1. Occurrence

Nowadays, the construction of electrified DC rail transit systems in modern cities, especially in developing countries, has been a movement to alleviate congested highways and to provide efficient mass transportation. However, dealing with corrosion and its detrimental effects, attributable to stray-current corrosion due to the DC rail systems, is, at the same time, becoming a challenge in terms of public safety, fortunately, with increasing awareness. The operation of DC rail systems causes stray current interference problems to the underground pipelines for transporting product oil, natural gas, water, etc.

The most common DC rail systems are traction powered by DC current supplied from substations via a positive feeder circuit (e.g., overhead power conductor in Figure 1) and use the running rails as the negative return circuit to return the power current to the substation. The running rails are in resistive or conductive contact with earth, rather than being ideally isolated from it, causing current leakage problem. Essentially, stray-current leakage is a result of the resistance relationship between the rail-to-earth return path and the running-rail return path. A high resistance of the running-rail negative return

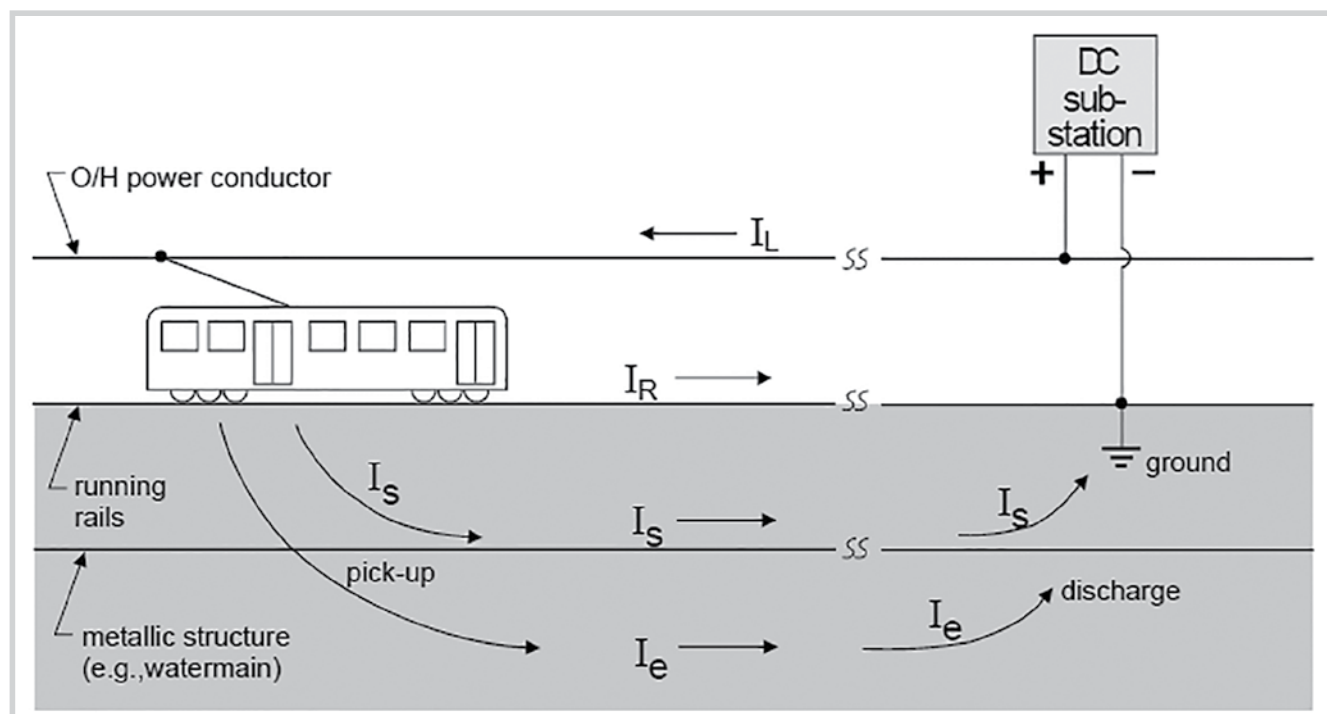


Figure 1. Generation of stray current from DC rail transit systems [2].

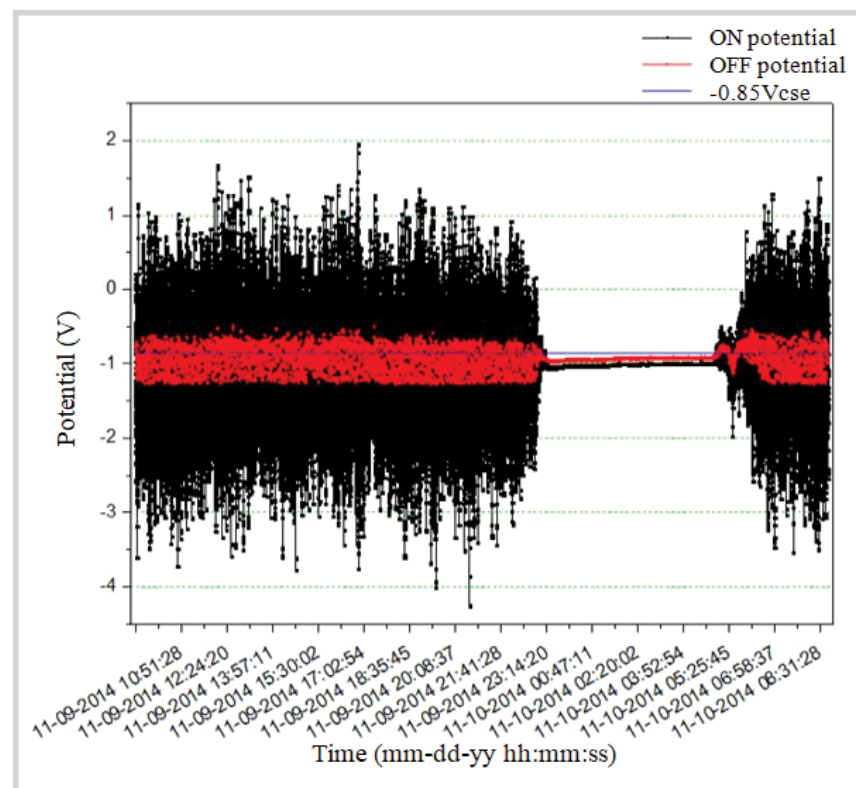


Figure 2. Pipe-to-soil potential vs time plot displaying fluctuations.

increases the voltage drop along the rails and, therefore, makes the rail-to-earth return circuit a more favourable path for the return current, thus causing stray-current leakage. These leakage currents in the earth tend to pick the paths like tunnel structure steel bars and underground metallic piping and cables with low resistance and then flow back to the substations [4]. The

current leakage off the running rails can be 5 - 10% of the power current for railcar running. This may seem a small percentage, but the stray currents can be substantial because the start-up load current can be several hundred amperes for a single railcar and several thousand amperes for a subway train. If the traction power is at the level of 2,000 - 3,000 amperes, the stray current leaking to the earth can reach up to 100 - 300A, which is significantly higher than the magnitude of current required by in which the cathodic protection systems for the underground pipelines, typically, at the level of several amperes to tens of amperes.

The stray current leakage behaves in a fluctuating manner. Not only will the magnitude of the stray current vary with time of day and whether the vehicle is accelerating or decelerating, but the location of stray current pick-up on the underground pipelines will also change as the railcar moves along the rails. Thus, a pipe-to-soil

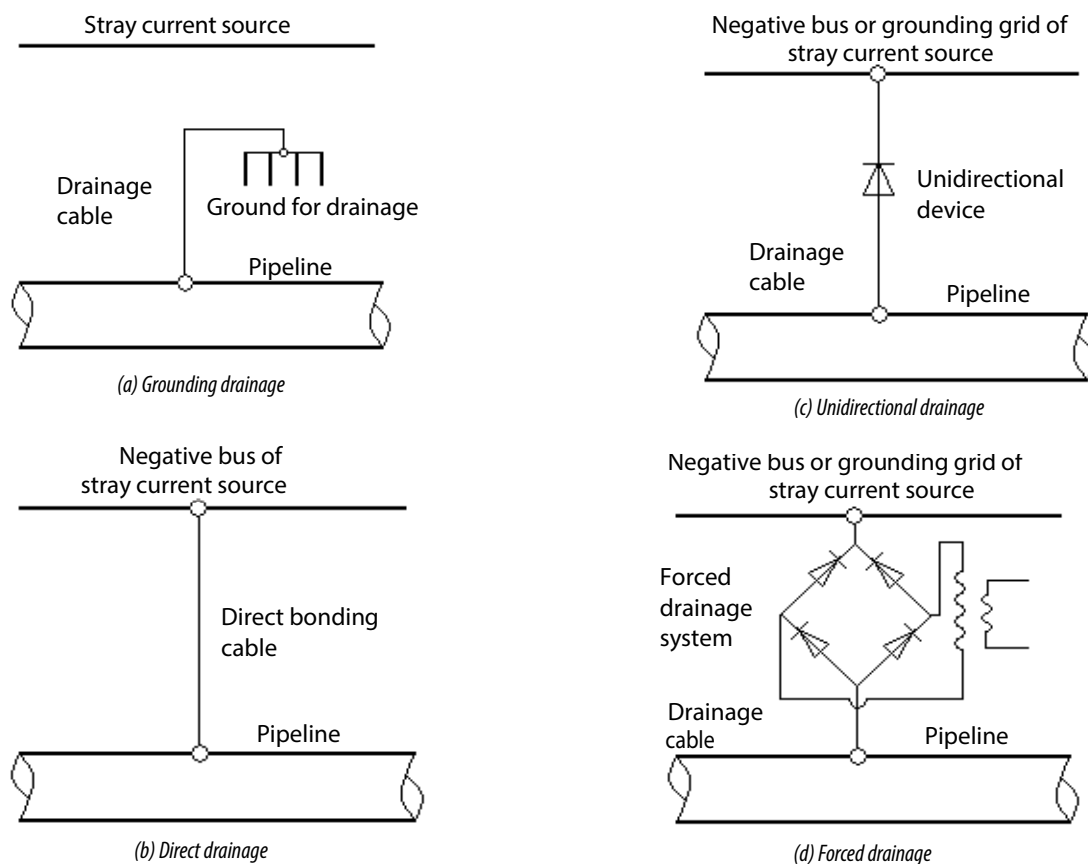


Figure 3. Layouts of different DC drainage systems.

potential recording will have a dynamic appearance, as seen in Figure 2 from our team’s project. The potential-time recording of stray current effects from a DC transit system has a distinctive pattern. There are considerable potential fluctuations during the daytime when the transit schedules are busy, while virtually no changes during the early morning hours. In Figure 2, the potential data was obtained with a data logger from a product pipeline with route intersected with a metro line. The plot shows that, from 8:30 am to 11:30 pm November 9 and from 5:30 am to 8:30 am November 10, the ON potential (black dots on solid line) and OFF potential (red dots on solid line) readings fluctuated rapidly, and roughly a third of the OFF potential readings excursed to the positive direction beyond the protection criterion $-0.85 V_{CSE}$ (blue solid line), indicating inadequate protection due to dynamic DC interference. While the ON potentials and OFF potentials nearly remained stable from 11:30 pm November 9 to 5:30 am November 10, and the OFF potential readings were approximately $-1.00 V_{CSE}$ indicating acceptable protection if the dynamic interference was off.

Although the stray current pick-up locations change with time, the discharge sites are predominately in proximity to the substation ground. Therefore,

determining the impact of transit-caused stray current on metallic facilities in urban areas requires comprehensive detection and evaluation, starting in the vicinity of the substation grounds and along the transit system route.

3.2. Mitigation

It is usually agreed by all parts that mitigating the DC transit interference on the pipelines is rather a task with challenge. Per the lessons the industry has learned so far, a committee comprised of local pipeline operators, the railway operators and the governing organisations is necessary to form to call for collaboration of the diagnosis, evaluation and mitigation of interference problems. Forming the committee and improving awareness has proved to be an effective and sometimes imperative way for interference control and mitigation.

Mitigation methods for minimising the deleterious effects of DC transit system stray currents include: electrical isolation of rails and substations implemented solely by the railway operators and regarded as proactive measures, and passive measures implemented in combination by the pipeline operators such as cathodic protection (CP), coating repair, drainage bonds, etc.

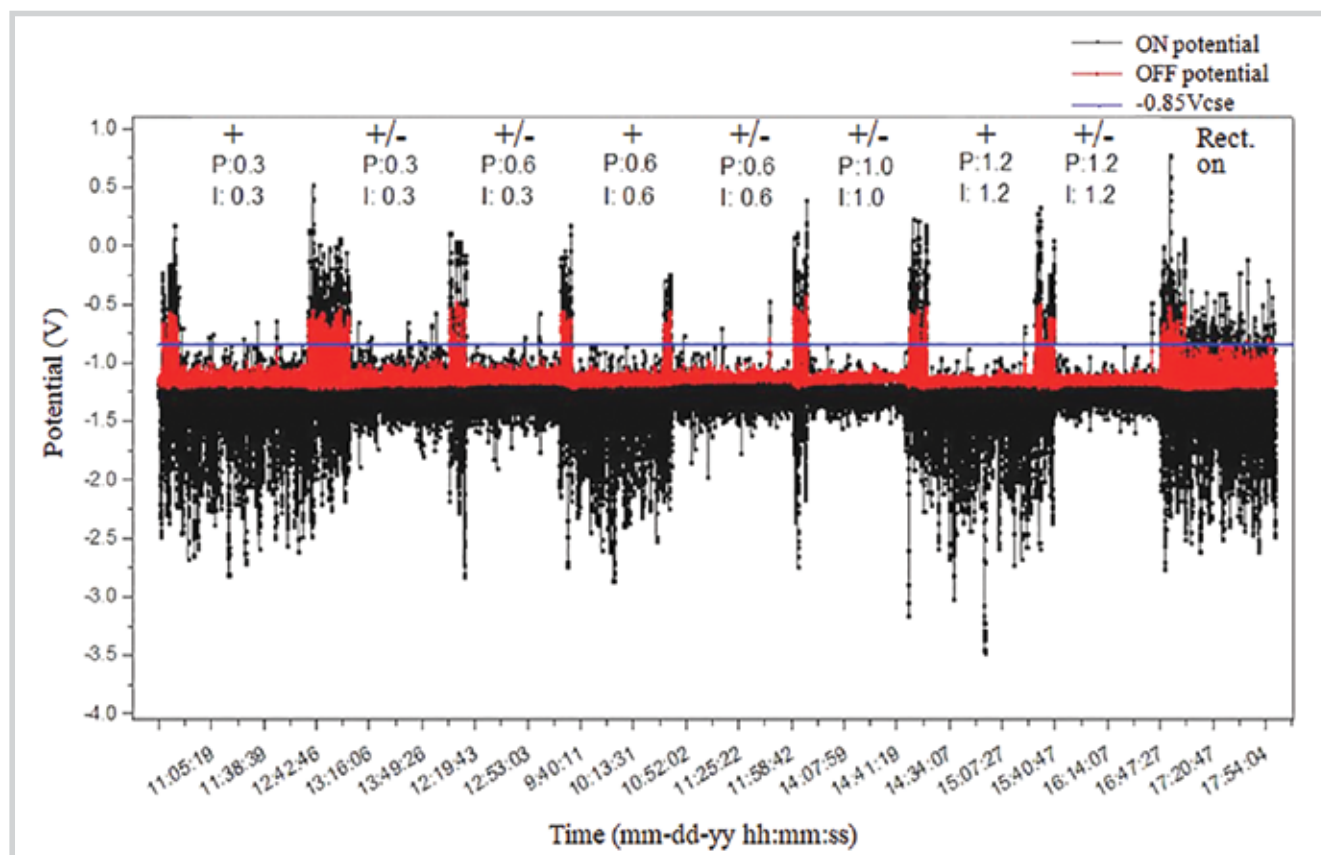


Figure 4. Comparison of potential excursions monitored on a product pipeline among the test durations when the innovated bidirectional drainage equipment was on or off.

Drainage measures are often sought for effectively driving stray current out of the pipeline in the controlled path [5]. The principle of drainage measures is to provide an electronic path for the stray current to return to its source, thus reducing the amount leaking to the electrolytic path. In practice, there are four different ways of building up DC drainage arrangements:

a. Grounding drainage

This drainage method (Figure 3a) is achieved by installing a groundbed close to the affected pipeline and connecting them together. Independent from the interference sources, this method is preferably applicable to the scenario the anodic areas of the pipelines are relatively fixed, where stray currents picked up by the pipelines from unknown locations are drained to the soil through the strategically installed groundbed.

b. Direct drainage

This drainage method is achieved by creating a stray current flow path from the pipeline to the negative bus of the stray current source. The execution of this method must ask for an agreement from the transit operators. In this method, the stray currents entering the pipeline

from unknown locations are directed back to the original source through the intentionally established path.

c. Unidirectional drainage

This drainage method is achieved by creating a current flow path from the pipeline via a unidirectional device (e.g. diodes) to the negative bus of the stray current source or a dedicated groundbed. An agreement must be asked from the transit operators if stray currents are to flow back to the original source. The unidirectional device is employed for avoiding stray currents from re-entering the pipeline through the groundbed or preventing stray currents circulating. In this way, this drainage arrangement is applicable to the scenario the affected pipeline segments are indefinitely changing between anodic and cathodic.

d. Forced drainage

This method is achieved by substituting the unidirectional device for a forced drainage device, for instance, a potential-controlled rectifier. The forced drainage device works if the pipeline potential is more positive than that of the original source or the dedicated groundbed. An agreement must be asked from the transit operators if stray currents are forced to flow back to the

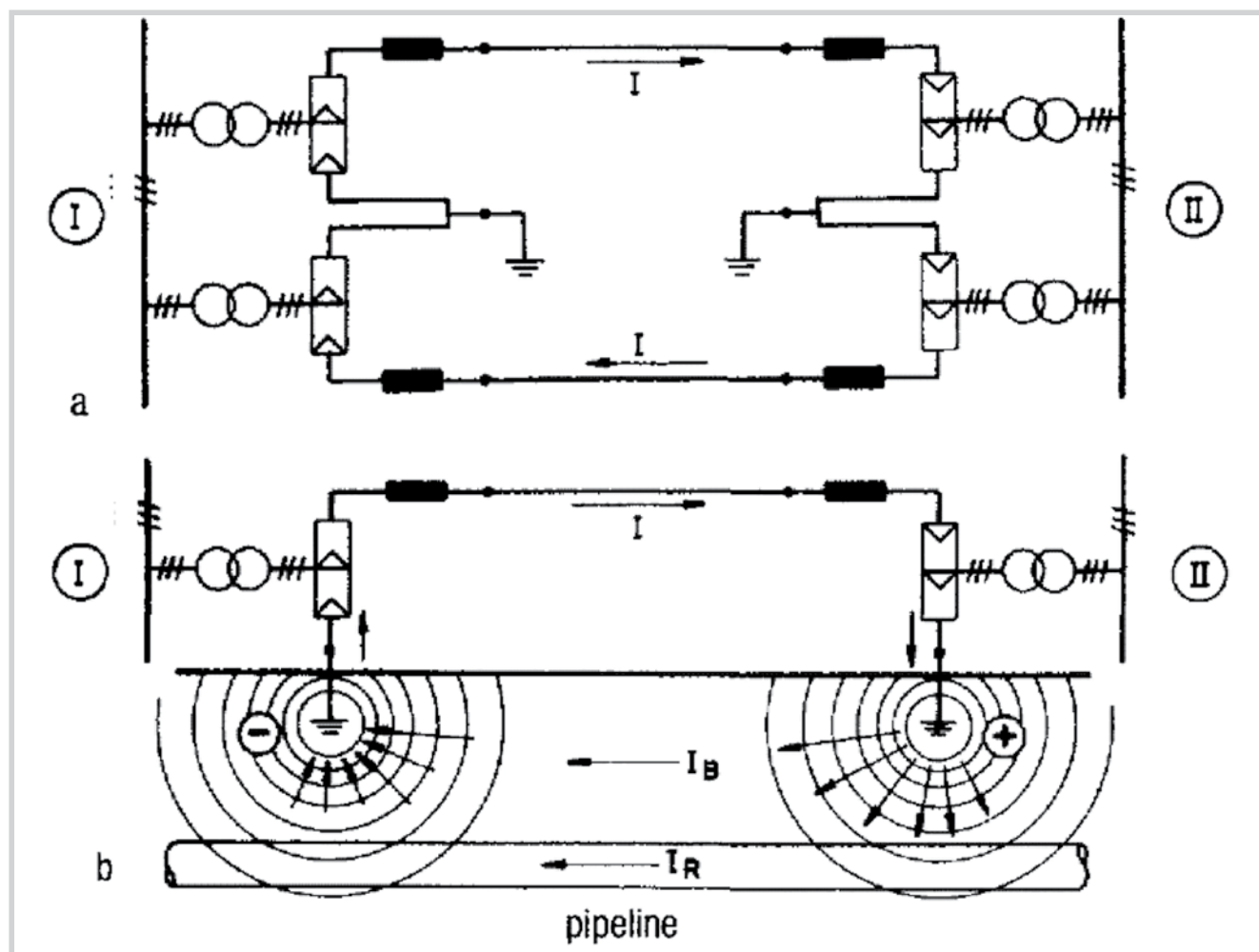


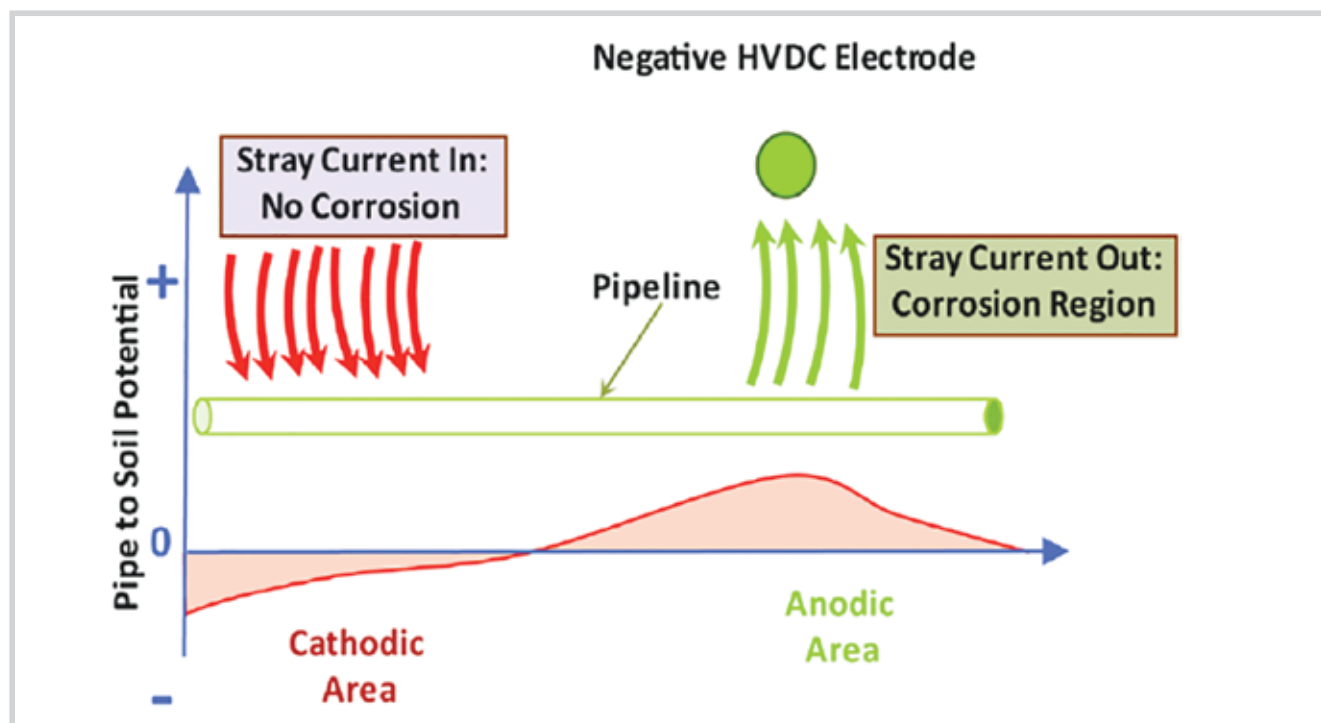
Figure 5. HVDC transmission operations [6]: bipolar systems (a), monopolar system (b).

original source. To be completely effective, the forced drainage arrangement must be located at the point of maximum discharge.

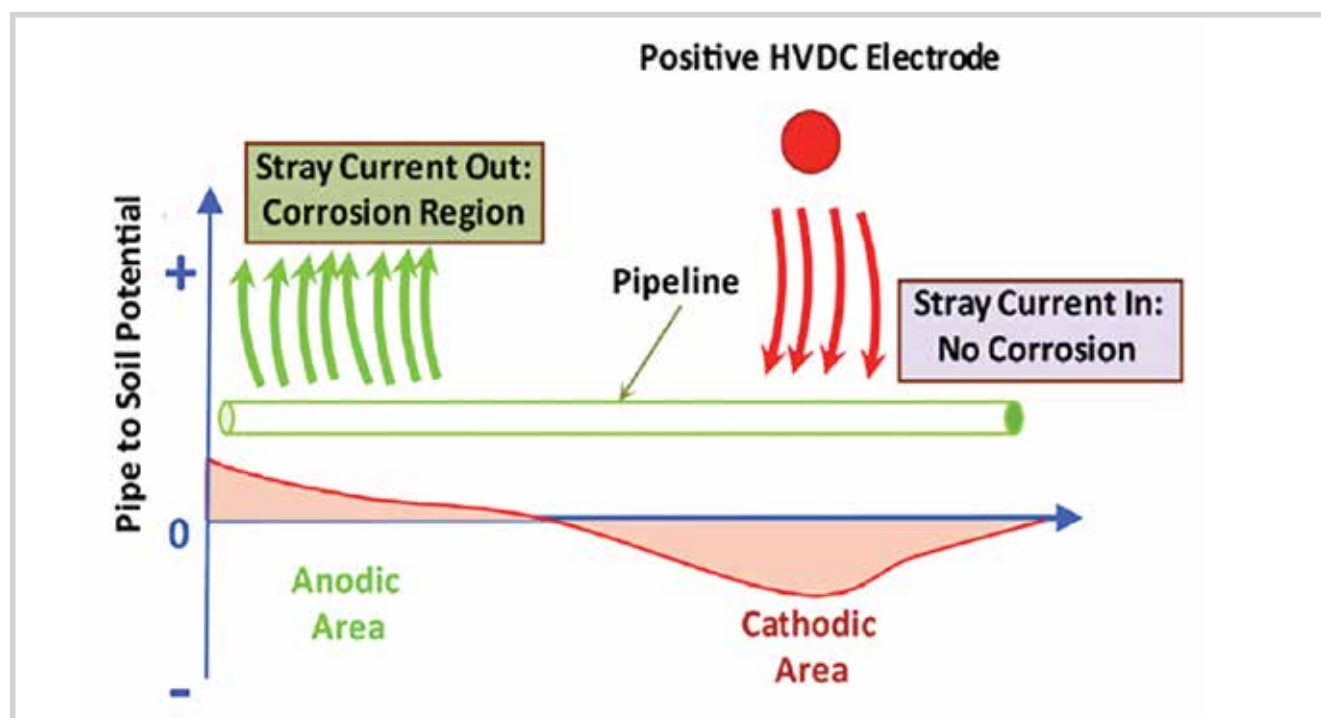
These drainage methods are described in the order happening to show the evolution course. All these methods are more applicable to mitigating interferences for pipeline sections adjacent to the negative return circuit of stray currents and are effective to controlling the OFF potential of these pipeline sections within the industrially-acknowledged criteria. At locations where anodic and cathodic interferences are mixed, none of the above drainage methods demonstrates the interference mitigation efficiency as expected. The authors' team has invented a set of potential-controlled bidirectional drainage equipment. This equipment is capable of feeding varied amount of current in both directions in response to the interference potential to cancel off the interference effects, by which the pipe-to-soil potential can be controlled within criteria. The equipment has been put

into a field test to verify the mitigating effect on the same product pipeline as related to Figure 2, and the results are displayed in a potential-time plot in Figure 4. From the plot, it is seen that, the OFF potential excursions of the pipeline under CP (Rect. on) were significantly reduced below $-0.85 V_{CSE}$ line when the bidirectional drainage equipment was in operation at different output modes (in which +/- stands for current output in positive or negative direction; P and I values reflect the response time). This invention has proved to be an additional choice for the mitigation of interference from DC rail transit systems.

To summarise, stray current corrosion caused by DC rail transit systems has been found on the underground pipelines or other structures in many cities all over the world. It is ultimately important for the pipeline operators to be clear of how severe these dynamic stray currents can cause wall loss of the pipelines and how to effectively mitigate the interference problems. However, neither evaluating the severity of dynamic DC stray current



(a) Cathodic HVDC interference



(b) Anodic HVDC interference

Figure 6. Mechanism of HVDC electrode interference [7].

interference nor mitigating the corrosion risk is a best-practice-procedure-following task. More efforts are certainly required from engineers, scientists, operators, regulators and officials in order to make informed decisions on improving the reliability of the pipelines and other underground utilities in the cities.

4. HVDC interference

4.1. Occurrence

HVDC transmission networks have been widely implemented globally in recent years. HVDC transmission is used to carry electrical energy over long distances or

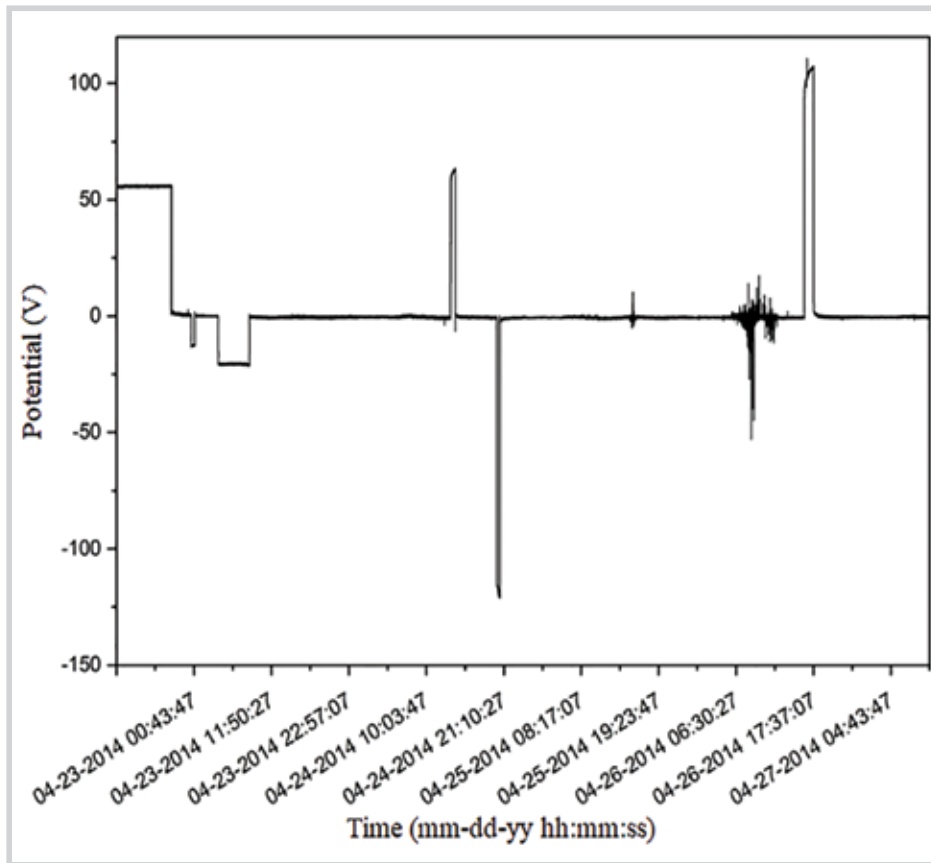


Figure 7. Pipe-to-soil potential shifts on a pipeline as a result of HVDC interference at different times.

to interface two AC power systems that might not be synchronised [6].

HVDC transmission systems may operate in such a manner that continuous (normal operation) or periodic (monopolar operation) direct current follows an earth path between HVDC system terminals [6], as seen in Figure 5. During such operations, a portion of the DC current that is flowing between the two HVDC electrodes is captured by the pipelines and associated grounding systems located in zones where the earth potentials are high and are discharged back to the soil at locations where the earth potentials are lower. More precisely, a pipeline may

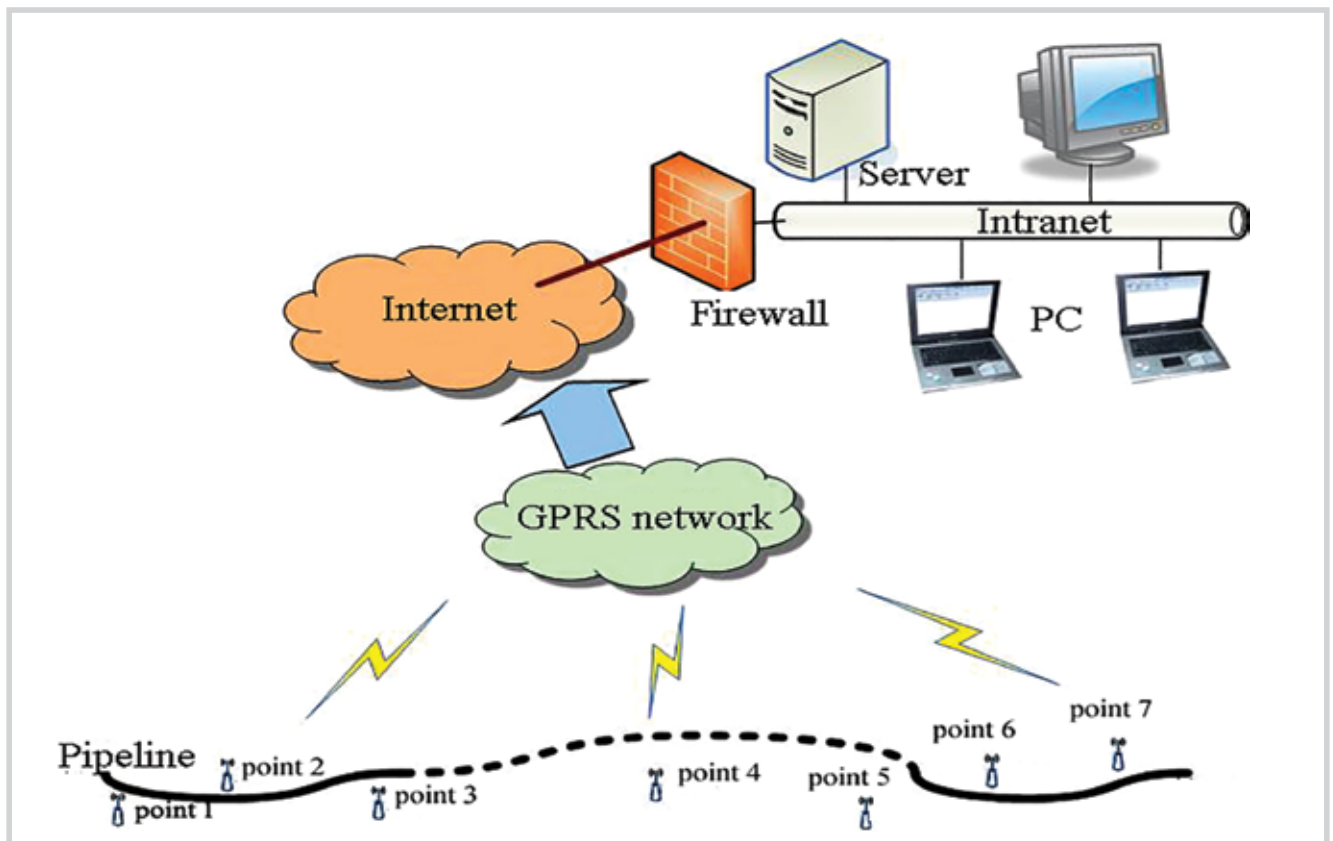


Figure 8. Remote monitoring and control network for HVDC interferences.



Figure 9. Intelligent data sampling units installed in test posts along the pipeline.

collect, conduct, or discharge a portion of this current depending on the location of the pipeline and the polarity of the HVDC ground electrode. Due to such excessive stray currents, pipe-to-soil potentials are accordingly shifted at different locations, making the potential-mileage plot similar to a “hat” shape, as seen in Figure 6. When the electrode near the pipeline is operating in positive mode, the current from the electrode is collected by the pipeline in the region located in the vicinity of the electrode, and then discharged from the pipeline at locations remote from the electrode. When the HVDC electrode near the pipeline is operating in negative mode, the current is discharged from the pipeline in the vicinity of the electrode and collected in the area far from the electrode.

Corrosion of the metallic pipelines occurs if DC stray current discharges from the metallic structure into the soil, namely, in the anodic areas in Figure 6. The corrosion, causing metal loss, is particularly critical on well-coated pipelines where the current discharge is concentrated at holidays in the coating. Perforation of the pipe wall can occur rapidly at a holiday as a result of the high density of current discharge from the pipeline to the earth. In the cathodic areas, pipe-to-soil potential shifts in the negative direction in Figure 6. This shift can be beneficial for the pipeline, provided that the pipe steel is not susceptible to hydrogen embrittlement. Otherwise, sustained high negative voltages can cause coating disbondment and embrittlement of high-strength steels [7]. Figure 7, from our team’s work, depicts the potentials of a pipeline continuously monitored with remote monitors for capturing HVDC interference events due to its proximity to a ground electrode in Southern China. The potential shifts indicate that, within this period, the pipeline at this monitoring location reached nearly 100V when the nearby HVDC electrode operated as a negative electrode, and in contrast, -120V when the nearby HVDC electrode operated as a positive electrode.

Depending on the soil condition and the relative position relationship between the pipeline and electrode (even several tens of kilometres apart), HVDC interference, can have massive impact on the pipeline in the range of hundreds of kilometres. Therefore, the concerns on their possible adverse impact on the environment have accelerated the need for accurate approaches to analyse HVDC adverse effects on neighbouring buried metallic utilities and development of appropriate effective and economical mitigation measures.

4.2. Mitigation

The mitigation of HVDC interference relies on comprehensive measures. Similar to the mitigation of dynamic DC interference, a collaborative committee should form

for problem solving. A proper design based on full engineering analysis and interference prediction is deemed to be the most effective method to avoid severe interference issues; however, this article only emphasises the possible mitigation measures for existing structures.

Most pipelines are located far from the HVDC electrodes, the interference sources, to make it not economical to install a bond. Because of the large voltage shifts, sacrificial anodes may not adequately compensate the local electric field caused by the HVDC earth current. The most practical mitigation method is to use an impressed current system powered by a potential controlled rectifier. Not only would the cathodic protection power supply be able to counteract the large positive potential shifts, but during the negative shift periods it would also shut down, thus minimising the stress on the coating [8].

Depending on the amplitude of HVDC earth current, it is ultimately necessary to divide the pipeline into numerous electrically isolated sections to increase the effective path resistance for facilitating the application of the above mitigation measures. In this way, sacrificial anodes can be used for mitigation. Besides, if the use of sacrificial anodes is still not adequate, using automatic potential-controlled rectifiers in each section can mitigate HVDC fault currents.

The author's team has accomplished to mitigate HVDC interference for the pipelines by using the abovementioned bidirectional forced drainage equipment. The equipment is capable of automatically adjusting the magnitudes and directions of the current outputs in response to shifts and changes in the structure-to-electrolyte potential. The HVDC interference case showed in Figure 7 was successfully mitigated at this location with the bidirectional forced drainage method. After mitigation measures were taken, the potential shifts have been controlled within the range between -27V in the negative direction and 23V in the positive direction.

4.3. Remote monitoring

HVDC interference on the underground pipelines has been found with the features of inadvertence, unpredictability, and random durations. Therefore, remote monitoring techniques are to seek for continual monitoring of not only the HVDC interference incidents but also the HVDC mitigation efficiency.

The continual monitoring of HVDC interferences can be achieved by configuring a remote monitoring and

control network, as depicted in Figure 8. The network is composed of three main elements:

a. Intelligent data sampling units

These units are installed in the test posts at the strategic locations along the pipeline (Figure 9), and, with the aid of buried coupons and permanent reference electrodes, measure the required parameters, such as potential, voltage, current and soil resistivity, etc. These data can be ready for automatic transmission or stored for retrieval.

b. Data transmission network

The data transmission network is the core to transmit the data measured at the test posts with certain protocols to servers for storage. On the other hand, commands for adjusting the work mode of the units are sent over the same network and received by the units. At present, the most popular data transmission network can be cellular communication network, satellite and other wireless techniques.

c. Servers

Servers are used via internet services to receive and store the field measurement data from the units for processing and analysis. All the HVDC monitoring data are managed through specialised software installed on the servers. Other than this, the management software is also integrated with control functions for changing the work mode of the units.

In order to effectively monitor HVDC interferences, multiple intelligent data sampling units are to be installed at the strategically selected locations along the pipeline right-of-way, minimally, at the pipeline section close to the HVDC electrodes. The occurrence of HVDC interference can be ascertained if the pipe-to-soil potential shifts are noticed at different monitoring locations at the same time.

5. Conclusions

Stray currents can have a wide range of interference effects on a pipeline, the most harmful being the creation of localised electrochemical corrosion cells that attack any buried metallic structure. Stray currents flow through unintended paths and come from different sources. It is important for the pipeline operators to determine whether stray currents are affecting the pipelines, identify the probable source(s) of stray currents, evaluate the

severity of the stray current interferences on the pipelines and mitigate the interference effects. DC stray current interferences caused by DC rail transit systems and high voltage direct current transmission systems are becoming more and more severe on the pipelines as urbanisation proceeds and more large-scale infrastructures are invested.

Acknowledged by the industry, a collaborative committee comprised of at least pipeline operators and the parts operating the interference sources is necessary to form for the diagnosis, evaluation and mitigation of interference problems. Diminishing the discharge of stray currents into soil is the most effective way; however, pipeline operators are still in need of their own measures for interference mitigation, such as CP. Forced drainage methods are often sought for DC interference mitigation when the stray current in the pipeline is at a high level. Other than conventional protection methods, bidirectional forced drainage methods have been accomplished by the author's team to mitigate dynamic transit DC and HVDC interferences. In order to evaluate the severity of interferences on a pipeline in a timely manner, remote monitoring techniques are recommended for continual monitoring of not only interference incidents but also mitigation efficiency.

References

1. Elizabeth Nicholson. *Stray current detection and correction*. Poland Corrosion Conference. 2010.
2. NACE International. *CP interference manual*. 2012.
3. T.Place, T.Smith. *Practical telluric compensation for pipeline close interval survey*. NACE International conference. 2000.
4. Thomas J.Barlo, Alan D.Zdunek. *Stray current corrosion in electrified rail systems: Final report*. 1995.
5. M.Cheng, Q.Tang, D.Weil, P.Zhang, *Comprehensive protection of buried steel pipelines at HVDC earthed electrode interference area*. Natural Gas Industry. 2015; 35 (9): p. 105 - 111.
6. Walter von Baeckmann, Wilhelm Schwenk, Werner Prinz. *Handbook of cathodic corrosion protection*. Gulf Professional Publishing. 2011.
7. Yu Gong, Chunlin Xue, Zhilei Yuan, Yexu Li, Farid Paul Dawalibi. *Advanced analysis of HVDC electrodes interference on neighboring pipelines*. Journal of Power and Energy Engineering. 2015; 3: p. 332 - 341.
8. NACE International. *High-voltage direct current interference (24254-SG)*. 2014.